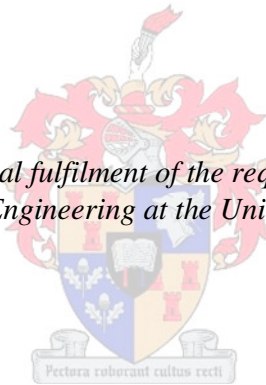# Design and Analysis Aspects of Radial Flux Air-cored Permanent Magnet Wind Generator System for Direct Battery Charging Applications

by

Johannes Abraham Stegmann

Thesis presented in partial fulfilment of the requirements for the degree
Master of Science in Engineering at the University of Stellenbosch

December 2010

Declaration

By submitting this thesis electronically, I, the undersigned, hereby declare that the entirety of the work contained therein is my own, original work, that I am the owner of the copyright thereof (unless to the extent explicitly otherwise stated) and that I have not previously in its entirety or in part submitted it for obtaining any qualification.

December 2010

Abstract

Design and Analysis Aspects of Radial Flux Air-cored Permanent Magnet Wind Generator System for Direct Battery Charging Applications

The electromagnetic and mechanical design aspects of optimally designed double-sided rotor radial flux permanent magnet wind generators with non-overlap air-cored (iron-less) stator windings are analysed in this thesis. The wind generator is implemented in a battery charging system for use in rural settlements and farms. The optimal generator and system design is based on an accurate analytical model and is confirmed with finite element analysis. It is shown, amongst other things, that the electromagnetic design and surprisingly not the mechanical design, determines the rotor yoke dimensions and, hence, largely the mass and cost of the generator. Alternative battery charging systems are also considered and discussed.

Opsomming

Ontwerp en Analiese Aspekte van Radiaal-vloed Lugkern Permanente Magneet Wind Generator Stelsel in Direkte Battery-Laai Toepassings

Die elektromagnetiese en meganiese ontwerp aspekte van optimaal ontwerpte dubbel-kant rotor radiale vloed permanente magneet windgenerators met nie-oorvleuelende lug kern (sonder yster) statorwindings word in hierdie tesis ontleed. Die windgenerator word geplaas in 'n battery-laai stelsel vir gebruik in landelike nedersettings en plase. Die optimale generator en die stelsel ontwerp is gegrond op 'n akkurate analitiese model en is bevestig met eindige element analise. Daar word onder andere getoon dat die elektromagnetiese ontwerp, en nie die meganiese ontwerp, die rotor juk dimensies en dus grootliks die massa en die koste van die generator, bepaal. Alternatiewe battery-laai stelsels word ook oorweeg en bespreek.

Author Publications

Work done in this thesis can be viewed, in part, in the following publications by the author:

International conference papers

J.A. Stegmann, M.J. Kamper, "Design Aspects of Medium Power Double Rotor Radial Flux Air-cored PM Wind Generators," *IEEE Energy Conversion Conference and Expo*, San Jose, USA, 19-24 September 2009, pp. 3634 - 3640.

National conference papers

J.A. Stegmann, M.J. Kamper, "Economic and efficiency evaluation of different battery charging wind generator systems," *Southern African Universities Power Engineering Conference (SAUPEC)*, pp.205-210, January 2010, Wits University, Johannesburg.

International Journal papers

J.A. Stegmann, M.J. Kamper, "Design Aspects of Double-Sided Rotor Radial Flux Air-cored Permanent Magnet Wind Generator," *IEEE Trans. on Industry Applications (IAS)*, currently in print.

Patent application:

South African Provisional Patent no. 2009/06507.

J.A. Stegmann and M.J. Kamper. Wind generator.

Acknowledgements

Thanks to...

God the Father – The Lord of all the universe, who cares to know my name.
  for freely giving undeserved grace to this sinner. *(Romans 3:24)*

Jesus Christ our Saviour – The eyes that see my sin, yet look on me with love.
  for loving me, even before I knew His name. *(Ephesians 1:4)*

Holy Spirit – The Spirit of Truth
  for lighting the way for my ever wondering heart. *(John 16:13)*

Prof. Maarten Kamper – Study leader
  for much wise counsel and encouragement.

Me. Daleen Kleyn – Electrical and electronic engineering secretary
  for helping me with a large part of my admin.

PH Petzer, A Swart and MH Jumat – The electrical workshop staff
  for their friendship and for helping with all the prototype building.

my EMLab colleagues and friends
  for their camaraderie and help.

Madri Burger – My girlfriend
  for loving me and sticking with me through some tough times.

Mom and Dad
  for their support and for believing in me.

"*The joy of the Lord is my strength*" – Nehemiah 8:10

Table of Contents

List of Figures

List of Tables

Nomenclature

Constants

Symbol	Meaning	Unit
C_p	Betz creation	(0.593)
g	Gravitational pull of earth	(9.80665 m/s)
γ_{cu}	Conductivity of copper at room temperature	$(1/\zeta_{cu\text{-}20} = 58.8 \times 10^6$ S/m)
μ_0	Permeability of air	$(4\pi \times 10^{-7}$ H/m)
μ_{cu}	Permeability of copper	$(1.2566290 \times 10^{-6}$ H/m)
π	pi	(3.141 592 653 589)
ρ_a	Density of air at sea level	$(1.225$ kg/m^3)
ρ_{cu}	Density of copper at room temperature	$(8930$ kg/m^3)
ρ_m	Density of magnet material (NdFeB) at room temperature	$(7501$ kg/m^3)
ρ_{fe}	Density of mild steel at room temperature	$(7850$ kg/m^3)
σ_{fe}	Yield stress of mild steel	$(250 \times 10^6$ Pascal)
$\zeta_{cu\text{-}20}$	Resistivity of copper at room temperature	(17 nΩm)

Variables (in alphabetical order with dimensionless units denoted by '#')

English alphabet symbols:

Symbol	Meaning	Unit
a	Number of parallel connected circuits	(#)
A_{cu}	Area occupied by the copper wire	(m^2)
A_g	Cross-sectional area of the facing magnet sides	(m^2)
A_{proj}	Projected area inside the cylinder pressure vessel	(m^2)
A_s	Swept area of the turbine blades	(m^2)
$A_{stressed}$	Area of the rotor yoke under stress	(m^2)

B	Average magnetic flux density in the air-gap (B_g) and in the steel rotor yoke (B_y). Residual magnetic flux density (B_r) and peak air-gap flux density of the fundamental harmonic (B_{p1})	(T)
c	Weibull plot scale parameter	(#)
C_f	Capacity factor	(#)
C_p	Turbine power coefficient	(#)
d	Average diameter of the air-gap stator winding	(m)
d_c	Single conductor diameter	(m)
d_i	Average diameter of inner curved permanent magnets	(m)
d_s	Solid shaft diameter	(m)
E	Young's modulus, or modulus of elasticity	(Pa)
E_g	Per phase back-EMF RMS voltage of the generator	(V)
E_{gp}	Per phase back-EMF peak sinusoidal voltage of the generator	(V)
E_{kw}	Kinetic energy in the wind	(J)
E_{oc}	Open circuit terminal voltage	(V)
f	Electrical frequency	(Hz)
F_{b1} & F_{b2}	Forces transferred by the bearings on the generator shaft	(N)
F_{Hoop}	Tangential hoop force inside the cylinder pressure vessel	(N)
F_m	Inter-magnet pulling force between inner and outer magnets	(N)
F_{ms}	Force due to the gravitational pull on the shaft mass	(N)
F_v	Vertical force exerted on the inner wall of the rotor yoke	(N)
h	Stator thickness/height measured in the radial direction	(m)
H	Magnetic field strength in the magnets (H_m), in the air-gap (H_g) and in the steel rotor yoke (H_y). Coercive magnetic field strength (H_c).	(A/m)
h_h	Order of the harmonics	(#)
h_m	Magnet thickness/height measured in the radial direction	(m)
h_y	Rotor yoke thickness/height measured in the radial direction	(m)
I_0	Area moment of inertia	(m^4)
I_{ac}	Per-phase ac-current	(A)
I_{sc}	Short circuit current	(A)
J	Current density	(A/mm^2)
k	Ratio of the copper losses to the total losses of the machine	(#)
k_s	Weibull plot shape parameter	(#)
K_1	Machine constant	(#)
K_2	Machine constant	(#)

k_d	Distribution factor	(#)
k_e	End-winding constant	(#)
k_f	Copper filling factor	(#)
K_n	Inductance correction factor (Nagaoka constant)	(#)
k_{pc}	Pitch factor of the concentrated winding	(#)
k_w	Stator winding factor	(#)
k_λ	Flux linkage factor	(#)
L	Length of the generator shaft	(m)
L_0	Initial length or thickness of the expanded material	(m)
l_a	Active length of a stator coil	(m)
l_b	Longitudinal length of a rotor yoke	(m)
L_c	Per-phase connecting cable inductance	(H)
l_e	Total end-winding length per coil	(m)
l_g	Air-gap length measured in the radial direction	(m)
L_i	Internal per-phase stator inductance	(H)
l_{ipg}	Inter polar gap length between permanent magnets	(m)
L_s	Total system inductance	(H)
L_T	Linear thermal expansion of a material	(m)
M_m	Mass of the permanent magnets	(kg)
M_y	Mass of the rotor yoke materials	(kg)
n_b	Base charging speed of the generator (cut-in speed)	(r/min)
n_r	Rated charging speed of the generator	(r/min)
N_p	Number of parallel strands in a conductor	(#)
N_t	Number of turns per coil	(#)
p	Number of permanent magnet poles	(#)
$p(v_w)$	Probability density function of the wind velocity	(#)
P_{aa}	Annual average turbine generator power	(W)
P_a	Total available power in the wind	(W)
P_{cu}	Copper losses in the generator	(W)
P_d	Developed power of the turbine	(W)
P_{dc}	Power delivered to the battery bank	(W)
P_{eddy}	Eddy losses	(W)
P_{gr}	Rated generator power	(W)
P_i	Internal pressure inside the cylinder pressure vessel	(Pa)
P_{rr}	Power at the point just before the diode rectifier	(W)
q	Number of stator coils per phase	(#)

Q	Total number of coils in stator	(#)
R_{ac}	Internal ac-equivalent resistance of the battery bank	(Ω)
r_b	Turbine blade length in the radial direction	(m)
R_c	Per-phase connecting cable resistance	(Ω)
R_{cu}	Resistance of copper wire	(Ω)
R_{dc}	Internal dc resistance of the battery bank	(Ω)
r_e	Average radius of the air-gap stator winding	(m)
R_{eddy}	Eddy current loss resistor model	(Ω)
r_{iy}	Inner rotor yoke average radius measured in the radial direction	(m)
R_{ph}	Per-phase resistance of copper stator windings	(Ω)
R_s	Total system resistance	(H)
S_f	Mechanical safety factor	(#)
t_c	Generator operating temperature	(°C)
$T \& T_0$	Final and initial member temperatures respectively	(°C)
T_d	Developed torque of the turbine	(Nm)
THD_V	Total harmonic distortion of the measured voltage waveforms	(%)
w	Coil side width (arc length of non-linearised model)	(m)
w_1	Weighting factor for the permanent magnet cost	(%)
w_2	Weighting factor for the copper cost	(%)
V_1	Voltage amplitude of the fundamental frequency	(V)
V_a	Volume of air interacting with the wind turbine	(m^3)
V_b	Fundamental RMS ac-equivalent battery phase voltage	(V)
V_{bat}	Battery bank voltage	(V)
V_d	Forward voltage drop over a diode in the rectifier	(V)
V_n	Voltage amplitude of the nth order harmonic frequency	(V)
v_w	Free flowing velocity of the wind	(m/s)
X_{Li}	Internal inductive reactance of the stator	(Ω)
Z_i	Per-phase internal impedance	(Ω)

Greek alphabet symbols:

Symbol	Meaning	Unit
δ	Phase angle between current and induced EMF	(rad)
Δ	Half of the coil side-width (linearised model)	(m)
ε_T	Thermal strain	(#)
η_g	Generator efficiency	(%)
η_s	Wind turbine system efficiency	(%)

κ	Per unit coil side width	(#)
λ_N	Flux linkage of the concentrated coil	(Wb-turns)
λ_s	Turbine blade tip speed ratio	(#)
μ_m	Permeability of the magnet material	(H/m)
θ_c	Coil width angle (non-linearised model)	(rad)
θ_m	Magnet angle (non-linearised model)	(rad)
θ_p	Magnet pitch angle (non-linearised model)	(rad)
θ_r	Coil side width angle (non-linearised model)	(rad)
ρ_a	Density of air at sea level	(kg/m^3)
ρ_{cu}	Density of the stator coil material (copper)	(kg/m^3)
ρ_{fe}	Density of the yoke material (steel)	(kg/m^3)
ρ_m	Density of the permanent magnet material (NdFeB)	(kg/m^3)
σ_h	Hoop stress in a cylinder pressure vessel	(Pa)
σ_l	Longitudinal stress in a cylinder pressure vessel	(Pa)
σ_r	Radial stress in a cylinder pressure vessel	(Pa)
σ_Y	Yield stress of a material	(Pa)
τ_m	Permanent magnet pole pitch	(#)
Υ_{max}	Maximum deflection of a cantilevered beam	(m)
ω_e	Electrical rotating speed (electrical frequency)	(rad/s)
ω_m	Mechanical angular velocity of the turbine	(rad/s)
ζ_{cu}	Resistivity of copper	(Ωm)

Chapter 1
Introduction

It is worthwhile to consider some of the history behind wind energy. History provides us with some insight into why we use wind energy the way we do today. Wind power is no new topic. For a long time man has been utilising wind power to help accomplish his work. Ancient civilizations used the wind to propel their sailing ships, turn their grain grinding mills and pull up heavy water filled buckets from their wells. This form of energy utilisation proved to be very efficient. The Persians discovered just how profitable this form of energy is when they started to build the first vertical axes windmills around 900 AD [1]. Wind energy also made its appearance during the Middle Ages in Europe. These early windmills were used primarily to convert kinetic energy to mechanical power.

More recently though, particularly in the last three decades, wind energy has really come of age. "Wind turbines" has become a generic term used to describe a rotating blade machine that converts the kinetic energy in the wind to useful power. With mechanical insight and technology constantly developing, the wind industry has grown into a multimillion dollar industry. Lately, a large driving force behind the development of new wind turbine technologies has been the concern for the environment. Renewable energy production methods, in particular wind, have received much attention due to a shift to this cleaner and more sustainable form of energy. Fossil fuels are no longer seen as the only reliable and infinite source of power, as was once thought.

1.1   Wind energy conversion

Wind energy may be free, but to harness it doesn't come cheap. The basic theory of converting the wind's kinetic energy into useful energy is discussed in this section. The reason for the kinetic energy present in the wind is due to wind consisting of moving air. To have kinetic energy a fluid medium has to possess mass and momentum [2]. Since atmospheric air is a gas made up largely of nitrogen and oxygen it possesses a low density. The average air density at sea level is 1.225 kg/m^3. This is

about 816 times lower than the density of water. Even though air has a low density, it still has mass and possesses kinetic energy. The kinetic energy present in the wind can be calculated by [1]

$$E_{kw} = \frac{1}{2}\rho_a V_a v_w^2 , \tag{1}$$

where E_{kw} is the kinetic energy in Joule, ρ_a is the air density, V_a is the volume of air interacting with the turbine and v_w is the velocity of the wind. This kinetic energy per unit time produces power. The total available power, P_a, present in the wind for a given area, is given by [4]

$$P_a = \frac{1}{2}\rho_a A_s v_w^3 , \tag{2}$$

where A_s is the swept area of the turbine blades. Three points that should be noted from this power equation are:

- The wind power density is proportional to the density of the air. Air density is dependent on temperature, pressure, humidity and altitude [3]. The density is directly proportional to pressure and inversely proportional to altitude, temperature and humidity.
- Power from the wind is directly proportional to the swept area of the turbine blades.
- The wind power is proportional to the cube of the wind velocity.

Considering the equation above, one can see that the wind speed plays a much larger role in the power content of the wind than the air density. This entails that locations with higher wind speeds will be more advantageous for wind power utilisation than locations with denser air. Higher wind speeds, in any case, usually occur at low pressures, where the density of air takes on low values [3].

Furthermore, not all of this available power can be extracted from the wind. Wind turbine power production depends on the aerodynamic interaction between the rotor blades and the wind. If all the energy in the wind could be extracted there would be no wind blowing behind the turbine. This would cause a build-up of air since it would not be exiting behind the blades. Since air has to pass through the turbine blade swept area, some of the kinetic energy in the wind should be retained behind the blades. This means that only a fraction of the total available power present in the wind can be harvested by wind turbines. The power equation now becomes:

$$P_{\max} = \frac{1}{2}C_p\rho_a A_s v_w^3 , \tag{3}$$

where C_p is known as the turbine power coefficient. It describes that fraction of power present in the wind which that can be converted by the turbine into mechanical work [4]. It can also be understood as the turbine efficiency. It should be noted that the turbine efficiency is not to be confused with the generator efficiency. The turbine efficiency is the ratio of the mechanical power delivered to the turbine blades to the kinetic energy in the incoming wind. This includes for instance

the aerodynamic blade efficiency. The generator efficiency on the other hand is the ratio of the electrical power output by the generator to the mechanical power input from the turbine blades. In an ideal turbine the maximum theoretical value of this power coefficient, C_p, is calculated as 0.5926. This value is known as the Betz criterion [4]. In other words, it is the maximum fraction of available power in the wind that can be captured by an ideal wind turbine. The power coefficient is affected largely by the blade profile design.

In order to increase the power generated, or to essentially better the turbine efficiency, C_p has to be maximised. The power coefficient is a function of the turbine's tip speed ratio. Turbine blades rotating at a low speed will allow the wind to pass through the gaps between the blades undisturbed, while high speed rotation will act as a barrier to the incoming wind [24]. In both of these cases the energy in the wind is not optimally resourced. By varying the tip speed of the blades with the incoming wind speed, an optimum C_p value can be realised.

The tip speed ratio, λ_s, defined as the ratio of blade tip speed to the free stream wind speed on the windward side of the turbine, is given by [1]

$$\lambda_s = \frac{r_b \omega_m}{v_w} \; , \tag{4}$$

where r_b is the turbine blade radius and ω_m is the mechanical angular velocity of the turbine. Many large wind turbines operate at a tip speed ratio of between 5 and 8 [3]. A typical tip-speed-ratio versus power coefficient graph is show in Fig. 1.

When designing a wind turbine the designer has a measure of control over the power coefficient and blade swept area but little control over the wind velocity and air density. For this reason the designer has to look not only at the wind turbine design, but also at the suitability of that turbine at a particular wind site. This means the designer has to possess at least a good base of wind behaviour and wind measurement expertise.
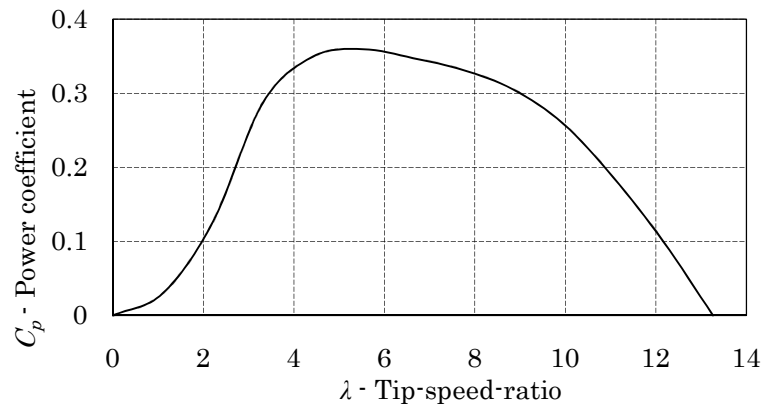
Fig. 1 : A typical power coefficient versus tip-speed-ratio plot.

1.2 Wind resources and global energy demand

The previous section showed the importance of designer's having some knowledge of how wind works. This is because a major wind turbine design consideration is the atmospheric conditions in which the turbine should operate. These conditions are, amongst others, the surrounding terrain (mountains, trees, flat), the annual wind speed distribution, weather (temperatures, rainfall) and location (ocean, shore or inland). In this section some basic theory will be presented.

Wind is caused by the sun. Air moves in the atmosphere from higher to lower pressures which are caused by uneven heating of the earth's surface by solar radiation. The amount of solar radiation absorbed at the equator, for example, is more that the amount at the poles. In a simplified flow model the air rises at the equator and sinks at the poles. There is however a large number of factors which complicates the global air flow considerably. Seasonal variations, the earth's rotation (Coriolis force), smooth ocean surfaces and mountainous land masses, to name a few.

More local winds, also known as tertiary wind conditions [21], also have many factors contributing to their behaviour. Some examples of tertiary circulation include the valley and mountain winds and land and sea winds. Valley and mountain winds are shown in Fig. 2. During the day the warmer air of the mountain slope rises and replaces the heavier cool air above it. The direction reverses at night, as the cold air drains down the slopes and stagnates on the valley floor. Land and sea winds are also opposites of each other. In the day the land mass, and the air above it, warms up more quickly than the sea. The hot air rises and it is replaced by cool air that blows in from the sea. An understanding of these wind patterns, and other local phenomena, are important for the evaluation of potential wind energy sites.

Another consideration when evaluating a potential wind site is the immediate surroundings. Obstacles like trees or buildings also interfere with the wind, most of them disadvantageously. A rule of thumb when positioning the turbine is to allow a distance of 20 times the height of objects obscuring the wind between the turbine and the obstruction. Also note that a grass covered field can also slow down the wind while the flat water surface in a lake does the opposite.
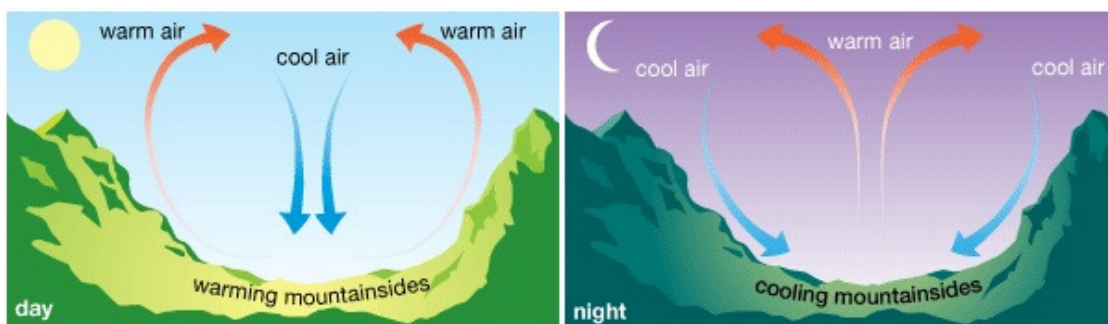
Fig. 2: Diurnal valley and mountain breezes [22].

As with any fluid in motion relative to a fixed medium, the wind generates friction with the medium's surface which causes a boundary layer [2]. The wind velocity decreases rapidly closer to the ground layer while at the same time the flow becomes more turbulent. As a result of this the tower height also plays an important role in turbine placement.

Global energy demand is growing exponentially and the need for clean renewable energy is on the increase. In 2009 alone 38 GW of wind energy was installed worldwide [5]. Studies also show that South Africa has good wind energy potential [6].

1.3   Wind turbine types

Wind energy converters that have been built over the years can be divided into two major groups namely lift devices and drag devices. In short, lift designs use airfoils to convert wind energy and drag designs use wind drag. Two further sub-categories include horizontal axis - and vertical axis turbines. Just as these names suggest, the drive-axis orientation is either in a horizontal or a vertical position. Their orientation is such that their drive axis lies either parallel or perpendicular, respectively, to the incoming wind. The most common designs are horizontal axis lift designs, but many useful vertical and horizontal axis drag machines have also been developed [7], [8]. An overview of each follows in the next sections.

1.3.1 Drag technology

Fig. 3(c) shows a typical drag device, a Savonius turbine. Drag devices like this operate by "catching" the wind perpendicular to a blade which successively turns the rotor. The drag force exerted by the wind on such a flat surface is a function of the relative wind velocity at the rotor surface (the difference between the wind speed and the speed of the surface). The rotor power is in turn a product of the drag force and rotational speed of the rotor surfaces. The power coefficient, C_p, of such a generator is a function of the tip-speed-ratio of the wind catching surfaces. One of the major drawbacks of such a turbine is the fact that the tip speed ratio of such a device cannot exceed unity since the speed at which the catching surface moves cannot exceed the oncoming wind speed. This is different for lift devices. This, of course, has a direct detrimental effect on the performance since a theoretical C_p of 0.08 occurs at a tip-speed-ratio of 0.33 [1]. This is significantly lower than the Betz limit of 0.5926 and makes this type of turbine rather ineffective over a large range of wind speeds.

Drag devices do however have some advantages. They are great for applications which require large torque at low speeds. They are however not as effective as lift devices at higher speeds. Classical multiple blade windmills, as used on farms, are called high solidity turbines [9]. In these turbines a large portion of the swept area is occupied by the turbine blades. Windmills are devices which require large torque to pump water and are a very attractive option for a drag technology.

1.3.2 Lift technology

Practical horizontal axis wind turbine designs use airfoil technology to transform the wind's kinetic energy into useful energy. The cross-sections of the wind turbine blades have the shape of an airfoil, as seen in Fig. 4. The airfoil, which is used amongst others in aeroplanes and some kites, is known for its aerodynamic lift property. The portion of drag force experienced on these blades is small compared to the lift force. Only the much larger lift force is converted into mechanical power, while the drag force acts as a braking force.

With tip-speed-ratios of up to 10 it can be seen that the forces that are developed by lift machines are significantly higher than those achievable with drag machines. The larger forces allow for much greater power coefficients. Compared to drag devices, lift devices operate at much higher rotational speeds and their blades occupy a lower portion of the swept area, hence they are referred to as low solidity turbines.

1.3.3 Horizontal axis turbines

The most common type of wind turbine is the horizontal axis wind turbine (HAWT). These constitute almost all grid-connected turbines built today [3]. They consist mainly of a propeller-type rotor mounted on a horizontal axis on top of a vertical tower. This type of turbine has to be aligned with the direction of the wind so that the air flows parallel to the axis of rotation. A distinction is made between upwind and downwind rotors. Upwind rotors, which face the wind in front of the vertical tower, have the advantage of avoiding the wind shade effect produced behind the tower. The presence of a solid object in the way of the wind causes a great deal of wind distortion and turbulence. A yaw mechanism is also necessary when building upwind rotors. This mechanism enables the rotor axis to be aligned with the direction of the wind. Downwind turbines, on the other hand, are placed on the leeward side of the tower. They can be built without a yaw mechanism provided that the nacelle is designed in such a way that it will passively follow the wind. A major disadvantage of this design is the fluctuations in the wind power due to the rotor blades passing through the wind shade of the tower.
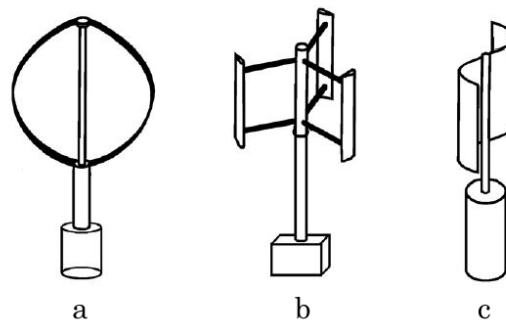
Fig. 3: (a) Darrieus turbine, (b) H-Rotor turbine, (c) Savonius turbine.
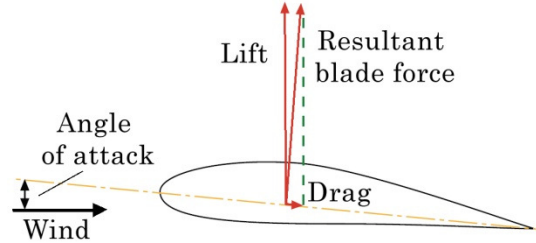
Fig. 4: Representation of an airfoil with its resultant forces.

1.3.4 Vertical axis turbines

In contrast with the mode of operation of HAWTs, the vertical axis wind turbine (VAWT) doesn't need to be aligned with the direction of the wind. Fig. 3 shows three types of VAWTs. These turbines do not need to be directed to the oncoming wind, eliminating the need for a yaw system. Classical water wheels allow the water to arrive tangentially to the water wheel at a right angle to the rotational axis. VAWTs are designed to act correspondingly toward air. One major advantage of such a turbine is that the generator and gearbox can be placed on the ground which makes them easily accessible. Some disadvantages include an overall lower level of efficiency, that the rotor is placed relatively close to the ground where wind speeds are lower and the fact that the turbine needs total dismantling in order for certain repairs to be done.

1.4   Radial flux permanent magnet generator

In large wind turbine applications the system usually consists of a wind turbine connected to a gearbox, which in turn is connected to an electric generator. Recently however, wind turbine developers have seen the advantages of omitting the gearbox and coupling the electric generator directly to the wind turbine of the system [10], [11] and [12]. The reason for this direct drive wind turbine is to minimise losses related to gearboxes. Since this topology eliminates the need for a gearbox, it also effectively eliminates the negative aspects associated with gearboxes such as the need for gearbox repairs, gearbox maintenance and complex installation procedures. Furthermore gearboxes are heavy and expensive. In this study a direct drive system is implemented.

A radial-flux permanent magnet (RFPM) direct drive generator derives its name from the radial orientation of its magnetic flux path, its permanent magnet excitation (PM) and its direct driven topology. In a radial flux machine, the magnetic flux lies perpendicular to the axis of rotation. The radial flux is produced by the permanent magnets present in this type of machine. These magnets replace the electromagnets produced by excited coils in other machines. One of the more popular alloys from which permanent magnets are manufactured, is known as neodymium-iron-boron ($Nd_2Fe_{14}B$). This is a type of rare earth magnet and is well known for its good strength to weight

ratio. Rare earth magnets do however have some disadvantages such as high costs and material brittleness.

An alternative topology to the radial-flux machine is known as an axial-flux machine. In this case the magnetic flux path lies axially along the machine, parallel to the axis of rotation. A simplified illustration of these machines is shown in Fig. 5. In both of these topologies the rotors are made up of two interconnected steel disks which act as a housing and flux return path for the surface-mounted permanent magnets. An air-cored (iron-less) stator is located between the two opposing rotors. The stator consists of copper conductors embedded in a hardened epoxy resin. In this study the focus is on a RFPM generator type.

1.5   Implementing wind generator systems in rural areas

There are many ways to supply a rural settlement with reliable electrical power. A good option could be to connect the area to the nearest national electricity grid. This option becomes uneconomical however, when the settlement is either very small and/or very far from the nearest grid connection point. In such a case the cost of installing transmission lines is far too high. An alternative is to let the settlement generate its own power and become independent of third party supply. To transform a rural village into a self sustaining grid-independent settlement, one has to design an electrical system which is able to generate, transmit and store electrical power. However, installing a stand-alone system can be harder than initially anticipated. Firstly, a resource is needed from which energy can be extracted. The resource should preferably be abundant and easily accessible in that specific area. Wind and solar energy are good examples as they are both globally
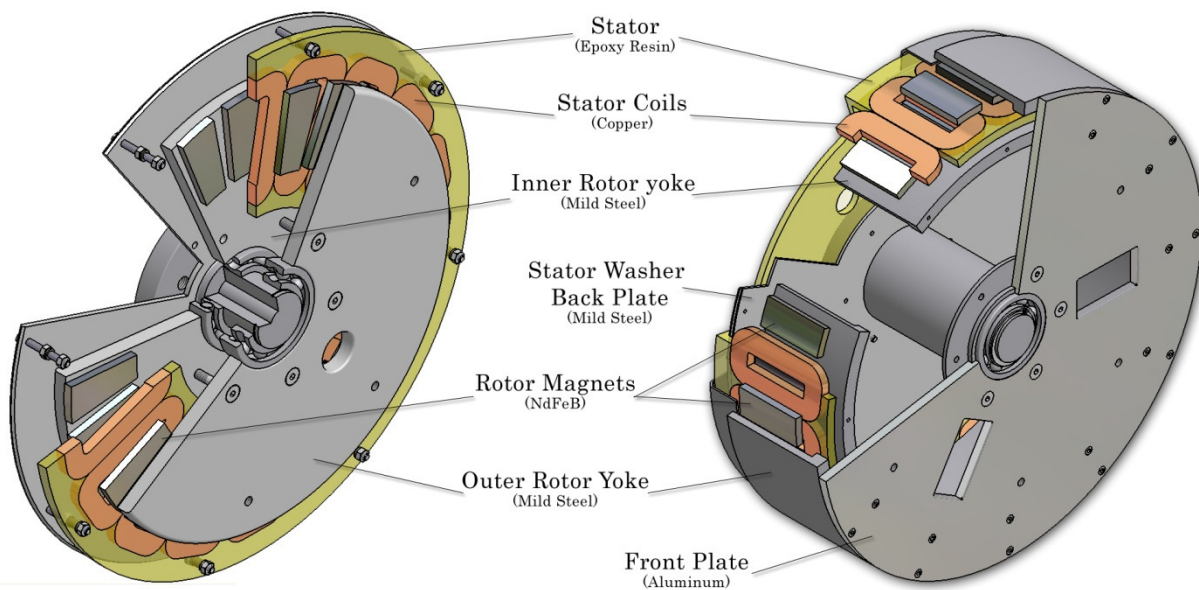
Fig. 5: AFPM (left) and RFPM (right) direct drive generators.

available. Secondly, a technology should exist that can convert this recourse's energy into useful electrical power. The technology should be efficient and reliable. Photovoltaic panels and wind turbines fall in this category. Thirdly, some means of storing this power should be available. When the power requirement of the users is low the surplus power should be stored for times when the demand will exceed the generation. This is necessary because the availability of the resource, especially in certain times of the day or year, will not always match the demand of its users. Lastly, all of this should be cheaper than simply installing a transmission line to the nearest electrical grid supply. The wind option will be in this study.

Implementing a rural wind turbine system

When optimising the design of a wind turbine system, site-specific characteristics can be included in the design process [13]. For example, to reduce the turbine system's energy production costs, the system can be optimally designed for different sites that have different wind conditions. These designs are advantageous in scenarios where a large number of units are installed in one location, e.g. offshore wind farms. Carrying out site-specific wind turbine optimisation, however, has its disadvantages. The industry trend is to produce a standard range of turbines, each operating at different conditions, rather than to redesign the generator for each new site.

Many small to medium power permanent magnet stand-alone wind generators are connected to the electrical load system via an uncontrolled diode rectifier or via an active synchronous rectifier, as shown in Fig. 6a and b respectively. In a rural setting the electrical load system can e.g. be a battery charging system or a micro-grid connected system. In the case of an uncontrolled diode rectifier the fundamental component of the generator current is in-phase with the terminal voltage as shown in the phasor diagram in Fig. 6a. The current angle, δ, in this case is equal to the phase angle between the induced voltage, E_g, of the generator and the voltage, V, at the diode bridge. To ensure sinusoidal
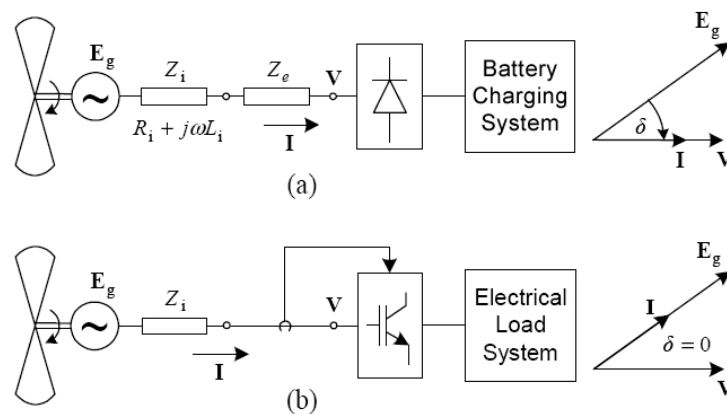
Fig. 6: PM stand-alone wind generator systems: (a) Diode rectifier and (b) active rectifier system.

currents and also an improved power matching with the turbine, an external reactance X_e (capacitive or inductive) [15], [32] may be used in series with the impedance $Z_i = R_i + j\omega L_i$ of the generator and connecting cable. This reactance has a direct effect on the current angle of the system. In the case of an active synchronous rectifier the phase currents are controlled to be sinusoidal to ensure high torque quality and low noise coming from the generator. The currents are also controlled to be in-phase with the induced voltage E_g to ensure maximum torque per copper loss operation of the generator. The current angle in this case becomes zero as shown in Fig. 6b. In the design and the design optimisation of the generator it is, thus, important to take into account the type of load system the generator is connecting to. In cases where the current angle is not zero ($\delta \neq 0$) the generator does not operate at its optimum performance. The implication of this is that an oversized machine must be designed to generate the necessary torque and power, and to generate this torque and power at a satisfying efficiency.

1.6   Problem statement

Many designers of small wind turbines (typically sub 100 kW) emphasize the simplistic design of the wind generators so as to allow for little or no maintenance. These generators are usually direct-drive permanent magnet (PM) synchronous machines which are directed windward by a simple tale vain yaw system. Small wind turbines are used amongst others in water pumping, electrification of fencing and small weather station power. The dominant share of the market for small wind turbines, however, lies in off-grid residential properties [14]. These homes are usually powered by hybrid systems incorporating wind, solar and in some cases diesel generators.
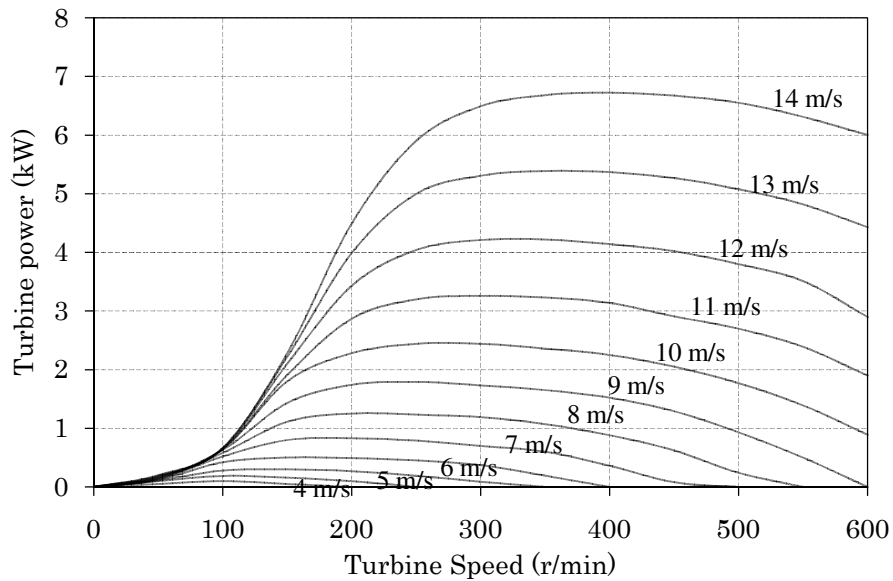
Fig. 7: Estimated 3 kW *Aero Energy* turbine blade power curves.

In developing countries, especially, many non-grid connected rural areas are in need of reliable and low cost electrical power. To solve this problem numerous wind power systems have been developed and implemented over the years to supply farms and rural settlements with high quality electrical power. For these applications, direct-connected battery charging systems are most often used. The wind generators are used to charge the battery banks, whilst the battery banks allow for an uninterrupted inverter-fed power supply without requiring continuous turbine operation. Typically, these stand-alone systems are used where a grid connection would be too expensive. Many of these systems have shown that the energy capture of the wind turbine falls short of expectations based on only the generator rating and rotor size [14], [15], [16].

Problems to solve

Firstly, a concern arises as the small to medium scale wind turbine generators implemented in the above mentioned systems, are still too expensive and complex for the average consumer to consider buying and installing. These generators are heavy and skilled personnel are usually required to perform maintenance on them. Off-the-shelf parts are rarely available and repairs are not cheap. A need arises for a reliable, simple and cost-effective wind generation technology that can be implemented in rural areas where little or no maintenance is possible.

Secondly, a demand for an effective and economical power conversion and storage system arises. This system needs to transform the power delivered by the electric generator into good quality power that can be used and stored by various loads. The cost per energy of such a system needs to be optimised.

1.7   Approach to problem

To solve the problems associated with the generator, an alternative machine is designed to try to counter the problems associated with small to medium wind turbines. There are numerous types of generators and turbine technologies available that can be used in rural electrification. In this study the focus is on an air-cored RFPM generator used in rural stand-alone wind energy systems. There is an attempt to illuminate some advantages of using this type of generator and compare some off-grid topologies in which it is used. The generator is optimised both electrically and mechanically. Mass, cost and performance play a large role in the optimisation procedure. Cost per energy produced should remain competitive to other standalone system.

1.8 Thesis layout

Chapter 1: Introduction

A short history of wind power development is discussed. Wind power concepts and basic theory of energy production are explained. Contemporary problems are identified and possible solutions are suggested.

Chapter 2: Analysis of the RFPM generator and system

The RFPM electrical generator is examined and optimised. This generator is then implemented into a battery charging system and the entire system is analysed.

Chapter 3: Mechanical design of the RFPM generator

The RFPM electrical generator's mechanical design aspects are examined. Optimisations in terms of mass and cost are done.

Chapter 4: Simulated and measured results

Generator simulations and system measurements are presented and discussed.

Chapter 5: Comparing three different generation systems

Alternative system designs are evaluated in terms of their efficiency and economical aspects. Cost per energy is calculated for each system.

Chapter 6: Conclusions and recommendations

Some conclusions are drawn and recommendations are made.

Appendix A: External inductor design

Appendix B: Eddy currents

Appendix C: Fastener design

Appendix D: Deflection of a cantilevered beam

Appendix E: Derivations of important formulae

Chapter 2
Analysis of the RFPM Air-cored Generator and System

In this chapter the aims is to examine the electrical design of a wind turbine generator and its corresponding transmission and storage system as used in small to medium scale wind turbine applications. The generator, a radial-flux permanent magnet (RFPM) air-cored machine, is implemented in a battery charging system. The alternating current (ac) produced by the generator is rectified to direct current (dc) through a six-pulse diode rectifier. A 36 V battery load, which serves as an energy storage unit, is connected to the wind turbine system.

2.1 Generator components

2.1.1 Rotor

The rotor of the RFPM generator consists of two cylindrical steel yokes located concentrically one inside the other. The reason for both an inner and an outer yoke is the double row of permanent magnet (PM) material necessary to maintain the required magnetic flux density in the air-gap located between them. The large effective air-gap present in an air-cored generator possesses a much lower permeability than an iron-cored generator does. To maintain the same flux density levels in the air-gap more PM material is needed. The two steel cylindrical rotors provide a rigid steel construction, which maintains the air-gap length as well as supplies a return path for the PM's magnetic flux. Unlike in iron-cored generators, in an RFPM air-cored machine the flux distribution inside the steel rotor yokes remains static during operation. For this reason the iron losses in the rotors become negligible [18].

Permanent magnet placement and shape

The RFPM generator yokes have circumferential arrays of alternating polarity permanent magnets. The magnets are equally spaced on each yoke's periphery.
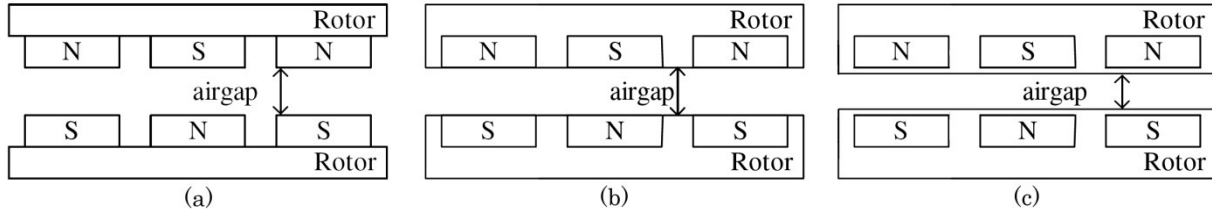
Fig. 8: (a) Surface mounted, (b) partially embedded and (c) and fully embedded.

Inner and outer magnets are placed opposite to each other to form pole pairs. A pole pair is magnetised in the same direction. The permanent magnets can be placed in one of three ways. They are fully embedded, partially embedded or surface-mounted. These three configurations are depicted in Fig. 8. A major advantage of the surface-mounted magnets is that the steel yokes do not have to possess machined slots as in the case of embedded magnets. The absence of slots allows machining costs to drop, which makes the generator more economical. Another advantage is that the surface-mounted magnets act as a fan which creates a natural wind cooling effect inside the machine [19]. The rated operating speed of the direct drive RFPM generator is relatively low and centrifugal forces present on the magnets are small. This means that the magnets can be glued onto the yokes. If the speed of such a machine increases other means of fastening, like through magnet screws, should be considered [24].

The RFPM generator discussed in this study makes use of the surface-mounted topology. This is primarily due to the large air-gap present in air-cored machines, which causes high amounts of magnet leakage flux to occur if the magnets are embedded within the steel. This leakage flux occurs between the magnets and iron yoke and is discussed later in the chapter. Both surfaces on which the magnets are placed are arc shaped due to the circular yokes. This means that the shape of each magnet also needs to be curved and to be radially magnetised.

2.1.2 Stator

Unlike the rotor, the stator of the RFPM air-cored generator is a non-ferrous component. Whereas a conventional iron-cored generator has punched iron laminations in the stator around which the stator coils are wound, an air-cored generator has air (or another non-magnetic material). This type of stator creates a large effective air-gap between the rotor magnets, which causes low armature magnetic flux in this region. The low armature magnetic flux of the stator is responsible for the low inductance values of these coreless machines [24].

The round cylinder stator piece is located between the two rotor disks. Conductors are located circumferentially around the air-gap and are kept in place with epoxy resin to form the stator. The stator is manufactured by casting the piece with the help of a mould.
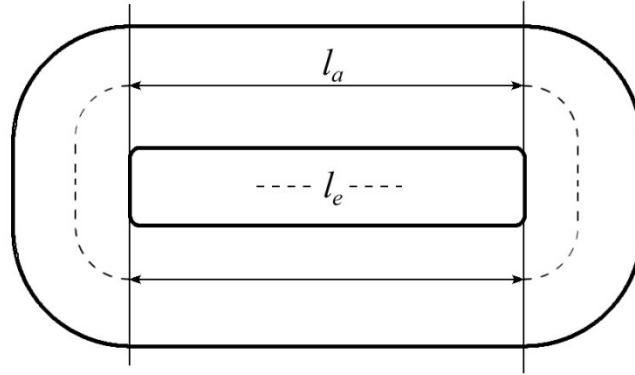
Fig. 9: RFPM generator coil profile.

Coils

The copper wire used in this generator prototype application is round annealed polyamide coated wire. Each coil is individually wound around a plastic PVC former with the help of a coil jig and a wire winding machine. Once a coil is wound its sides are tied together with a piece of string known as winding twine. This helps secure the coil dimensions against deformation before it is removed from the former. The finished coil profile is shown in Fig. 9. The active length, l_a, and the end turn length, l_e, are shown. The total length of a single turn can be approximated as $2l_a + l_e$. It should be noted that the end turn length is an approximate average length.

2.1.3 Winding layout

The most common stator winding type used in iron-cored RFPM machines is the overlapping winding layout which comprises of normal overlapping stator coils [24]. An overlapping winding layout requires that the end-windings of the different phase coils overlap each other, effectively causing long end windings. Recent studies on RFPM machine winding layouts have found the benefit of incorporating concentrated windings in these machines [25]. The main reasons for considering this alternate winding topology is the potential reduction in manufacturing cost, while simultaneously producing the same amount of torque. Using concentrated coils allows for a simpler coil construction [27] which could ultimately lead to automated manufacturing of the stator and smaller end-turn lengths of the coils implying less copper being used [25]. Overlapping windings are also very difficult to realise in these machines because of their double-sided rotor topology.

Both the overlapping and the concentrated winding topologies can be seen in Fig. 10. To distinguish between the three electrical phases, they are marked with red, yellow and blue. The winding layout chosen for this study uses a concentrated winding topology. In Fig. 11 such a winding type together with some dimensional properties, is shown.
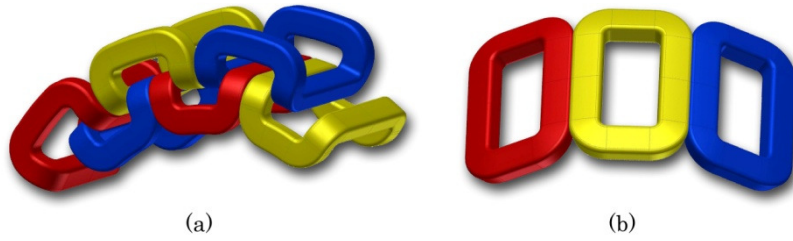
Fig. 10: (a) Overlapping winding and (b) concentrated winding [25].
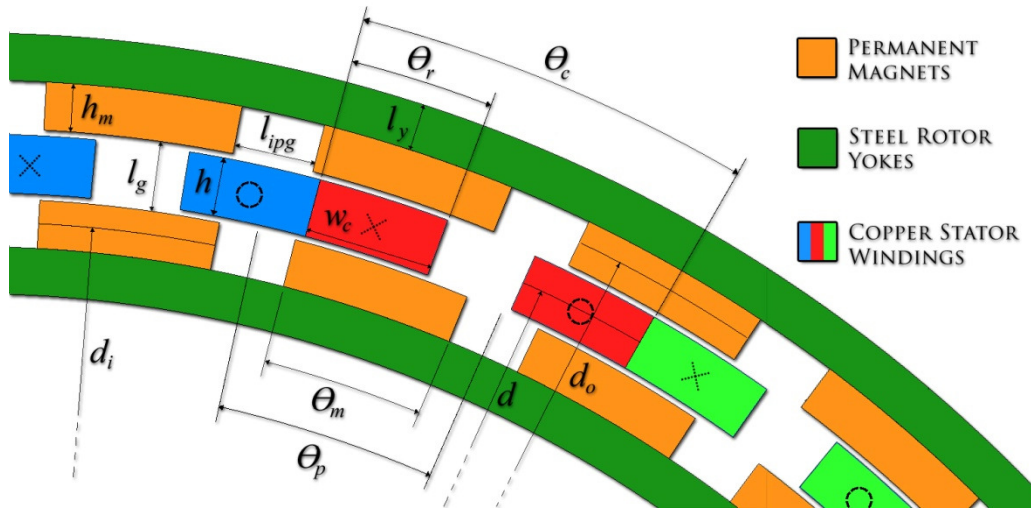
Fig. 11: Cross-section of the RFPM machine and concentrated winding layout.
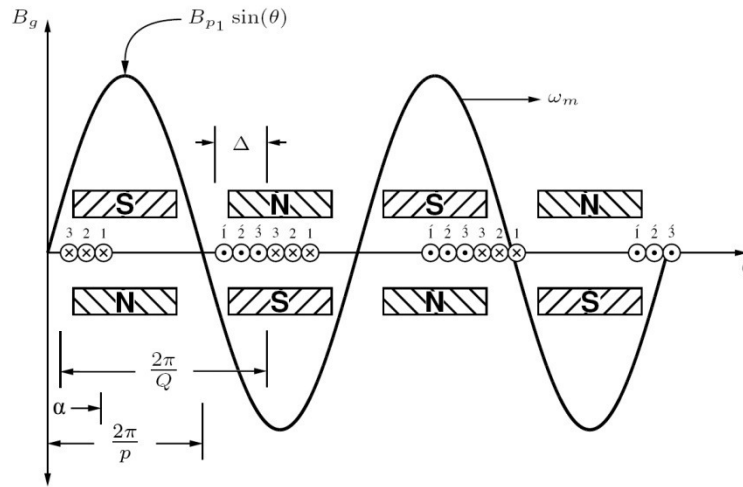
Fig. 12: A linearised model of a three-phase concentrated coil distribution [25].

Fig. 12 shows a linearised cross-sectional view of a RFPM machine with a three-phase concentrated coil layout, together with the permanent magnets and the fundamental sinusoidal magnetic flux created in the air-gap. With the correct sizing and spacing of the pole magnets it was

found that the air-gap flux density in an axial flux air-cored permanent magnet machine could be made quasi-sinusoidal [25]. For theoretical analysis, it can therefore also be assumed that the flux density distribution a RFPM air-cored machine is also sinusoidal as shown.

For N_t conductors, the flux linkage of the concentrated coil winding layout can be calculated by [25] as

$$\lambda_N = \frac{4}{p} N_t B_{p1} r_e \, l_a k_\lambda ,$$

(5)

where p is the number of PM poles, N_t is the number of turns per coil, B_{p1} is the peak air-gap flux density of the fundamental harmonic, r_e is the average radius of the stator winding, l_a is the active length of the stator winding and k_λ is defined from the linear model in Fig. 12 as

$$k_\lambda = \frac{\cos\left(\dfrac{\pi}{Q}\dfrac{p}{2} - \Delta\dfrac{p}{2}\right) - \cos\left(\dfrac{\pi}{Q}\dfrac{p}{2}\right)}{\Delta\dfrac{p}{2}} ,$$

(6)

where Q is the total number of stator coils and Δ is the coil side-width length (shown in Fig. 12). The overlapping and concentrated stator coil configurations can be compared in terms of flux linkage. The flux linkage is directly proportional to the flux linkage factor, k_λ. In Fig. 13 the flux linkage factor of both an overlapping winding and concentrated winding are plotted against the per unit coil side width, κ, where κ is defined from Fig. 12 as

$$\kappa = \frac{\Delta}{\Delta_{max}} ,$$

(7)

with Δ_{max} defined as

$$\Delta_{max} = \frac{2\pi}{Q} .$$

(8)

From Fig. 13 it can be seen that the value of κ can range from 0 to a maximum of 0.5; that is, the coil side width can only occupy up to half of the total coil width. κ can also be defined in terms of the non-linearised model of Fig. 11 as a angle ratio given by

$$\kappa = \frac{\theta_r}{\theta_c} .$$

(9)

Fig. 13 shows how the flux linkage varies with change in the coil side width. The concentrated winding topology reaches a peak flux linkage at a κ of 0.37 (or 37% of its maximum possible value) with k_λ at 0.966. The developed torque of the generator is directly affected with a change in κ and the chosen value will be discussed in later sections.
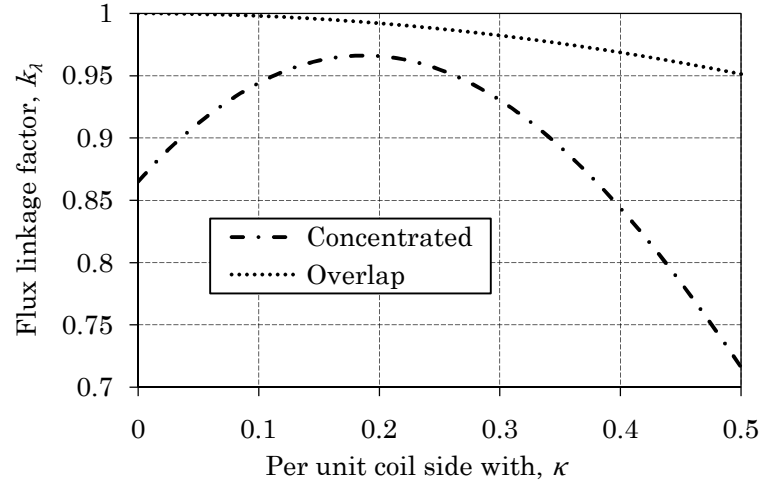
Fig. 13: Flux linkage versus coil side width [25].

2.2   Electrical analysis of the RFPM generator

The electrical analysis of the RFPM machine is discussed in this section. Each component of the wind generator having an influence on the generators electrical characteristics, is considered.

2.2.1 Equivalent circuit

Consider a three-phase generator having terminals A, B and C feeding a balanced three-phase load. The generator and its load are both connected in wye. Both of the neutral points of the generator and load are at the same potential because the load is balanced. Consequently, we could connect them without affecting the behaviour of the voltages or currents in the circuit. We can thus simplify the generator by modelling only one phase. The single phase equivalent circuit diagram is modelled as seen in Fig. 14 [33]. This enables calculations to be done on the steady-state generator model.

Shown on the left is the induced electro-motive force (EMF). The EMF is produced by the time-varying magnetic flux inside the air-gap stator coils as given by Faraday's law [33]. This is represented by an ac voltage source, E_g. Each phase of the stator winding possesses an internal resistance, R_i, and an internal inductance, L_i, in series with the back-EMF voltage which together correspond to the internal impedance of the generator. Connected in parallel with E_g is a resistance, R_{eddy}, symbolizing the Eddy-current losses in the stator coils. Flowing out of the generator model is the induced ac current, I_{ac}, and V_t is the voltage at the generator terminals. All of these parameters, together representing the complete RFPM air-cored generator model, are discussed.
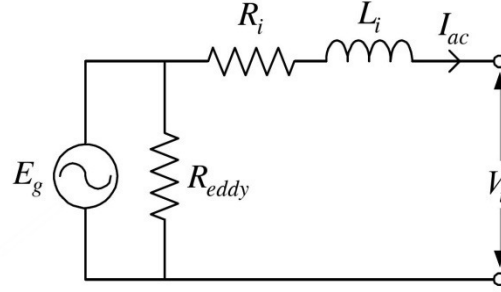
Fig. 14: Equivalent circuit of the RFPM generator [24].

Induced phase voltage, E_g

The peak sinusoidal induced phase voltage, E_{gp}, of the in the concentrated winding stator can be calculated by [28]

$$E_{gp} = \frac{q}{a}\frac{4}{p}\omega_e N_t B_{p1} r_e l_a k_{pc} k_d,$$ (10)

where q is the number of stator coils per phase, a is the number of parallel connected circuits, p is the number of PM poles, ω_e is the electrical rotating speed, N_t is the number of turns per coil, B_{p1} is the peak air-gap flux density of the fundamental harmonic, r_e is the average radius of the stator winding, l_a is the active length of the stator winding, k_{pc} is the pitch factor of the concentrated winding and k_d is the distribution factor. The electrical rotating speed, ω_e, is related to the generator's mechanical rotating speed, ω_m, by

$$\omega_e = \left(\frac{p}{2}\right)\omega_m.$$ (11)

The number of stator coils per phase can be calculated by

$$q = \frac{Q}{3}.$$ (12)

The radial flux density in the air-gap of a coreless RFPM generator can be approximated as having a flat-topped, near trapezoidal waveform [24]. For typical machine dimensions, the ratio of the flat-topped flux density value, B_g, to the peak fundamental component (first harmonic), B_{p1}, is determined from finite element (FE) analysis for a per-unit magnet pitch of $\tau_m = 0.7$ as

$$\frac{B_g}{B_{p1}} \approx 0.937 \quad [\tau_m = 0.7],$$ (13)

where B_g is the dc-value of the trapezoidal waveform plateau of the flux density waveform in the air-gap and τ_m is given from Fig. 11 as

$$\tau_m = \frac{\theta_m}{\theta_p}.$$ (14)

τ_m plays an important role, amongst other things, in the leakage flux constraints discussed later in this chapter. An optimal τ_m-value found by [26] that can be used in the analytical design is $\tau_m = 0.7$.

FE results represented in Fig. 15 show the near trapezoidal waveform of the average radial air-gap flux density. This average flux density occurs around the circumference of the machine in the space half way between the permanent magnet poles. In other words, it is measured on the average stator diameter denoted by d in Fig. 11. The reason for the radial flux having an almost trapezoidal form can be traced to the fact that small amounts 3rd and 5th harmonic content is present in the waveform [31]. This is due to the occurrence of tangential leakage flux in the spaces between the magnets. B_g can either be measured or estimated analytically from the demagnetisation B-H curve of the permanent magnet material.

The average stator coil radius, r_e, can be calculated by

$$r_e = \frac{d}{2},$$ (15)

where d is the average stator diameter shown in Fig. 11. The active length of the stator winding, l_a, is taken as extending into the paper in Fig. 11. The pitch factor, k_{pc}, of the concentrated winding (which is equivalent to the flux linkage factor in (6)) can be calculated in terms of the non-linear model of Fig. 11 by [28]

$$k_{pc} = \frac{2\sin\left(\theta_c\left(1-\kappa\right)/2\right)\sin\left(\theta_c\kappa/2\right)}{\kappa\theta_c},$$ (16)

where

$$\theta_c = \frac{\pi p}{Q}$$ (17)
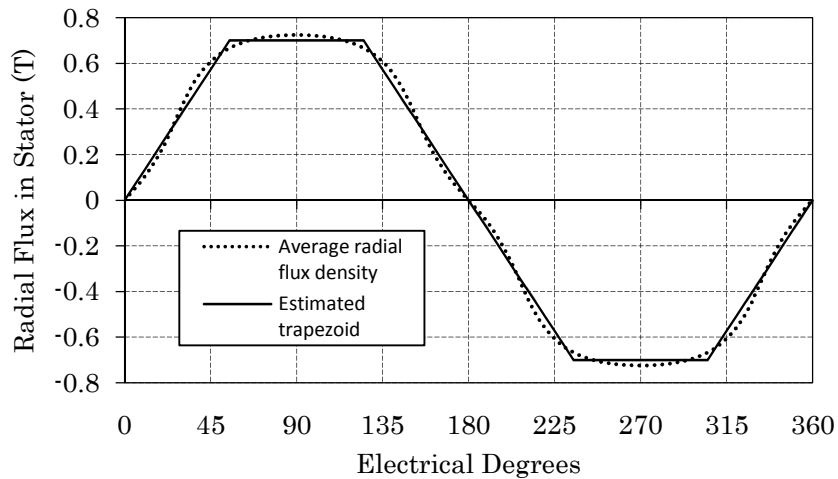
Fig. 15: FE generated radial flux density in the air-gap between two adjacent magnets and an approximate trapezoid.

and

$$\kappa = \frac{\theta_r}{\theta_c} \ . \tag{18}$$

The distribution factor, k_d, can be calculated by [28]

$$k_d = \frac{\sin\left(n(\theta_c - \pi)/2\right)}{n\sin\left((\theta_c - \pi)/2\right)}, \tag{19}$$

where $n = 1$ for a stator with one coil in a phase band. More coils of the same phase ($n > 1$) can be put side by side to form a phase group.

Stator resistance, R_i

The phase resistance can be used to calculate the copper losses in the stator windings of the RFPM generator. To calculate the phase resistance, we first have to consider the resistance of copper wire, R_{cu}, that can be calculated by [25]

$$R_{cu} = \frac{\zeta_{cu}\left(2l_a + l_e\right)}{A_{cu}}, \tag{20}$$

where A_{cu} is the area occupied by the copper wire and ζ_{cu} is the resistivity of copper which can be approximated as [24]

$$\zeta_{cu} = \zeta_{cu-20}\left(1 + 0.0039(t_c - 20)\right), \tag{21}$$

where $\zeta_{cu\text{-}20}$ is the resistivity of copper at 20°C (room temperature) and t_c is the generator operating temperature in °C. The total end-winding length, l_e, per coil is calculated by [29] as

$$l_e = \frac{4r_e\theta_c}{p}\left(1 - 0.586\kappa\right). \tag{22}$$

The copper area, A_{cu}, can be calculated by

$$A_{cu} = \frac{\left(h \times w\right)k_f}{N_t}, \tag{23}$$

where w is the coil side width ($w \approx 2r_e\Delta$) and k_f is the copper filling factor. The filling factor is defined as the ratio of the cross-sectional area occupied by the copper to the total area available in the coil side. Substituting (23) into (20), the total resistance for a coil with N_t windings, can thus be calculated as

$$R_{cu} = \frac{N_t^2 \rho_{cu}\left(2l_a + l_e\right)}{k_f\, hw}. \tag{24}$$

The total per phase resistance, R_i, with q number of coils per phase and a the number of parallel circuits, can now be calculated by

$$
\begin{aligned}
R_i &= \frac{q\, R_{cu}}{a^2} \\
&= \frac{N_t^2 q \rho_{cu}\left(2l_a + l_e\right)}{a^2\, k_f h w}
\end{aligned}
\tag{25}
$$

Stator inductance, L_i

Each stator winding possesses an internal synchronous inductance. The coreless nature of the RFPM generator stator causes this inductance to have a very low value. The internal per-phase inductance of a concentrated coil stator winding, L_i, can be calculated from an adapted air-cored multilayer solenoid formula given in [24] as

$$
L_i = \frac{q\left(2l_a + l_e\right)^2 N_t^2}{h_a} 10^{-7} K_n,
\tag{26}
$$

where K_n is a correction factor known as the Nagaoka constant. K_n is necessary for the non-uniform magnetic field present in the winding during normal operation. The constant can be expressed as [24]

$$
K_n = \frac{1}{1 + 0.9\left(\dfrac{2l_a + l_e}{2\pi h}\right) + 0.32\left(\dfrac{2\pi w}{2l_a + l_e}\right) + 0.84\left(\dfrac{w}{h}\right)}.
\tag{27}
$$

Eddy-current losses, R_{eddy}

In an electric machine there are electromagnetic losses which can be divided into iron losses and copper losses. The copper losses consist of ohmic-losses and eddy-current losses while iron-losses comprise of hysteresis and eddy-current losses [33]. There are no iron-losses possible in the air-cored (iron-less) stator. There are also negligible iron-losses in the rotor yoke and permanent magnets due to the generator being a synchronous machine. In a synchronous machine the fundamental magnetic field in the stator rotates at the same speed as the rotor and thus no alternating flux is present in the rotor yokes or magnets. This is especially true for air-cored generators. For these reasons both the rotor and stator of the generator are essentially iron-loss free and can be ignored [24]. The ohmic-loss component of the copper-losses present in the stator windings are modelled by a resistor R_i, as shown in Fig. 14.

From a machine perspective, it is desirable to use a simple eddy-loss calculation which can easily be incorporate into the design optimisation procedure. The eddy-current loss can be calculated based on the analytical solution of the eddy-loss in a single conductor lying in a transverse alternating magnetic field [29]. Eddy-loss is thus approximated as

$$P_{eddy} = \frac{\pi l_a d_c^{\ 4} B_{p1}^2 \omega_e^2 Q N_t N_p}{32 \zeta_{cu}}, \tag{28}$$

where N_p is the number of parallel strands in a conductor. From (28) it can be seen that the eddy losses are proportional to d_c^4; with d_c representing a single conductor diameter. Minor increases in wire diameter would thus cause major increases in eddy-losses. To minimise eddy-current losses in the conductors of the stator winding, multiple thin conductor strands are connected in parallel instead of using a single thicker wire. This also has a positive effect on the fill factor, k_f, since the smaller conductors tend to have a tighter packing in their slot. This may however create a new problem. Circulating eddy currents between the parallel paths may occur [29]. This is due to the conductor closer to the permanent magnet experiencing a higher magnetic flux density compared to the conductor in the radial centre of the stator winding. To overcome this, the strands of parallel conductors can be twisted and transposed. Twisting is performed so that each of the parallel strands occupies all the possible positions in the active length of the coil. It has been shown that this method can almost eliminate the eddy losses [40]. A discussion on eddy-loss measurement and minimisation techniques are included in Appendix B.

2.3   Optimisation of the RFPM generator

A general rule of thumb when designing a wind turbine is to make the generator that is located on top of the tower as simple and as light as possible. An uncomplicated design helps decrease maintenance costs and makes for easy assembly and installation. A generator with a lower mass requires a less rigid tower structure, which decreases both generator and tower costs. A major drawback of the air-cored type of machines is that they require a relatively large amount of PM material to maintain the required air-gap flux density. The active mass of the generator, i.e. the PM and copper material, are more expensive per mass compared to the rest of the materials the turbine consists of. Since the cost of the active material is determined largely by the amount of the material used, it would be advantageous to minimise the mass of these materials specifically. The non-active parts of the generator can also be optimised in terms of mass and cost. Mechanical strength analysis permits components to use less material and could possibly require less labour.

The optimisation of the RFPM generator discussed in this section, is aimed to minimise the mass and the cost of the machine simultaneously. Two main categories are considered in optimisation procedures: (a) Minimisation of the active mass of the RFPM generator (that is the amount of PM, copper and iron material used in the generator rotor and stator) (b) the introduction of a new stator design. The optimisation procedure discussed in sections 2.3.1 through 2.3.3 is published in [30].

2.3.1 Mathematical model

To optimise RFPM generator design an analytical approach is used. For this a mathematical model is introduced. The required performance of the RFPM generator and the dimensional parameters that have to be optimised in the design are defined respectively in matrix-format by $\mathbf{U}$ and $\mathbf{X}$ as [30]

$$\mathbf{U} = \begin{bmatrix} P_d \\ \omega_m \\ \eta_g \end{bmatrix}; \quad \mathbf{X} = \begin{bmatrix} d \\ l_a \\ h \\ h_m \\ h_y \end{bmatrix} \tag{29}$$

Among the required performance parameters is the developed power of the generator, P_d, the mechanical rotating speed of the rotor, ω_m, and the generator efficiency, η_g. Parameters to be optimised include the average stator diameter of the RFPM generator, d, the stator winding's active length, l_a, the stator thickness in the radial direction, h, the magnet height, h_m, and the rotor yoke thickness, h_y. Two important required performance parameters of the generator that are functions of $\mathbf{X}$, namely the developed torque $T_d(\mathbf{X})$ and the copper losses $P_{cu}(\mathbf{X})$, can be determined from the known required performance given in (29) as [30]

$$\mathbf{G} = \begin{bmatrix} T_d(\mathbf{X}) \\ P_{cu}(\mathbf{X}) \end{bmatrix} = \begin{bmatrix} 1/\omega_m \\ k(1-\eta_g) \end{bmatrix} P_d, \tag{30}$$

where $k < 1$ gives the ratio of the copper losses to the total losses of the machine. As the air-cored stator winding RFPM machine has practically no iron losses, and if the mechanical wind and friction losses are ignored in the design optimisation, the only remaining losses in the machine are the copper losses, P_{cu}, and the eddy-current losses in the stator winding, P_{eddy}. Hence, k of (30) is given by [30]

$$k = \frac{P_{cu}}{P_{cu} + P_{eddy}}. \tag{31}$$

The eddy-current losses in air-cored stator winding PM machines can be calculated from (28). The eddy current losses can be made substantially smaller by using parallel connected coils and parallel stranded wires to reduce the conductor diameter d_c in (28), as described by [29]. In practice k can be taken in the design in (30) as between $2/3 < k < 1$ and a typical value to start with is $k = 0.7$; if this value is difficult to apply in practise, then k can be adjusted and the machine can quickly be re-optimised in its design. Note that to include the eddy-current losses as part of the design optimisation, makes the design optimisation unnecessarily difficult.

Torque

As derived in [25], [28] and [29] for radial flux, axial flux and linear PM air-cored stator machines, the developed torque of the generator can be expressed by

$$T_d = k_w C_1 K_1, \tag{32}$$

where k_w is the stator winding factor (derived in Appendix E), C_1 is a function of the copper losses and is given by [30]

$$C_1 = B_1 \sqrt{\frac{\pi P_{cu} \kappa k_f}{2\rho_t}} \cos\delta \tag{33}$$

and K_1 is a machine constant as a function of d, l_a and h of (29) as

$$K_1 = \sqrt{\frac{h l_a d^3}{2(1 + k_e d/l_a)}}, \tag{34}$$

where k_e is the end winding constant derived in the Appendix E. The current angle, δ, of (33) depends on the system (Fig. 6) to which the generator is connected. It is important to point out that the constant K_1 of (34) can be calculated from the known (required) torque of (30) and from (32) and (33) as

$$K_1 = \frac{T_d}{k_w C_1} \tag{35}$$

Copper losses

The copper losses in the stator winding of Fig. 11 can be expressed as

$$P_{cu} = C_2 K_2, \tag{36}$$

where C_2 is a constant given by

$$C_2 = 2\pi\kappa k_f \zeta_{cu} J^2 \tag{37}$$

and K_2 is another machine constant, but also a function of d, l_a and h which can be expressed as

$$K_2 = h l_a d (1 + k_e d/l_a). \tag{38}$$

The current density, J, of (37) must be selected in the design. The selection of J plays an important role in the outcome of the design, as is showed in the next section. Similarly to (35), K_2 can be calculated from the known (calculated) copper losses of (30) and from (36) and (37) as

$$K_2 = \frac{P_{cu}}{C_2}. \tag{39}$$

Stator Length and Diameter Relationship

A relation between the axial length, l_a, and the diameter, d, of the stator winding can be derived from (34) and (38) by taking

$$\frac{\sqrt{K_2}}{K_1} = \sqrt{2}\left(\frac{1}{d} + \frac{k_e}{l_a}\right).$$

(40)

From (40) it follows that

$$l_a = \frac{k_e}{K_3 - 1/d} \quad \left\{K_3 = \frac{\sqrt{K_2/2}}{K_1}\right\}.$$

(41)

According to (41), there exists a functional relationship between l_a and d of the stator winding, independent of h. Hence, if d is chosen, then l_a can be determined from (41). With l_a and d known, h can be determined from (38). In this way, three of the important dimensional parameters of (29) that satisfy the required performance **U** and **G** of (29) and (30) of the generator can be determined.

Magnet and Yoke Heights

The remaining dimensional parameters that have to be determined in the design according to (29) are the magnet height, h_m, and the yoke height, h_y, of the generator. These heights must be designed in such a way that the required flux density in the air gap is obtained. The flat-topped trapezoidal shaped air gap flux density waveform is shown by in Fig. 15.

The electromagnetic design of the magnet and yoke heights depends on the permeability and BH-characteristics of the magnet and yoke material. Due to the relatively large air gap of the air-cored stator RFPM machine, high energy product rare-earth magnet material must be used for the permanent magnets. For the solid rotor yokes, mild steel material is used. The BH-characteristics of NdFeB magnet material (grade N48) and mild steel are shown in Fig. 16. Due to the large air gap the rotor yokes can be put fairly deep into saturation before they start to increase the magnetic circuit reluctance substantially. By choosing a fixed value for the yoke flux density, B_y, the magnetic field strength in the yoke, H_y, can be determined from the mild steel BH-curve, as shown in Fig. 16; typical values are $B_y = 1.5$ T and $H_y = 4000$ At/m.

Consider a permanent magnet pole that generates a MMF of $F_g = I_m = H_c h_m$ across the magnetic ciruit, then the MMF equation for the magnetic circuit can be written as

$$H_c h_m = H_m h_m + 0.5 H_g l_g + H_y l_y,$$

(42)

where l_g and l_y are lengths defined in Fig. 11 and given by

$$l_g = h + 2g$$
$$l_y = \frac{\pi d}{2p} \qquad (43)$$

From Fig. 16 the permeability of the magnet material can be determined as $\mu_m = B_r/H_c$. From this and by taking the flux density in the magnet the same as in the air gap, (42) can be expressed as

$$H_c h_m = B_g \left(\frac{H_c}{B_r} \right) h_m + \left(\frac{B_g}{\mu_0} \right) \frac{l_g}{2} + H_y l_y. \qquad (44)$$

By re-arranging (44), the magnet height can be calculated as

$$h_m = \frac{B_g l_g + 2\mu_0 H_y l_y}{2\mu_0 H_c \left[1 - B_g / B_r \right]}. \qquad (45)$$

As half of the flux per magnet pole is set up in the back iron yoke, the yoke height can simply be calculated from the ratio of the air gap and yoke flux densities as

$$h_y = \frac{\pi d \tau_m}{2p} \left(\frac{B_g}{B_y} \right), \qquad (46)$$

where τ_m is given in (14).
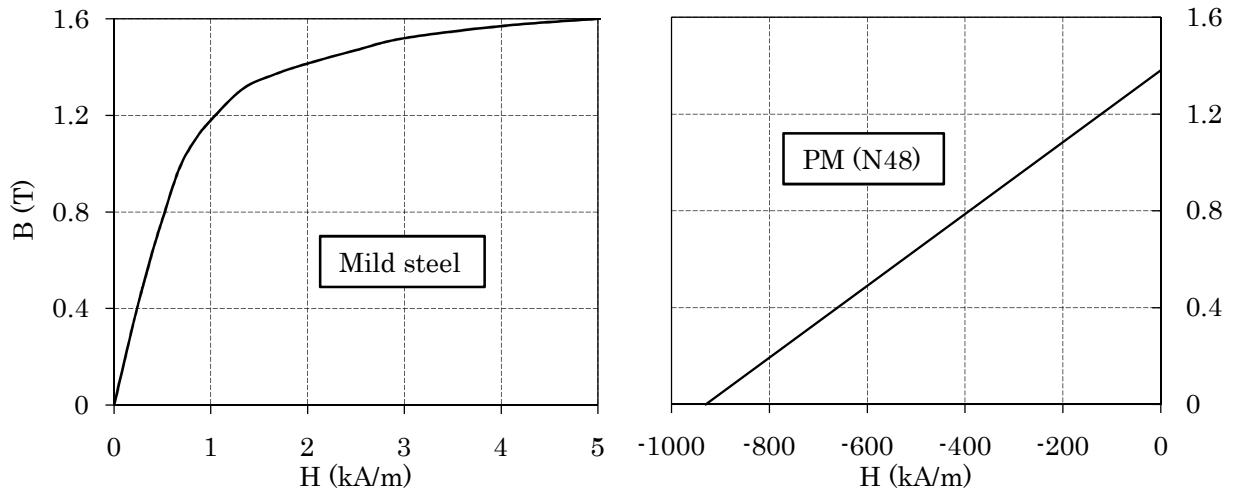
Fig. 16: BH-characteristics for mild steel (left) and NdFeB (N48) permanent magnets (right).

Active Mass

With **X** of (29) calculated, the active mass of the double rotor air-cored stator RFPM machine can be determined. This mass consists of the mass of the permanent magnets, the stator copper and the rotor yokes. The mass of the permanent magnets, M_m, and rotor yoke materials, M_y, are respectively given by

$$M_m = 2\pi\rho_m\tau_m h_m l_a d \tag{47}$$

and

$$M_y = 2\pi\rho_{fe} h_y l_a d \,, \tag{48}$$

where ρ_m and ρ_{fe} is the density of the permanent magnet material (NdFeB) and the yoke material (mild steel) respectively. The stator copper mass can be determined as

$$\begin{aligned} M_{cu} &= 2\pi\rho_{cu}\kappa k_f \, hl_a d\left(1 + k_e d/l_a\right) \\ &= 2\pi\rho_{cu}\kappa k_f K_2 \end{aligned} \tag{49}$$

with ρ_{cu} representing the density of copper. Substituting (38) and (36) into (49) results in an equation for the copper mass as

$$M_{cu} = \frac{P_{cu}\,\rho_{cu}}{\zeta_{cu}\,J^2} \tag{50}$$

This is an interesting result as the copper mass is independent of **X** of (29); it is not necessary to consider the copper mass in the design optimisation of **X** as it is a constant. However, the determined P_{cu} and the chosen J in (50) are important parameters in the final outcome of the generator design.

Leakage flux constraints

Due to the relatively large air gap of the air-cored stator PM machine a high amount of leakage flux can easily be set up tangentially between adjacent magnets in the air gap. This is particularly prevalent in machines with higher pole numbers, since the permanent magnets are placed closer together. This tangential leakage flux in the air gap must be minimised as it is detrimental to the performance of the machine [31]. A solution to this is to minimise the pole count. On the other hand, flux can also leak from the magnet pole edges directly back to the iron yoke. This is more likely at low pole numbers. To counter this, the number of poles is increased to a higher value to minimise the flux per pole and, thereby, the required rotor yoke thickness and thus the rotor mass of the machine. Care should be taken not to increase the poles too far as leakage flux between the neighbouring permanent magnets will then increase as well. Both leakage flux cases are shown in Fig. 17. To ensure minimum leakage flux or else to ensure strong radial flux between opposite poles, the design of the machine is subjected to the following constraints:
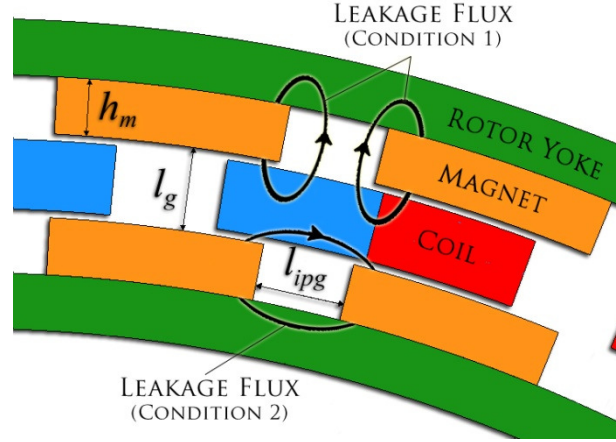
Fig. 17: Two different kinds of leakage flux caused by the permanent magnets.

$$h_m \geq 0.5\, l_g \qquad \qquad \text{(Condition 1)}$$
$$l_{ipg} = \frac{\pi d_i}{p}(1 - \tau_m) \geq l_g \quad \text{(Condition 2)} \tag{51}$$

where d_i and l_{ipg} are as defined in Fig. 11. Often these two constraints make many optimisation designs invalid, in which case d and/or p must be altered. These constraints are therefore responsible for optimising the number of PM poles. The pole count affects both the mass and the rotor yoke thickness.

2.3.2 Constant parameters

Before the optimisation procedure can start, a couple of constant generator parameters and design constraints need to be established.

Firstly, the current density is varied manually in the design optimisation as a parameter to get the best result, however only designs where $J < 5$ A/mm² are accepted. As given in Table 1, different pole numbers are used in the design optimisation of the generator to determine the best choice.

In Fig. 6a, $L_e \gg L_i$, so that L_e can be determined beforehand as $L_e = 1.5$ mH according to the chosen cut-in and rated operating points of the turbine-generator system [32]. This determination of L_e is described in a later section. From this, the current angle for the wind generator system at 80 Hz with $p = 32$ is determined approximately as $\delta = 52°$, which results in $\cos(\delta) = 0.616$ as given in Table 1 and used in (33).

To ensure an average air-gap flux density of 0.7 T, the flux density in the design is taken a fraction higher than 0.7 T namely as $B_g = 0.725$ T. This results in $B_{p1} = 0.774$ T according to (13). The optimal winding design and harmonic analysis in [29] show that a per unit coil side width of $\kappa = 0.37$ and a per unit magnet pitch of $\tau_m = 0.7$ can be used in the design optimisation. The temperature of the stator winding is taken as fairly high, namely as 80 °C, which results in the resistivity as given.

Table 1: Constant parameters and design constraints.

$B_{p1} = 0.774$ T	$\kappa = 0.37$	$\tau_m = 0.7$	$J < 5$ A/mm^2
$k_f = 0.42$	$g = 1$ mm	$k_w = 0.875$	$\cos(\delta) = 0.616$*
$p = 24, 28, 32, 36, 40$	$B_r = 1.38$ T	$H_c = 923$ kA/m	$\zeta_t = 2.1$ x 10^{-8} Ωm
$\rho_{fe} = 7800$ kg/m^3	$\rho_{cu} = 8100$ kg/m^3	$B_y = 1.55$ T	$H_y = 5$ kA/m

* with $p = 32$ and 300 r/min

Finally, the values of the magnet coercivity, H_c, and magnet remanence, B_r, depend on the chosen magnet grade. A summary of the constant parameters and design constraints are given in Table 1.

2.3.3 Optimisation procedure

The mathematical model and constraints discussed in the previous section are used in a case study to optimise the design of a 4.2 kW air-cored RFPM wind generator prototype. The optimisation specifically minimises the active mass of the generator, as well as the non-active mass of the rotor yokes. The construction mass is not considered in this section but rather in Chapter 3.

Wind Generator System and Specifications

The air-cored RFPM wind generator is designed to operate in a direct battery charging system as shown in Fig. 6a. The DC output of the diode rectifier in this case is connected directly to the battery bank to keep the system as simple and cheap as possible. The batteries are protected against over-charging by dissipating the excess energy into a parallel connected resistor bank.

Connecting an air-cored generator with its low internal inductance directly to a diode rectifier causes the generator current to become non-sinusoidal and the generator to be very noisy. Also, good turbine power matching is only obtained at a small range of wind speeds. To solve these two problems a three-phase external inductor, L_e, is used in series with the diode rectifier to act as an additional series reactance $Z_e = jX_e = j\omega L_e$ as shown in Fig. 6a; this solution has been proposed and analysed in detail by [32]. However, the use of an additional series inductance comes at the expense of a large current angle δ as shown in Fig. 6a and an oversized generator.

For this application the turbine-generator's rated operating point is chosen to be at 12 m/s and 300 r/min of turbine speed, which, according to the turbine blade power curves, gives a rated turbine-generator power of 4.2 kW. The cut-in operating point is chosen at 3 m/s of wind speed and 100 r/min of turbine speed. Further discussion on how these two operating points are chosen will occur in a later section. The efficiency of the relatively small direct drive generator is chosen to be not less than 90 %, but a higher efficiency is not chosen as it would considerably increase the size of the generator, which is already operating at a large (poor) current angle. The required generator performance **U** of (29) is, thus, given by

$$\mathbf{U} = \begin{bmatrix} P_d \\ \omega_m \\ \eta \end{bmatrix} = \begin{bmatrix} 4200 \\ 31.42 \\ 0.9 \end{bmatrix}. \tag{52}$$

From (52) and (30) it follows that

$$\mathbf{G} = \begin{bmatrix} T_d \\ P_{cu} \end{bmatrix} = \begin{bmatrix} 134 \\ 294 \end{bmatrix}, \tag{53}$$

with k of (30) and (31) taken as $k = 0.75$.

Magnet grade

Permanent magnets can be manufactured from various alloys. Some of the alloys that produce the strongest permanent magnets consist of what are known as "rare-earth" materials, often misunderstood as consisting of rare or precious materials. These include samarium-cobalt ($SmCo_5$) and neodymium-iron-boron ($Nd_2Fe_{14}B$) magnets of which the latter has the higher energy density. A major advantage of using permanent magnets instead of excited electromagnets is the absence of excitation losses. Furthermore, carbon brushes are no longer required. This means better generator efficiency. In this design the neodymium-iron-boron, or NdFeB for short, magnets are used.

One of the first parameters to be optimised is the magnet grade. The question in relation to permanent magnet mass, cost and strength is if a low or a high grade magnet must be chosen. When a lower grade magnet is chosen, the magnet could potentially be cheaper but will also require more material. A higher grade magnet requires less material, and thus mass, but could be more expensive.

To investigate this, a study was conducted to determine the magnet cost and magnet mass versus magnet grade for a given air-gap flux density. This led to the surprising result shown in Fig. 18. The graphs illustrate a large reduction in magnet mass (diamonds) with only a marginal increase in magnet cost (circles). The consequence of this, thus, is that the strongest magnet grade must be chosen in the design optimisation, namely in this case the N48.
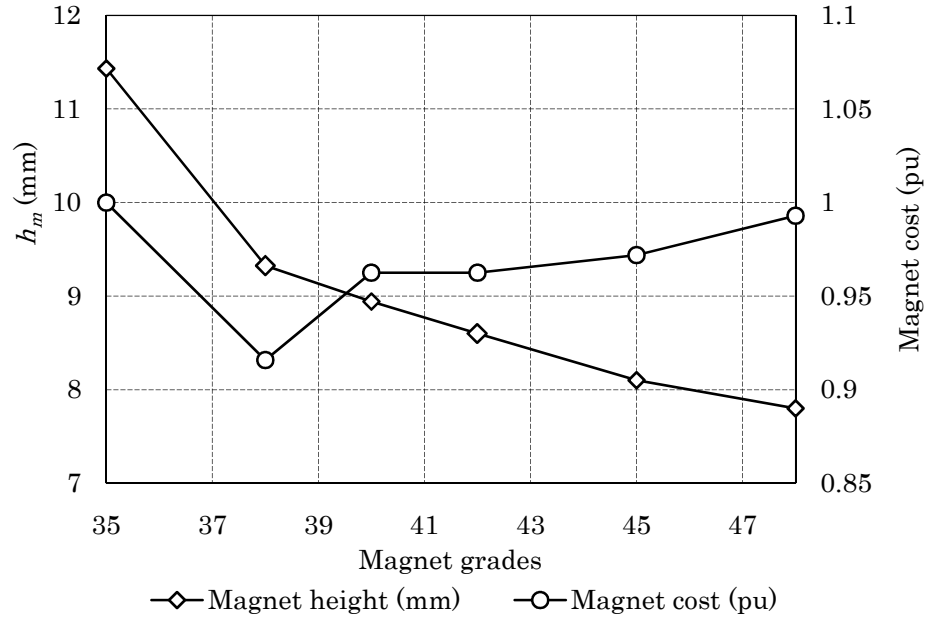
Fig. 18: Magnet grade versus cost and height (Cost values obtained in May 2009).

Objective function optimisation

As can be seen from (47) and (48), the mass equations of both the magnet and yoke material are functions of $\mathbf{X}$ of (29). These two parameters are directly responsible for the generator mass. It is these two variables that need to be optimised analytically to decrease the generator mass and cost while simultaneously adhering to the constraint parameters mentioned in the previous section. Hence, the objective function, $\mathbf{F(X)}$, to be minimised subject to the performance constraints in (52) and (53) and the leakage flux constraints of (51) can be estimated as

$$\mathbf{F(X)} = w_1 M_m(\mathbf{X}) + w_2 M_y(\mathbf{X}) , \qquad (54)$$

where w_1 and w_2 are cost weighting factors and $\mathbf{X}$ is the dimensional vector of (29) containing the machine variables to be optimised. The cost weighting factors are directly equivalent to the cost of the yoke and magnet materials plus labour at a given time. At the time of publication the weighting factor for the magnets, w_1, is considerably larger than that of the steel yokes. Note that M_{cu} is not included in (54) since it is a constant according to (50). M_{cu}, however, should be included in the total active mass when comparing optimum designed generators with different pole numbers.

The first step in the design optimisation is to calculate the constants K_1, K_2 and K_3 according to (35), (39) and (41) respectively. The next step is to vary the diameter d and calculate for each d a unique value for l_a for each d from (41), and then calculate unique values for h, h_m and h_y by (38), (45) and (46) respectively. From this M_m and M_y are calculated respectively by (47) and (48), and finally $\mathbf{F(X)}$ is calculated by (54). The d-value is changed in steps from an initial value until the minimum of the function is obtained. At each d-value the leakage flux constraints of (51) are

checked, and if one or both of these constraints are not satisfied, then that design is marked as invalid. The whole design optimisation can be implemented in a simple spreadsheet program. The different pole numbers given in Table 1 have been investigated in the design optimisation. For each pole number the current density has been varied to get an optimum and valid design. The outcome of this investigation shows clearly that the higher the pole number, the lower the active mass. However, high pole number designs tend to have large diameters, which might become impractical and/or which might increase the construction-mass of the generator. Also with higher pole numbers the generator supply frequency is higher, which, amongst other things, takes more effort to keep the eddy current losses within limits. From this investigation a pole number of $p = 32$ has been chosen for the air-cored stator RFPM generator.

The variations of the dimensional and mass parameters of a 32-pole wind generator with machine diameter d are shown in Fig. 19 and Fig. 20. First it is shown that for diameters between $364 \leq d \leq 424$ mm, the designs are invalid as (51) is not satisfied. Secondly, it can be seen from Fig. 20 that if the magnet mass is minimised at all costs, i.e. with $w_1 >> w_2$ in (54), it leads to very large machine diameters that increases the construction mass. It is better and more practical to rather minimize the total active mass of the generator ($w_1 = w_2$); the optimum result then is at $d = 504$ mm. Due to the turbine blade dimensions, however, the generator diameter is limited to $d \leq 464$ mm, which from Fig. 20 still gives a good result in terms of minimum active mass. The optimum design results of the air-cored stator RFPM generator at $d = 464$ mm are summarised in Table 2. Note that an aspect ratio (l_a/d) of just lower than 20 % and a total active mass of $M_t = 31.8$ kg are found.
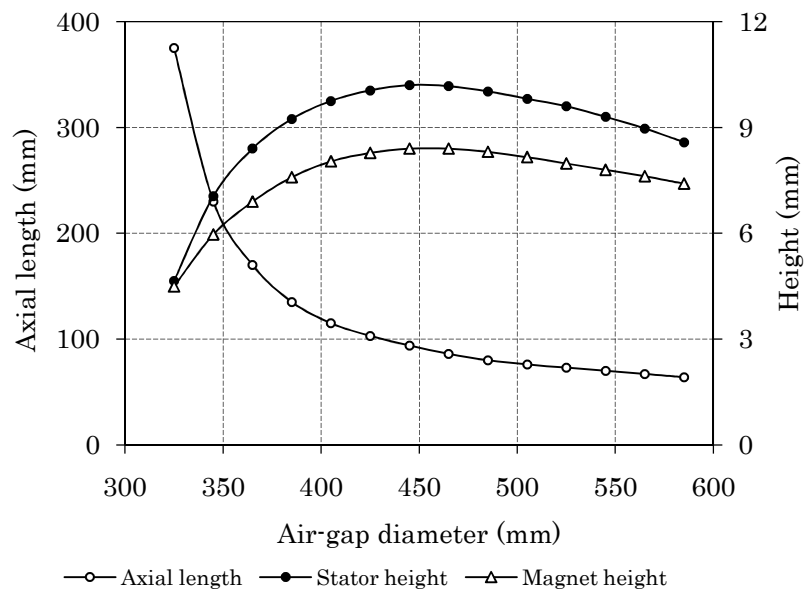
Fig. 19: Length and height versus diameter of the RFPM air-cored generator.
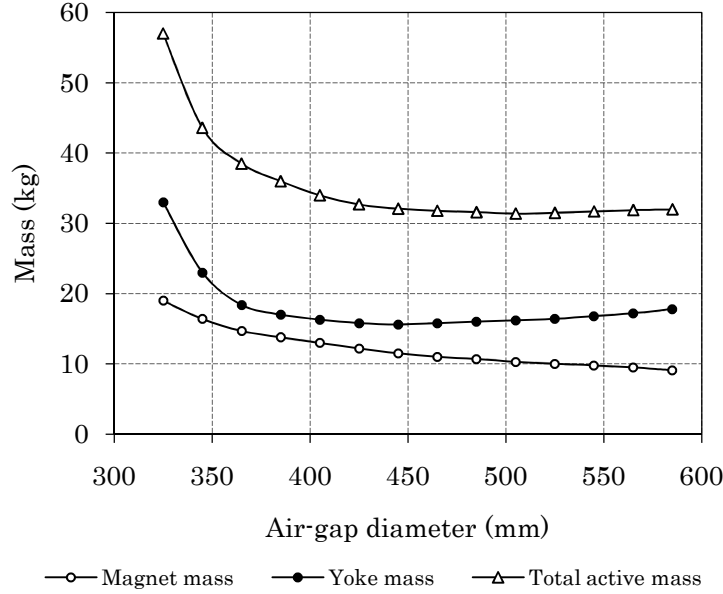
Fig. 20: Mass versus diameter of the RFPM air-cored generator.

Table 2: Optimum design results.

$p = 32$	$l_a = 84.9$ mm	$h_y = 7.97$ mm	$M_m = 11.06$ kg
$J = 5$ A/mm²	$h = 10.05$ mm	$l_a/d = 0.183$	$M_y = 15.38$ kg
$d = 464$ mm	$h_m = 8.91$ mm	$M_{cu} = 5.36$ kg	$M_t = 31.8$ kg

2.3.4 New stator design

The copper coils in the stator of an air-cored generator are held together by a non-magnetic epoxy resin. Prior to curing, the resin liquid is poured into a mould where it penetrates all areas between and inside the copper coils. Once the resin is hardened it creates a strong bond between the copper coils. This bond is so strong that it becomes impossible to successfully remove a coil from the epoxy without causing irreparable damage to the stator. This creates a major concern. If a whole stator is manufactured and a single coil becomes faulty it would mean that the entire stator would become useless since there is no way of replacing only that one coil.

Taking this into account, a further design optimisation has to be done on the stator. One way to counter this problem would be to design a segmented or modular stator which would allow easy replacement of individual or groups of faulty stator coils. This design would mean that it would be possible to replace only the defective coils and not the entire stator. The new sectioned stator design, shown in Fig. 21, has three coils situated in a removable segment. Because of the concentrated coil topology, each segment has an embedded A, B and C phase coil. A single section can in effect be seen as a generator in itself producing a fraction of the total power. Sections are electrically connected by means of embedded connectors protruding from the back of each section. Another advantage of this stator design is that the coils can be connected in series, parallel or in any combination of the two.
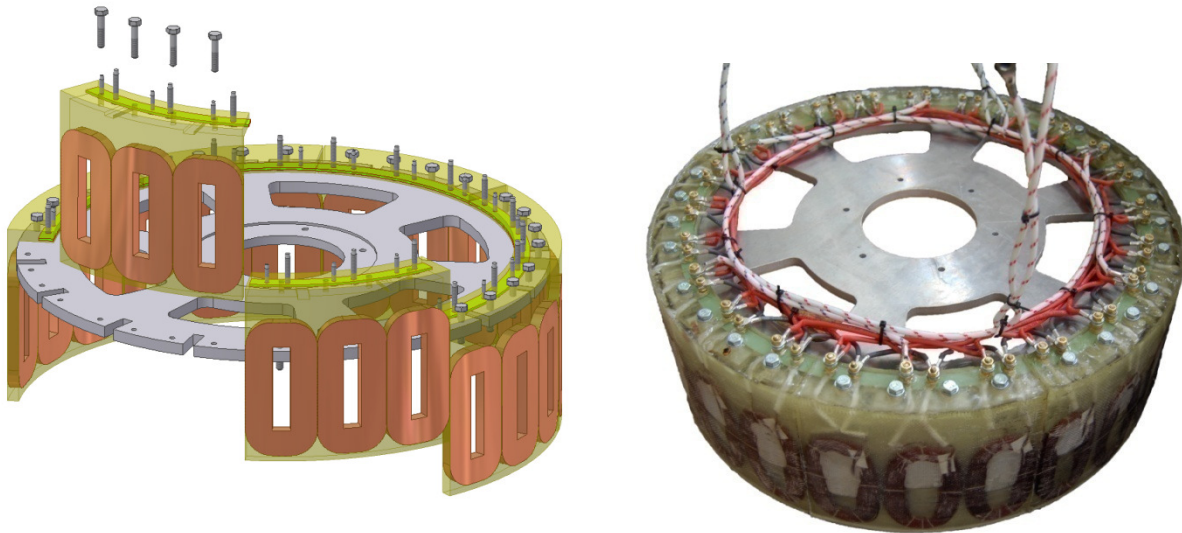
Fig. 21: New segmented stator. CAD design (left) and actual prototype (right).

This makes it possible for a generator to function either as a high voltage or as a high current machine by simply changing the electrical connections of each section. No redesign is necessary.

Mechanical considerations relevant to the stator, together with the manufacturing process are discussed in later sections.

2.4   Finite element analysis of the RFPM generator

To verify the analytical results of the previous sections, finite element analysis is performed on the RFPM air-core generator.

2.4.1 The FE model description

In a radial flux machine the magnetic flux changes in both radial and tangential directions. Little flux variance occurs in the axial direction provided that the modelled area lies in the active area of the stator windings and magnets. Phenomena occurring beyond these boundaries are negligible. To simulate a RFPM generator, a model is drawn which represents a cut-through perpendicular to the radial direction, with the model's depth being in the axial direction. This is a 2D analysis.

To reduce simulation time, the machine can be divided into similar symmetrical sections. If similar sections are repeated, so will the calculations to solve these pieces. Simulation time is reduced by the solving of a single symmetrical section instead of the entire machine.

For large radius RFPM generators it can be assumed that the generator has axial symmetry around the centre of the air-gap. This allows for the model to be cut in two equal halves around its circumference on the average stator diameter, *d*. This means that the model is mirrored on the

average stator radius, r_e. Each half consists of one PM rotor yoke, the PM material, an air-gap and half of the air-cored stator. A boundary condition is set on this plane to allow the machine model to be mirrored on the opposing side. This is referred to as the Neuwmann boundary condition [24].

Furthermore, the machine model can also be symmetrically divided into 8 equal coil group sections. These "pizza slices" each contain four permanent magnets and three coils (one representing each phase). Positive periodical boundary conditions are applied to the ends [24], which means that the machine is simply repeated beyond this boundary.

Both of these methods allow for a smaller machine model to be solved, which saves a considerable amount of computation time. Fig. 22 shows both symmetries and their respective applied boundary conditions.

The mesh of a model, which is made up of a number of triangles each connected at their ends, can be altered by the user. Areas where greater accuracy is needed, for instance in the air-gap, can be altered to have a finer mesh. Finer meshes, however, make for longer computation times since more nodes need to be solved.

2.4.2 Magnetic flux

Magnetic flux can be calculated by using FE analysis. Accurate magnetic flux calculation is important to ensure that the required peak air-gap flux density of B_{p1} = 0.774 T, as given in Table 1, is maintained. If this flux density is not within specified levels the machine performance is affected greatly. Since the RFPM generator has such a large effective air-gap a high magnetic field strength is required. The field strength in a PM generator is directly proportional to the strength of the magnets. For this reason rare-earth magnets, NdFeB grade N48, are used in this air-cored machine.
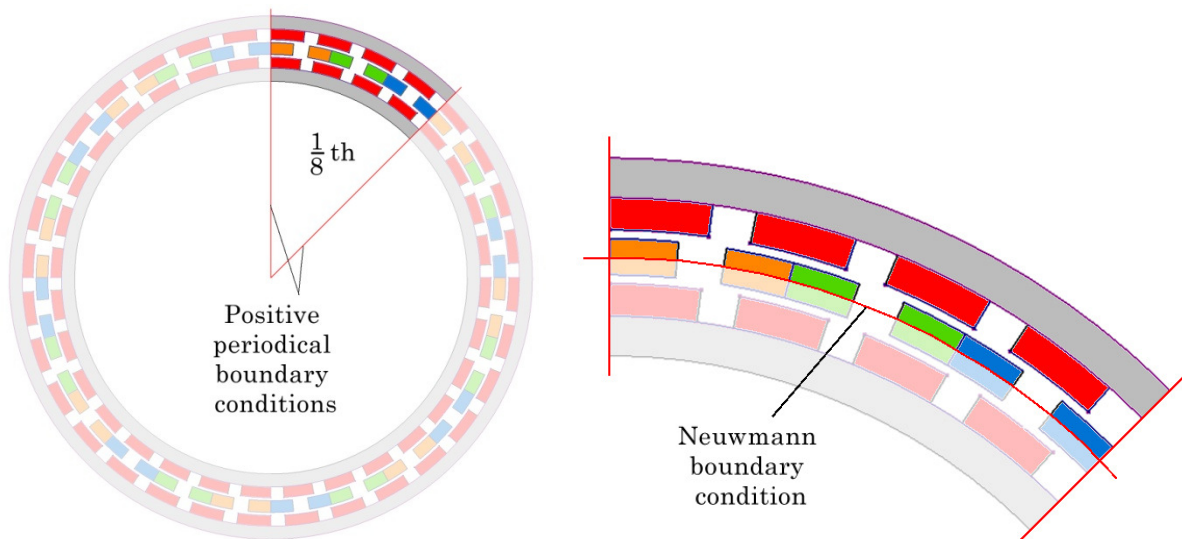

Fig. 22: Generator symmetry and boundary conditions.
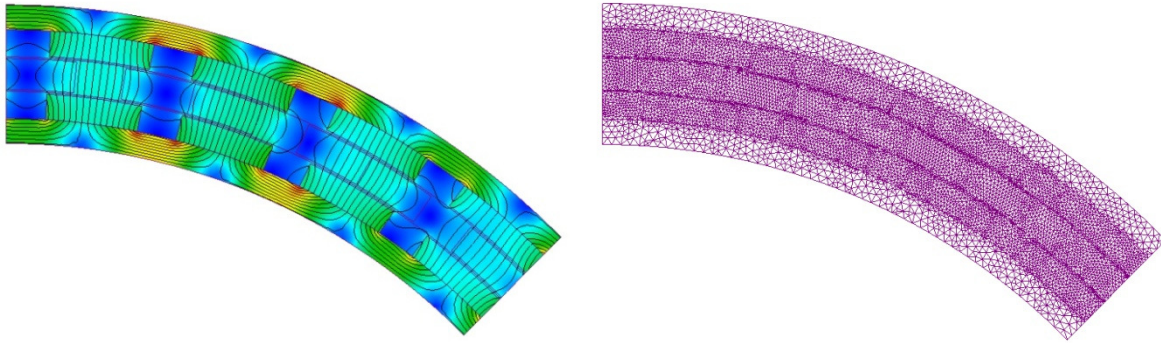
Fig. 23: Magnetic flux plot in a machine section (left) and solution mesh plot (right) of an RFPM air-cored generator.

In iron-cored machines an effect called armature reaction causes the magnetic flux in the stator and rotor to distort. Armature reaction is caused due to the armature flux generated by the current carrying coils that oppose the main permanent magnet flux [37]. This has a demagnetizing effect and produces core losses. In an air-cored machine these magnetic flux distortions can be ignored because of the large effective air-gap present between the rotor magnets. The armature reaction effect becomes negligible. This creates a major advantage because there are almost no eddy-currents, and therefore no core losses, induced in the permanent magnets or steel back yokes. The yokes can thus be manufactured from solid steel, as opposed to the laminated steel needed in iron-core generators [24].

The flux density plot in the middle of the air-gap is also simulated with FE analysis. The plot is shown to be of a semi-trapezoidal form as stated earlier. The magnetic flux plot for a section of the machine can be seen in Fig. 23.

2.4.3 Rotor yoke FE analysis

To minimise the RFPM generator's mass the rotor yoke has to be optimised. One previously mentioned function of the yoke is to serve as a return path for the magnetic flux of the permanent magnets. It now also becomes imperative to consider the electromagnetic aspects of the yoke optimisation since a consideration such as flux saturation can also affect machine performance.

The non-linear electromagnetic properties of ferromagnetic steel can be seen in the BH-curve of Fig. 16. It can be seen that the relationship between the magnetic flux density, B, and the field intensity, H, is not linear. In steel, magnetic saturation occurs at higher field intensities and at some point B ceases to increase even though H is still increasing [33]. The gradient of the plot is constant until about 750 A/m, after which the slope begins to decrease as saturation occurs.

Electromagnetic finite element (FE) simulations of the rotor yoke show clearly that the cylinder rotor yoke starts to saturate in terms of magnetic flux if the yoke thickness becomes too small. This magnetic flux saturation causes a decrease of flux density in the air-gap and the performance of the

machine is affected greatly. A simulation of the magnetic saturation in the RFPM generator yoke is shown in the FE field plot of Fig. 24. Magnetic flux lines in this figure are only plotted for the outer half of the machine. As is clear, magnetic saturation occurs in the steel yoke between the opposite magnet poles. To maintain the required peak air-gap flux density at 0.774 T, the FE electromagnetic analysis shows that the yoke thickness must not decrease below 8 mm. From an electromagnetic point of view the optimum yoke thickness, thus, is 8 mm. This corresponds closely to the 7.97 mm optimum design results obtained analytically as shown in Table 2. Further mechanical strength analysis and optimisation on the rotor yokes is discussed in section 3.2.1.

2.4.4 Magnetic attraction forces

The inter magnet attraction forces present between each opposite rotor magnet should also be calculated with FE analysis. As is shown in section 3.2.1, these forces are dependent, amongst others, on the average air-gap flux density, the permeability of air and the cross-sectional area between the two magnets. By doing a steady-state FE simulation on the generator model, one can calculate the force exerted on a particular magnet by the magnet opposite to it.

2.4.5 Back-EMF

It is possible to calculate the back-EMF of the stator windings with transient FE analysis by applying a constant rotational speed on the open circuit generator rotor. The model is in essence open-circuit since no current is flowing in the coils. By using the flux linkage of the windings and Faraday's Law, the back-EMF voltage can be calculated by the FE program. Since the flux linkages in the windings of an air-cored generator are nearly sinusoidal, so is the back-EMF voltage.
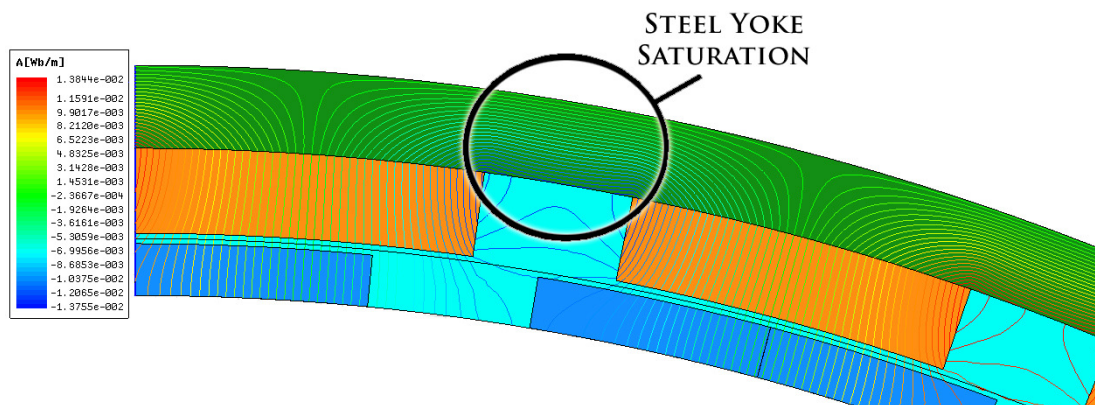

Fig. 24: Saturation occurring in rotor yoke between the magnets.

2.4.6 Developed torque

The developed torque, or electromagnetic torque, of the generator is calculated by FE analysis. It is the magnetic force in the tangential direction between the rotor and stator multiplied by the radius at which the force occurs. In this simulation the rated current of the generator is applied in the stator winding which creates the rated torque. The machine is essentially modelled as a motor since the current in this case is not induced by the rotating magnetic field as in a generator, but rather vice versa. The FE phase currents are 120 degrees out of phase with the fundamental component realised by means of a current source in the analysis. This is a good approach since the currents in an air-cored generator are sinusoidal when they are connected either to a pure resistive load or to an inverter. It should be noted, however, that the true currents induced in an air-cored generator connected to a battery load are only quasi-sinusoidal. Because of this, the battery loaded generator simulation approach tends to have some minor inaccuracies. As will be shown in the current test measurements of chapter 4, this is a reasonable approach.

Torque ripple

The developed torque exerted in PM iron-core machines operating at their rated speed is not a constant value. The electromagnetic torque of these machines has what is known as a torque ripple superimposed on top of the fundamental torque. Torque ripple has two primary causes. The first cause is cogging torque. Cogging torque is created by the rotor flux interacting with the stator slots. The second cause is mutual torque ripple. Mutual torque ripple is due to the magnetic saliency of the rotor [34].

In an air-cored generator there exists no attraction force between the permanent magnets on the rotor and the stator slots because of the non-magnetic slot-less nature of the stator. For this reason no cogging torque exists in these machines [36]. This condition is very advantageous since it allows this type of generator to start operating at much lower wind speeds. The air-cored generator does however have some mutual torque ripple. This is due to the current distribution with respect to the rotor that repeats itself every 60° [24]. This repetition causes a harmonic of the 6th order on the torque waveform.

Fig. 25 shows the FE results of the battery connected system with $\delta = 52°$, and the resistive load system with $\delta \approx 0°$. The dc-developed torque value with the superimposed torque ripple can be seen in both cases. The torque ripple is about 1.5 % of the 133 Nm dc-torque value.
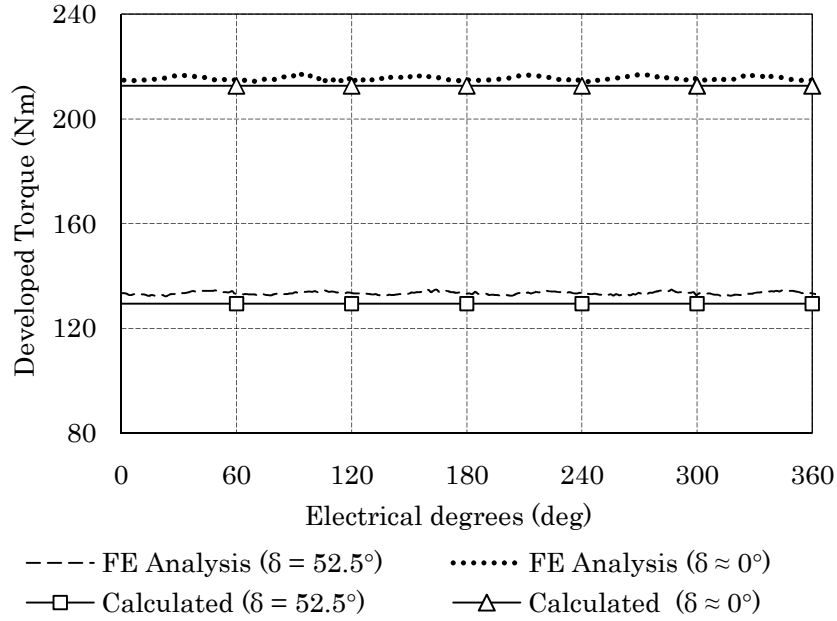
Fig. 25: Analytical and FE results of developed torque on a battery loaded system ($\delta = 52.5°$) and a resistor loaded system ($\delta \approx 0°$).

2.5   Analysis of the battery charging system

Because of the erratic nature of wind, there will be times that the generated power will not match the amount required by the load. Some means of storing the surplus generated power, when the generator supply outweighs the load demand, needs to be developed. This surplus must be stored to be available at times when the generation has stopped but the load still requires energy. This can be realised by implementing a battery charging system in which the wind turbine can operate. In this section the battery charging system is discussed shortly. It is important to ensure that the wind turbine, the electric generator and the transmission, conversion and storage system are all optimally matched. This ensures a better overall energy yield. More extensive research on the sub-system was done by [24], and some of those findings will be used in this section.

Fig. 6a shows how the system components are interconnected. The wind turbine is coupled directly to the RFPM electric generator. The generator is coupled to an additional external inductance L_e of which the value is determined in this section. The inductance is coupled directly at the ac-side of the diode rectifier by means of a cable. The dc-side of the rectifier is then coupled to the battery bank. Systems like these normally have battery charge controllers but since these are active only for small time periods these will be omitted from the analysed system.

The reason for inserting the external inductance into the system is due to the fact that air-cored generators, unlike iron-cored generators, have a very low internal inductance which gives rise to some negative effects on its performance. Amongst these are the non-optimal wind turbine power

matching and the non-sinusoidal line currents caused by the diode rectifier [24]. The harmonics present in the line current also emit a severe acoustic noise from the generator. It has been shown that inserting an external reactance (inductive or capacitive) does counter these negative effects [32], [15]. It should be noted, however, that inserting this external inductance also has a direct effect on the current angle of the system [30].

2.5.1 Equivalent system circuits

Fig. 26 shows the RFPM air-cored generator incorporated into the battery charging system to form a more detailed steady state per phase equivalent wind power system circuit diagram. In this diagram the wind turbine is coupled directly to the RFPM generator. The turbine generates a developed torque, T_d, at a mechanical rotation speed of ω_m. The generator's back-EMF voltage E_g is in series with its internal resistance, R_i, and its internal inductance, L_i. V_t is the RFPM machine's generated voltage measured at the generator terminals. The generator is connected to the three phase bridge rectifier through the proposed external inductor with an inductance, L_e, and a resistance, R_e. The arrow through the inductor symbol indicates that the inductance value is changeable depending on the wind generator characteristics. V_{rec} is the voltage measured on the ac-side terminals of the diode rectifier. The battery bank internal resistance, R_{dc}, as described by [24], is located in series with the battery bank's voltage V_{bat}. The battery bank is connected directly to the rectifier with the diode's dc-terminal voltage given as V_{dc}. I_{ac} and I_{dc} are the line currents on the ac- and dc-side of the diode rectifier respectively.

Complicating the system analysis are the non-linear characteristics of the battery bank load. The battery load voltage varies, amongst others, depending on the state of charge. For instance, a fully charged battery has a slightly higher terminal voltage than a nearly depleted battery. In order to analyse the system successfully, the battery bank needs to be converted to an ac-equivalent circuit model to ensure a linear steady state system.
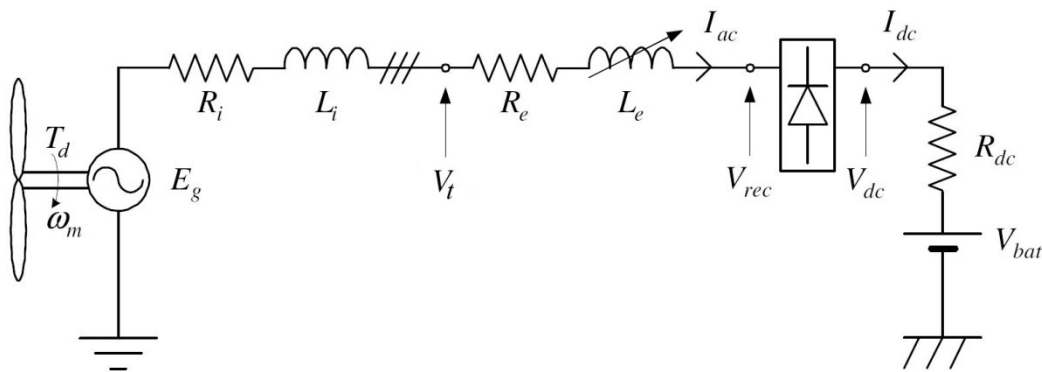
Fig. 26: Per phase equivalent circuit diagram of the wind generator system [24].

Firstly the dc-voltage of the battery bank can be replaced with its ac-equivalent voltage represented by the voltage source in Fig. 27. The fundamental RMS ac-equivalent phase voltage of a battery, V_b, is calculated by [24] as

$$V_b = \frac{\sqrt{2}\left(V_{bat} + 2V_d\right)}{\pi},$$

(55)

where V_d is the forward voltage drop over a diode in the rectifier. The frequency of the new equivalent ac-voltage, V_b, is the same as the operating frequency of the generator, f_g [24]. V_b is also known as the battery bank's base voltage. Once the generator back-EMF increases to above this voltage the battery bank will start charging. The base voltage is defined later. Secondly, the internal resistance of the battery can be converted to its ac-equivalent as [24]

$$R_{ac} = \frac{6R_{dc}}{\pi^2}.$$

(56)

From the equivalent circuit model of Fig. 27, a phasor diagram can be drawn which will aid in the system analysis. The diagram is shown in Fig. 28; the phasors are not to scale. Since the value of R_e is relatively small, it is omitted from the phasor diagram for simplification purposes.
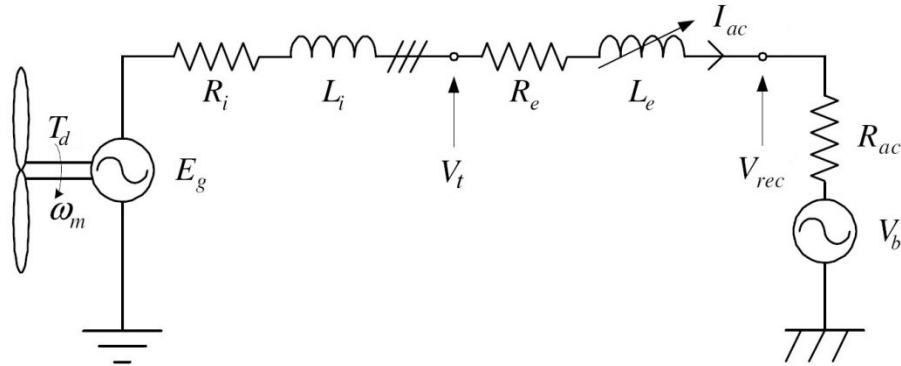
Fig. 27: Per phase ac-equivalent circuit diagram of the RFPM wind generator system [24].
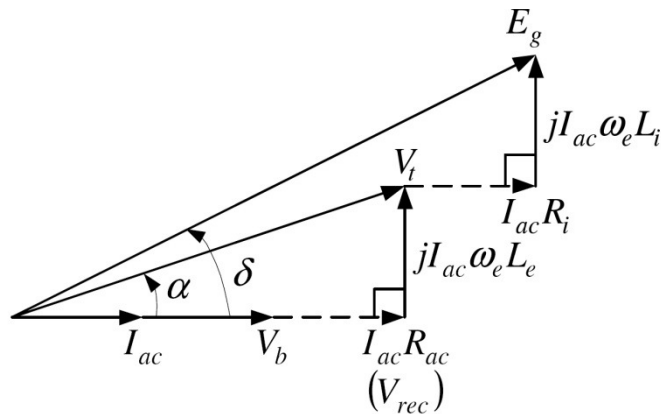
Fig. 28: Phasor diagram of the wind generator system [24].
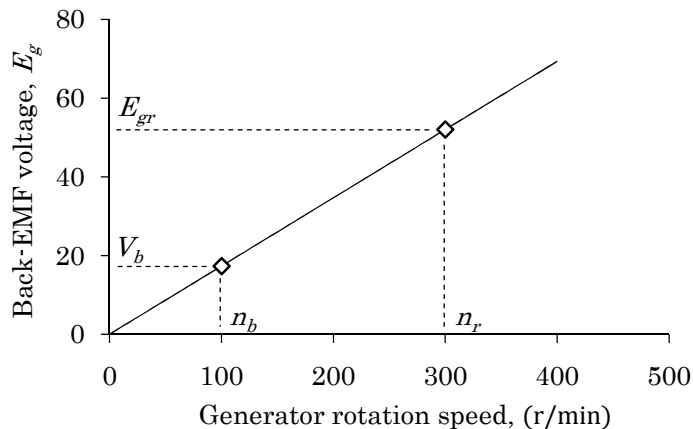
Fig. 29: Back-EMF voltage versus rotation speed of the RFPM wind generator.

The phasor diagram shows that the phase current, I_{ac}, is in phase with the rectifier voltage, but lags in relation to the generator back-EMF, E_g. This lagging is largely due to the role of the external inductance and also to a lesser extent to the relatively small internal machine inductance. The angle, δ, between the phase current and back-EMF voltage is referred to as the wind generator system's current angle.

Fig. 29 shows how the battery bank's base voltage, V_b, lies at the base rotation speed, n_b. If the generator back-EMF is lower than the dc-voltage of the battery bank, V_b creates a reverse bias over the diode rectifier which prohibits the batteries from discharging through the generator. At speeds higher than n_b the generator will generate high enough back-EMF voltage to overcome the reverse bias on the diodes and start charging the battery bank [46]. The rated back-EMF voltage, E_{gr}, occurs at the rated speed of n_r.

2.5.2 Power point matching

To obtain better power point matching of the RFPM wind generator system the appropriate value of the external inductance, L_e, should be determined. If a correct size of inductance is inserted into the system, the power curve of the generator and the power curve of the wind turbine blades can be matched and the system's performance at high and low wind speeds can be improved [15], [24]. The wind turbine power curves of Fig. 7 are redrawn in Fig. 30, with an additional maximum power point curve superimposed on it as shown. These points on the curve show the optimal power which can be extracted at different wind speeds using the available 1.9 m turbine blades.

From the previous section it can also be seen that the generator cut-in speed is determined by the ac-equivalent battery voltage, V_b. In other words, the frequency at which the generator starts delivering power to the battery bank is determined by V_b. If the battery voltage is lowered the

generator back-EMF reaches the voltage required to overcome the imposed rectifier diode's reverse bias at a lower speed (and vice versa).

A simplified maximum power point plot of the wind generator power curve is shown in Fig. 31. Two points are shown on this graph. The first point, denoted by b, is the generator's cut-in point at the corresponding cut-in speed of n_b. The second point, r, is the generator's rated operating point at the corresponding rated speed of n_r.

If good wind turbine power matching is to be obtained a specific value of L_e should be calculated that will guide the generator's power plot through points, a and b. The external inductance is situated in series with the internal inductance as shown in the ac-equivalent circuit of Fig. 27. This is also true for the resistance values of the per-phase circuit. The total system inductance, L_s, and system resistance, R_s, can be calculated as

$$L_s = L_i + L_e + L_c \tag{57}$$

and

$$R_s = R_i + R_e + R_c + R_{ac}, \tag{58}$$

where L_c and R_c are the per-phase inductance and resistance inherent in the connecting cable. The values of L_c and R_c are usually very small, enough so that they can be ignored for the purpose of this study. Since the external inductor has some resistance of its own, R_e is inserted into (58) to account for this. Knowing this, a more simplified per-phase system can be drawn as shown in Fig. 32 with its corresponding phasor diagram shown in Fig. 33.
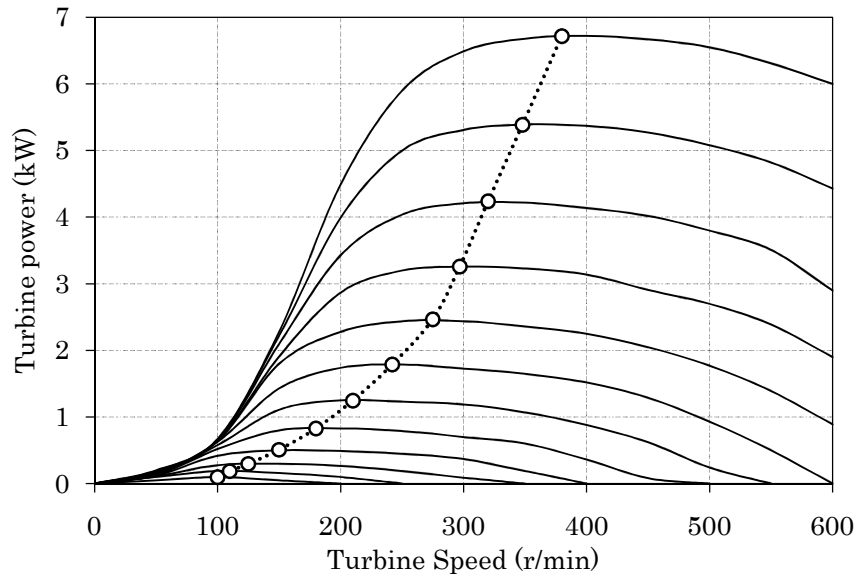
Fig. 30: Peak power points on the wind turbine blade curves.
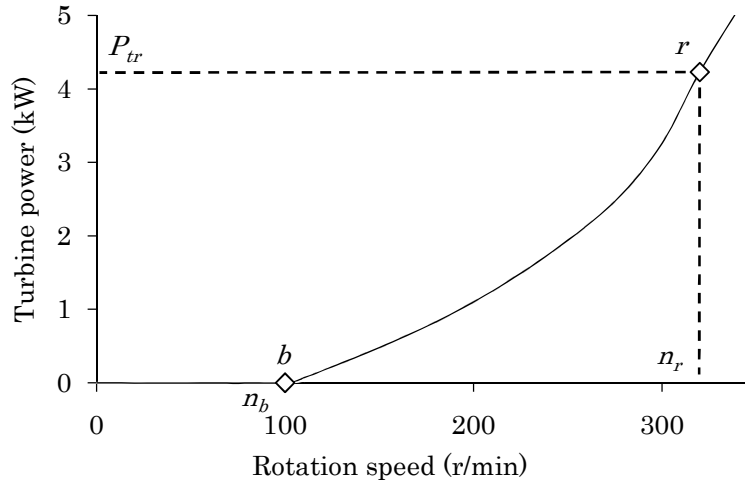
Fig. 31: Power points at cut-in speed (n_b) and rated speed (n_r).
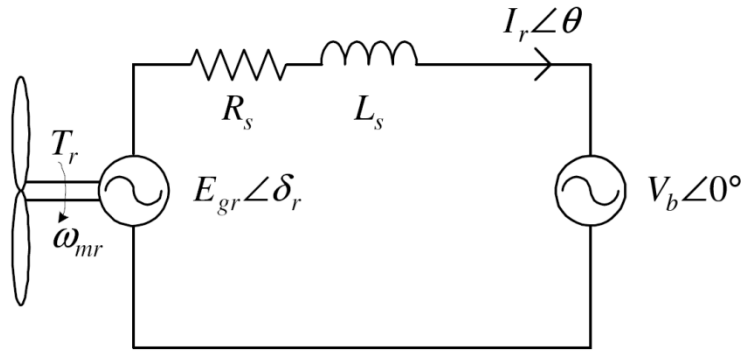
Fig. 32: Simplified equivalent circuit with total system inductance and resistance shown.
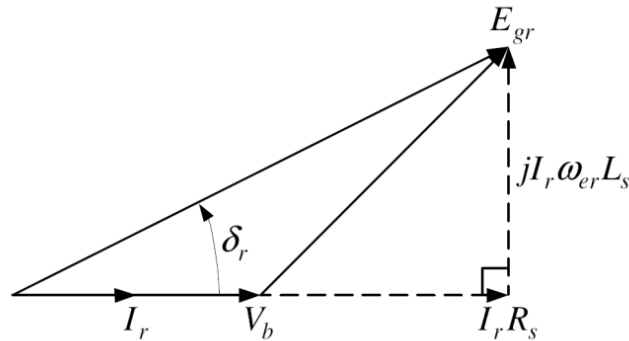
Fig. 33: Phasor diagram of the simplified system.

During rated operation in the above conditions the line current, I_{ac}, of the system is equal to the rated current, I_r. Also, the generator's rated output back-EMF voltage, E_{gr}, is a function of the rated and cut-in speed of the generator and can be expressed as

$$E_{gr} = V_b \frac{n_r}{n_b}. \tag{59}$$

The rated torque, T_{dr}, of the wind generator which will be developed at the operating point denoted by r in Fig. 31, can be calculated by

$$T_{dr} = \frac{P_{tr}}{\omega_{mr}},$$

(60)

where ω_{mr} is the rated mechanical rotation speed in radians per second and P_{tr} is the rated turbine power. From Fig. 31, ω_{mr} can be expressed as

$$\omega_{mr} = \frac{\pi n_r}{30},$$

(61)

while

$$\omega_{er} = \frac{p \omega_{mr}}{2}.$$

(62)

Since the wind and friction losses can be ignored at such a low rated speed the rated turbine power, P_{tr}, can be calculated as

$$P_{tr} = 3 E_{gr} I_r \cos \delta_r,$$

(63)

where δ_r is the current angle at rated speed that can be calculated from Fig. 33 as

$$\cos \delta_r = \frac{V_b + I_r R_s}{E_{gr}}.$$

(64)

From equations (63) and (64) the rated current, I_r, can be calculated as

$$P_{tr} = R_s I_r^2 + V_b I_r$$
$$\therefore I_r = \frac{\sqrt{V_b^2 + \frac{4}{3} R_s P_{tr}} - V_b}{2 R_s}.$$

(65)

From (57), (59), (61) and (62) the external inductance value can be calculated by

$$L_e = \left(\frac{60 V_b}{\pi p n_b} \right) \frac{\sin \delta_r}{I_r} - L_i.$$

(66)

With this external inductor inserted into the wind turbine system the generator power curve will pass through the operating points, b and r, on the turbine power curve [24].

Another important aspect to take into account is the power generated at speeds above the rated speed. At high wind speeds the generator needs protection from damage. One of the most important features that need to be protected against is the generation of currents beyond the design limit. Another positive effect of using an external inductance is the fact that the impedance of the inductor increases with increasing frequency. This means that at higher wind speeds the peak generated power is restricted by the increasing impedance of the external inductor. A rather low designed

current density of $J = 5$ A/mm² also allows for some protection. This current density could double for short intervals without damaging the generator.

2.5.3 System operation under rated conditions

In this section the system is analysed under its rated operating condition. Fig. 34 shows the equivalent circuit of the wind generator system with power shown at different points in the system. The dc-current charging the battery bank is calculated as [24]

$$I_{dc} = \frac{3\sqrt{2}}{\pi} I_r ,$$

(67)

where I_r is given in (65). The dc-bus voltage, V_{dc}, of the battery bank present on the dc-side of the diode rectifier is given as

$$V_{dc} = V_{bat} + I_{dc} R_{dc} ,$$

(68)

where V_{bat} is the open circuit dc-voltage measured over the battery terminals and R_{dc} is the internal resistance of the batteries. The efficiency of the wind generator system, from turbine power, P_{tr}, to power delivered to the batteries, P_{dc}, can be calculated by

$$\eta_{sys} = \frac{P_{dc}}{P_{tr}} \text{ x } 100\% ,$$

(69)

with

$$P_{dc} = I_{dc} \left(I_{dc} R_{dc} + V_{bat} \right) .$$

(70)

Some power is also dissipated in the diode rectifier. This can be calculated by

$$P_d = 2V_d I_{dc} ,$$

(71)

where V_d is the forward conducting voltage across a diode in the rectifier. The power at the rectifier, P_{rr}, is calculated as

$$P_{rr} = P_d + P_{dc}$$

(72)

or

$$P_{rr} = 3V_{rr} I_r \quad (\text{with } \delta_r \approx 0°) .$$

(73)

By using (67), (68) and (71) – (73) the rated fundamental RMS phase voltage at the ac-terminal of the rectifier can be calculated as

$$V_{rr} = \frac{\sqrt{2}}{\pi} \left(V_{dc} + 2V_d \right) .$$

(74)

As can be seen in Fig. 32 and (55), V_{rr} and V_b is the same value. The efficiency of the RFPM wind generator under rated conditions, η_{gr}, can be calculated by

$$\eta_{gr} = \frac{P_{gr}}{P_{tr}} \text{ x } 100\% \,, \tag{75}$$

where P_{tr} can be calculated by (63), and the rated wind generator output power, P_{gr}, by

$$P_{gr} = 3V_{gr}I_r \cos\alpha_r \,. \tag{76}$$
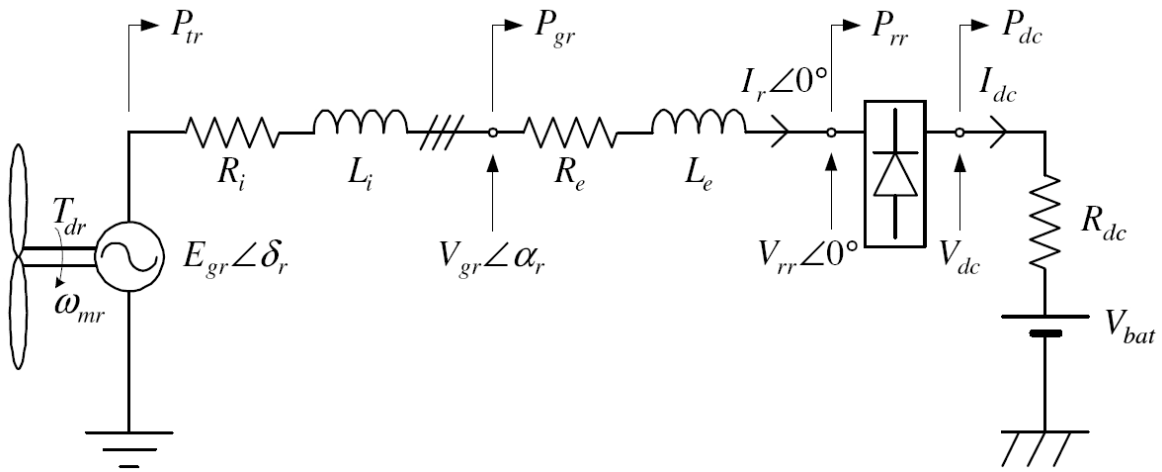
Fig. 34: Equivalent circuit of the wind generator system with generated power shown at different points.

Chapter 3
Mechanical Design of the RFPM Generator

The interaction of forces from the external environment, partly those due to the wind and the movements of the various wind generator components, result not only in the desired energy production from the turbine, but also in stresses in the constituent materials. When designing a wind turbine, these stresses are of primary concern, because they directly affect the life, strength and reliability of the machine. The turbine must not only be effective in extracting energy but also structurally sound enough to withstand the loads it will experience while doing so.

When considering the mechanical side of the design of a wind turbine generator, there are various aspects to consider. The mechanical design of large wind turbines presents a giant task to engineers. With regard to small to medium turbines, the mechanical design is less extensive. In this chapter various parts of the small-scale wind generator will be dealt with from a mechanical strength perspective. Parts are optimised to be cheaper and lighter by looking at their inherent strength. Statics, dynamics and strength of materials are the fundamentals to be looked at. In this particular design there are four major load carrying components that are prone to failure. These are the shaft, the rotor yokes, the stator and the assembly fasteners. All will be considered in this Chapter.

3.1   Shaft

In larger wind turbines the main shaft transmits the rotational energy from the rotor blades to a gearbox. Essentially, the shaft is used to transmit loads to the nacelle which is stationary. The loads include the aerodynamic loads, gravitational loads and the reactions of the gear and bearings. In some smaller wind turbines the shaft is stationary and its main purpose is only to support the generator and not to transmit rotational loads. This is also the case for the prototype built during this study. This kind of shaft topology mainly experiences static or non-time varying loads. A schematic cross-section of the shaft assembly is depicted in Fig. 35 and the dominant static loads are

shown. The vertical plane on the left-hand side of the figure is fixed to the nacelle while the bearings rest on the horizontal plane to the right.

3.1.1 Shaft deflection

The deflection of the shaft is the only major design consideration on this part. It is characterised by the sagging or bending of the part under load. The whole mass of the generator rests on the shaft. It is important that the shaft does not fail under either the weight of the generator itself or the external forces the wind places on the generator. Deflection also denotes an elastic bending of the part. As opposed to plastic deformation, elastic bending is a non-permanent deformation. The member will return to its original shape once the loads are removed [41]. Plastic deformation is not desirable since it causes the part to yield and thus deform permanently.
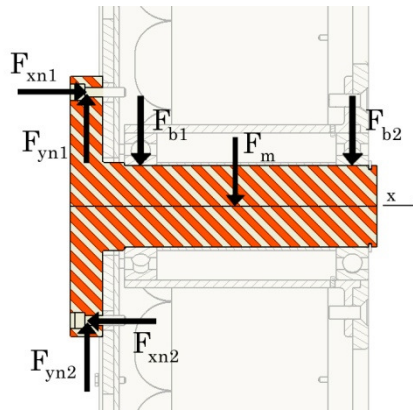

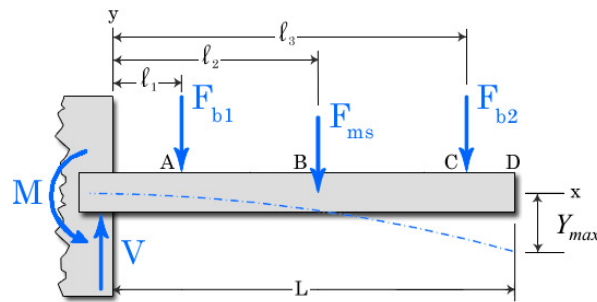Fig. 35: Design loads on generator shaft.

Fig. 36: Deflection of the shaft under load.
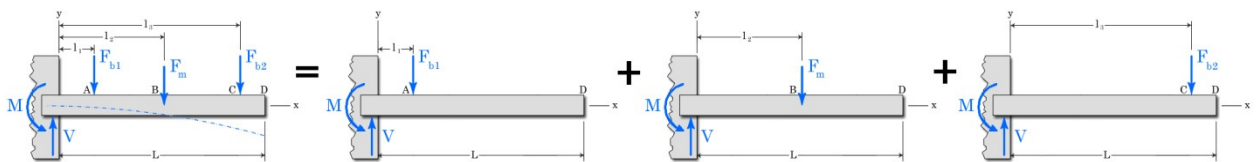
Fig. 37: Superposition of shaft loads.

Since the one end of the shaft is fixed onto the nacelle, the system can be approximated as a cantilever beam with forces as shown in Fig. 36. Once the loads on the shaft are known the deflection can be calculated by cantilever deflection theory. Cantilever deflection can be solved by linear differential equations, since the deflection function $v(x)$ and its derivatives apply linearly. For this reason the slope and deflection of a beam that simultaneously supports multiple different loads can be obtained by the linear superposition method [41]. Superposition is used to add the individual effects of loads acting separately of each other. This is shown schematically in Fig. 37.

From Fig. 37 the maximum deflection of the shaft tip, Y_{max}, at length L, can be calculated. There are three forces present on the shaft. F_{b1} and F_{b2} are the forces transferred by the bearings that support the weight of the generator and F_{ms} is force due to the gravitational pull on the mass of the shaft itself. The superposition equation for Fig. 37 can be written as

$$\Upsilon_D = \Upsilon_{max} \equiv \left| v(L) \right| = \Upsilon_A + \Upsilon_B + \Upsilon_C = \left| v_A(L) \right| + \left| v_B(L) \right| + \left| v_C(L) \right|, \tag{77}$$

where Y_{max} is the maximum deflection occurring at the shaft's end or point D in Fig. 36. Y_A, Y_B and Y_C are the individual deflections of point D caused by the forces at A, B and C respectively. The individual deflections are given in [41] as

$$\Upsilon_i = \frac{F_j \left(\ell_k \right)^2}{6EI_0} \left(3L - \ell_k \right), \tag{78}$$

where respectively

$$i = A, B, C$$
$$j = b1, ms, b2$$
$$k = 1, 2, 3$$

In (78) E is the Young modulus, or modulus of elasticity, of mild steel and I_0 is the area moment of inertia of the shaft. L and ℓ_k are given in Fig. 36. In Appendix D how to derive (78) is discussed. The area moment of inertia of a solid round shaft can be calculated from [42] as

$$I_0 = \frac{\pi d_s^4}{64}, \tag{79}$$

where d_s is the shaft diameter. Substituting (78) into (77) gives the maximum deflection occurring at D as

$$\Upsilon_{max} = \sum_{i=A,B,C} \Upsilon_i = \frac{1}{6EI_0} \left(F_{b1} \ell_1^2 \left(3L - \ell_1 \right) + F_{ms} \ell_2^2 \left(3L - \ell_2 \right) + F_{b2} \ell_3^2 \left(3L - \ell_3 \right) \right). \tag{80}$$

With a length of $L = 170$ mm and a solid shaft diameter of $d_s = 50$ mm the shaft deflection is a mere 0.43 µm. This value is within the acceptable range. In this study a solid shaft was used. This could be optimised in terms of mass by making the shaft hollow. A correctly designed hollow shaft could easily handle the forces of such a light generator.

Cantilever deflection theory can also be used in other parts of the turbine design. The bending of the turbine blades under the uniformly distributed wind forces is a good example.

3.2   Rotor yokes

As mentioned previously the rotor of the RFPM generator is a double sided rotor. This type of rotor consists of two cylindrical steel yokes of different diameter located concentrically, one in the other. Both the inner and an outer yoke act as rotors, each having a set of equally spaced permanent magnets located on them. This permits a required flux density to be induced in the air-gap located between them. Steel yokes are used, amongst others, for their strength in securing the PM magnets and to act as flux conductors between neighbouring magnets, minimising leakage flux. Since the rotor has to be constructed of a magnetic material, mild steel in this case, the mass of the two yokes has a significant impact on the overall mass of the generator.

The optimum designed generator of Chapter 2 set fixed values to the active length, l_a, average turbine stator diameter, d, and the rotor yoke wall thickness, h_y. The turbine blade design prohibits any change in the diameter of the outer yoke and is thus a fixed value. The active length also fixes the minimum limit of length that the rotor yoke can be. Lastly, the yoke wall thickness is limited to a minimum value of 8 mm according to the analytical calculation of section 2.3.3 and the FE analysis of section 2.4.3.

What remains is to determine whether the mechanical strength of an 8 mm yoke is sufficient to withstand the large attraction forces produced by the permanent magnets. The yoke thicknesses can now be optimised in terms of mechanical strength. This is why the yoke thickness of the rotors is an important additional dimension to be optimised when minimising the mass.

3.2.1 Thin-walled pressure vessel design

One drawback of this type of machine, and this is particularly prevalent in axial flux machines, is the large attraction forces that exist between the rotor cylinders due to the permanent magnets. Each magnet located on the inner yoke attracts a magnet of the opposite pole on the outer rotor yoke. If both rotor yokes have 32 high grade N48 NdFeB magnets located around their circumference, the total summed attraction forces between the rotors are quite high. The magnitude of the force between two magnet pairs of the same size but opposite polarity, F_m, can be calculated by Maxwell's pulling force calculation [43] as

$$F_m = \frac{B_g^2}{2\mu_0} A_g \,, \tag{81}$$

where B_g is the average air-gap flux density between the magnets, μ_0 is the permeability of air (a magnetic constant) and A_g is the cross-sectional area of the facing magnet sides. In this equation it is assumed that both of the magnets are of equal size, their flux passes through air and there is little or no leakage flux present. Since the rotor diameters are so large, the inner magnet's cross-sectional areas are a mere 5 % smaller than the outer magnet's diameters. This allows the first condition to be met with good results. The second condition is also met since the machine is an air-cored one. Thirdly, the magnets are attached to steel yokes which provide a very good flux return path, effectively eliminating most of the fringing flux.

Mechanical strength analysis is done on the steel rotor yokes in order to decrease their mass. In axial flux machines the rotor discs are pancake-shaped, whereas in radial flux machines they have a cylindrical from. These axial-flux rotor yokes are prone to bending under the magnet attraction forces [43]. If the same thickness of back yoke is used in both axial- and radial-flux machine rotors, the axial-flux would experience considerably more bending than their radial flux counterparts. This is due to the inherent strength of the radial flux rotors' cylinder topology.

Because of the inherent strength of the cylindrical topology the radial-flux machine's rotors can be designed much lighter than an axial-flux machine's flat rotors. The equally spaced permanent magnets fastened around the circumference of the rotor create an almost uniform stress distribution in the yoke as seen in Fig. 38. These evenly distributed forces can be compared to an internal pressure in a cylinder calculated as [42]

$$P_a = \frac{F}{A}, \tag{82}$$

where P_a is the resultant pressure of a force F, acting over a area of A. Because of this internal pressure and the cylindrical form of the rotor, the part corresponds very well to a pressure vessel with uncapped ends [41], [42].

To determine whether thin-walled pressure vessel theory is appropriate for use on these particular rotor dimensions, one condition should first be justified. This condition states that the ratio between the yoke thickness and average rotor radius should be [41]

$$\frac{h_y}{r_{iy}} \leq \frac{1}{20}, \tag{83}$$

where h_y is the yoke thickness in the radial direction and r_{iy} is the inner yoke radius as seen in Fig. 39. This condition is met in this design and thin-walled theory is thus permissible.
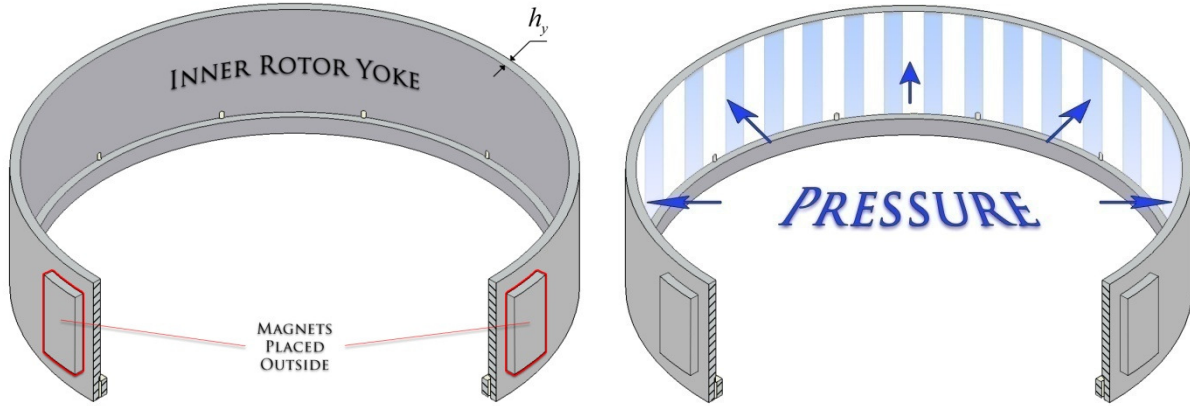
Fig. 38: Rotor yoke compared to a pressure vessel.
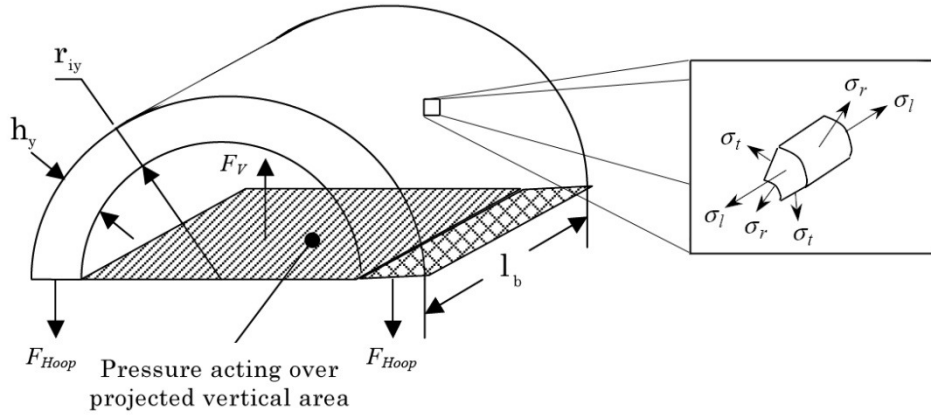
Fig. 39: Pressure vessel dimensions and loads.

By using thin walled pressure vessel theory on the rotor, the minimum allowable yoke thickness can be calculated. According to [42] the hoop stress, σ_h, can be assumed to be uniform across the wall thickness and the radial stress is insignificant compared to the tangential stress, thus, $\sigma_r = 0$. The longitudinal stress, σ_l, is assumed to be uniformly distributed across the wall thickness and the cylinder has no capped ends.

The internal pressure exerts a vertical force, F_v, on the cylinder wall,

$$F_v = P_i A_{proj} = P_i \left(2 r_{iy} l_b \right),$$

(84)

where P_i is the internal pressure inside the cylinder, A_{proj} is the projected area and r_{iy} and l_b are as shown in the Fig. 39. The tangential hoop force, F_{Hoop}, can be calculated by

$$F_{Hoop} = \sigma_t A_{stressed} = \sigma_t \left(h_y \, l_b \right),$$

(85)

where $A_{stressed}$ is the area of the yoke under stress. The vertical force is balanced by the tangential hoop stress, F_{Hoop}, so that

$$\Sigma F_y = 0 = F_v - 2F_{Hoop} = P_i \left(2r_{iy} l_b\right) - 2\sigma_t \left(h_y \, l_b\right). \tag{86}$$

Solving for the tangential stress gives

$$\sigma_t = \frac{P_i r_{iy}}{h_y}. \tag{87}$$

A Von Mises creation now gives the minimum thickness needed to withstand these stresses

$$h_y = S_f \left(\sqrt{\frac{3}{4}}\right)\left(\frac{P_i r_{iy}}{\sigma_Y}\right) = S_f \left(\sqrt{\frac{3}{4}}\right)\left(\frac{\left(F/A_y\right)r_{iy}}{\sigma_Y}\right), \tag{88}$$

where F is the total force acting on the yoke, A_y is the yoke area on which the force acts and σ_Y is the yield stress of the yoke material (which in this case is that of mild steel, σ_{fe}). With a safety factor, S_f, of five and mild steel used in construction, the minimum wall thickness needed to withstand these forces without plastic deformation of the yoke is found to be 1 mm. It should be noted that (88) does not take into account the deflection of the yoke tips under load but rather protects against yielding or plastic deformation which could ultimately lead to fracture. Tip deflection can still occur beneath the yield point of mild steel due to this lying in the elastic deformation range of the material. The deflection analysis of the yoke tips becomes an important consideration since this will determine whether the yoke can maintain the required air-gap between the two rotor yokes. In other words, both rotor yoke thicknesses need to be sufficiently thick to withstand the magnet attraction forces without causing deflection that will violate the air-gap. This condition will be investigated later in this Chapter by FE analysis.

3.3   Stator design and manufacturing

In Chapter 3 the stator armature windings of the RFPM air-cored generator is optimally designed from an electrical point of view. In this section the stator's mechanical design is discussed.

3.3.1 Armature coils

From the previous electrical optimisation the armature coils acquired fixed dimensions. Each coil is made up of individually insulated copper wires that are stranded together and wound in a particular manner. The round annealed copper wire has a pure copper core and is covered with a double layer of polyamide coating to insulate the wire. Armature coils are manufactured by using a winding machine and a coil former.

Fig. 40: A single stator coil in the former (left) and a completed coil (right).

The coils are wound around the former and are tied in place with winding twine string, prior to removal. Once a coil is removed from the former it is tested electrically to determine the existence of potential damage that can cause a short circuit. The completed coil is now ready for the mould. The coil former and a completed coil are shown in Fig. 40.

3.3.2 Mould design

To produce the new modular stator design mentioned in Chapter 3, a mould is needed to construct the individual stator sections. Since the stator pieces of a radial-flux generator are semi-circular the mould also needs to be designed in a similar fashion. To cut back on labour costs and produce a more cost-effective mould it was decided that the mould should be made from an assembly of smaller laser-cut mild steel plates. The steel plates are stacked on top of each other to form a solid part. The mould consists of two sections; a back base section and a front cover section. The base and cover pieces can be assembled together to form the complete mould. A different pattern was used to manufacture the base and cover sections so that they have a snug fit when placed on each other and when the mould is closed for casting. Threaded steel rods are inserted through holes in both of the sections to pull together the plates and form a single rigid form. Fig. 41 is an illustration of the two separated mould pieces prior to casting and after casting preparation.
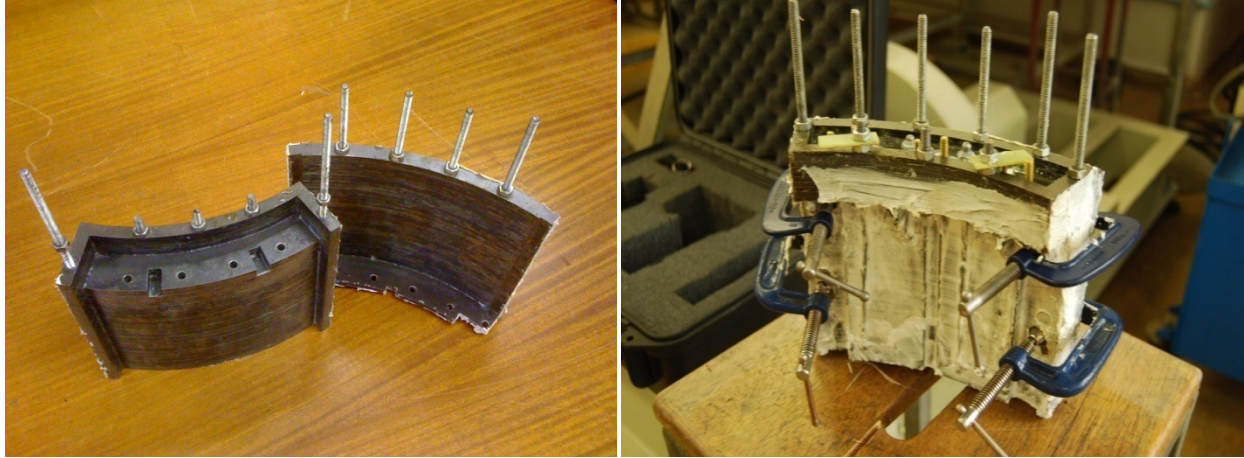
Fig. 41: Mould pieces apart (left) and the assembled and sealed mould (right).

An important consideration of the mould design is the mould material's thermal expansion properties. The epoxy resin stator pieces have to undergo a complete curing cycle in a heated oven before each casting can be removed. Obviously the mould will also be subjected to the same temperatures. Once the mould is assembled any swelling or elongation of its material could cause undesirable morphing of the epoxy resin and an incorrect casting. The dimensions of a casting should remain within certain prescribed tolerances or otherwise there is a risk of interference in the air-gap.

The dependence of size on temperature variation is measured in terms of the basic quantity known as the coefficient of linear thermal expansion [42]. The coefficient of linear thermal expansion, denoted by ψ, of a particular material is the constant that determines the amount of expansion the material will undergo if it is heated to a particular temperature. The calculation used to determine the expansion is given by [42] as

$$L_T = \psi L_0 \left(T - T_0 \right),$$
(89)

where L_T is the material's linear expansion in metres, L_0 is the initial length or thickness of the material and T and T_0 are the final and initial member temperatures respectively. This can also be expressed as thermal strain

$$\varepsilon_T = \frac{L_T}{L_0} = \psi(T - T_0),$$
(90)

where ε_T is the change in length per unit length for unit increase in temperature; that is thermal strain. To ensure that the deformation of the mould stays within respectable tolerances, the design has to incorporate the allowable strain tolerance before the final cutting form can be specified.

3.3.3 Epoxy resin castings

The epoxy resin stator castings are produced by first preparing the mould for casting. Initially the interior of the mould is smeared with a silicone based grease to ensure that the castings will not stick to the mould. This helps for easy release when the section is removed. Next the mould interior is lined with double woven fibreglass cloth. The cloth is placed on top of the grease and helps to increase the stator section's strength and ensure a more rigid end product. After this the three wound coils are placed side by side on the top of the base piece and aligned properly. Special care should be taken when positioning the coils. A minor variation between stator pieces can cause electrical characteristics to change considerably. If for instance the coils in this type of generator are misaligned by a single mechanical degree the corresponding electrical misalignment will be multiplied by a factor p/2 of that. The coils are then connected to the outgoing electrical links and some spacers are inserted. Following this the mould cover piece is placed on top of the base piece and is secured with G-clamps. Silicone rubber is now used to seal the outside of the mould and to close any remaining holes. The mould needs to be water tight because of the water-like viscosity of the epoxy resin that leaks even through the smallest opening.

While the silicone hardens, the epoxy resin mixture is prepared. This is done by adding the correct volumes of epoxy and their corresponding hardener into a container and thoroughly mixing the liquid. The liquid mixture is slowly cast into the mould to allow air to escape. A vacuum chamber is used to extract air bubbles suspended within the liquid. Once the desired level is reached the casting is allowed to cure. Curing consists of two stages. Initial curing takes place at room temperature where after secondary curing takes place in a high temperature oven. Finally the finished section is removed from the mould and is tested for quality. Fig. 42 (right) shows a finished peace.
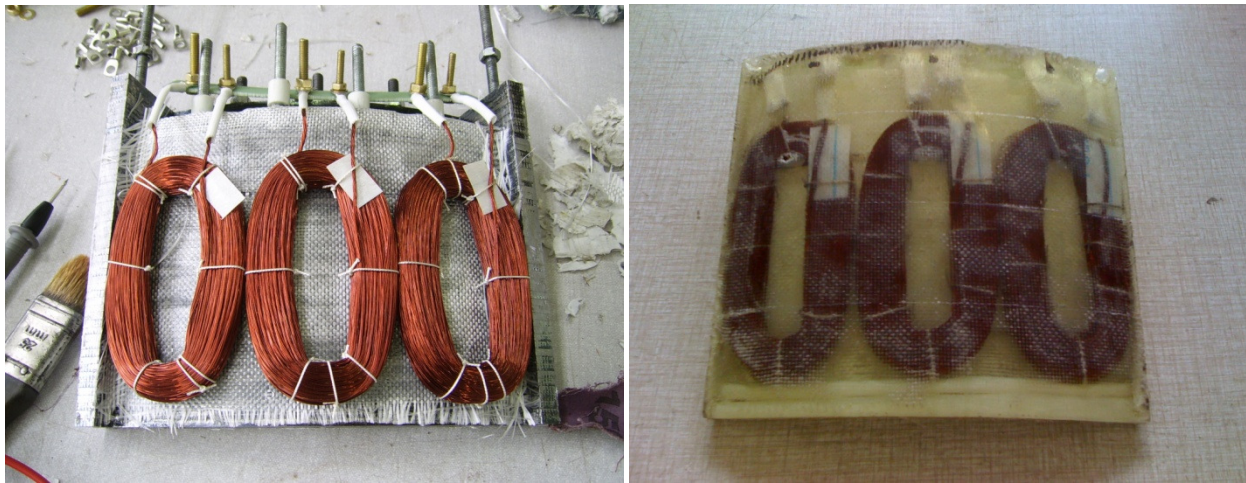

Fig. 42: Armature coils in mould prior to casting (left) and the finished stator piece (right).

3.4 Fasteners

In this section the fasteners fixing the assembly parts together are examined. The primary non-permanent fastener used when fixing metals to each other, is the bolted connection. This type of connection is examined first. Next, the permanent magnets situated on the rotor are secured in place with a permanent fastener, glue. Finally, the epoxy resin can also be seen as a permanent fastener and is examined last.

3.4.1 Bolted connections

The most widely used connection in wind turbine generator assembly is the bolted connection. It is also a very reliable connection because of all the academic study it has received and the quality standards it has to adhere to. Bolts are used in various connections in the RFPM generator. Any wind turbine is prone to cyclic loads, vibration and torque which require that these connections be strong and reliable. Since this study is partly about how to design an easily assembled generator these connections needs to be optimised. Calculations are done on these bolts to determine their optimal design. For a more detailed discussion on the bolted connections refer to Appendix C.

3.4.2 PM securing glue

To keep the permanent magnets secured to the steel rotor yokes, a method to fix their position permanently is needed. Various methods exist to keep the magnets from moving. One option, particularly useful in high speed PM machines, is to bolt the magnet onto the yoke by making a counter sunk hole through the magnet and into the steel. Another method is to use metal-to-metal securing glue. In this case a permanent connection is established between the permanent magnet material and the steel rotor yoke. The glue is prepared and a thin layer is applied on the magnet-yoke interface. After a magnet is secured with a clamp, sufficient drying time is allowed before neighbouring magnets are placed.

3.4.3 Epoxy resin

The armature coils in the stator of an air-cored machine need to be kept in place by a non-magnetic material. Various methods have been developed to solve this problem. PVC bobbins [49], plastic and epoxy resin [13] have all been used with good results. Another factor to consider when choosing such a fixing material is the strength and ease of manufacture. In this design an epoxy resin was chosen because of the relative ease of manufacture and good insulation properties. The resin and hardener are mixed together in liquid form and then cast. The fluid's high viscosity allows

for good penetration between the small gaps of the copper coils. Further, the resin is absorbed in the fibreglass cloth inserted in the mould.

3.5   Finite element analysis

The operation method of the mechanical FE analysis is largely similar to that of the electro-magnetic FE analysis described in Chapter 3. The same basic principles apply and calculations are done on a finite number of nodes in the model mesh. The difference, however, is that here mechanical stress and strain calculations are performed on the model instead of electro-magnetic calculations. In this section FE analysis is used to verify the analytical results of the shaft and yoke deformation.

Shaft deflection

The shaft deflection is simulated using *MSC Patran™ 2005*. In this simulation the three concentrated load forces acting on the shaft are applied to the mild steel FE model. These are the two bearing forces denoted by, F_{b1} and F_{b2}, and the shaft mass, F_{ms}. Fig. 43 shows the shaft tip deflection caused by the loads. It was found that the analytical calculation results of the previous section are predicted quite accurately by the FE analysis.

Yoke deformation

As mentioned previously, rotor yoke deformation can still occur within the elastic range of mild steel and diminish the air-gap length. This could cause a smaller clearance between the permanent magnets and the stator and the potential that the two surfaces will make contact is higher. If these two surfaces scratch against each other damage will occur. This elastic type of deformation however, is reversible. Once the forces are no longer applied the object returns to its original shape. FE analysis is performed on the inner rotor yoke model to investigate this condition.

The magnet attraction forces present between each opposite rotor magnet should also be verified using FE analysis. According to (81) these forces are dependent on the average air-gap flux density, the permeability of air and the cross-sectional area between the two magnets. Electromagnetic FE analyses show a force of more or less the same magnitude to the analytically calculated result in (81). A uniform pressure, equivalent to the forces induced by the magnets per unit area of the affected yoke, is applied inside the FE model.

Fig. 44 represents the FE model of the mechanical strength simulation. The yoke wall thickness was found to be as low as 4 mm so as to allow an insignificant amount of yoke deformation. Very small deflection occurs at the ends: 0.06 mm. This means that according to the mechanical strength analysis of the rotor yokes the wall thickness, h_y, does not have to exceed the 4 mm mark.
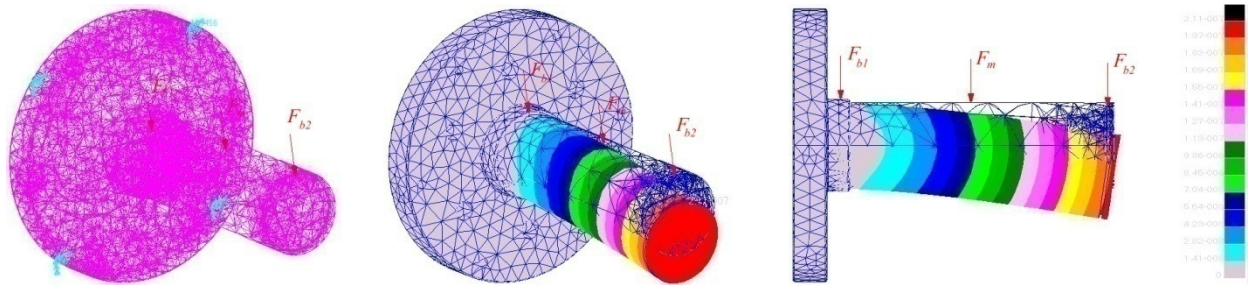
Fig. 43: FE simulation results of the shaft deformation and tip deflection under three point loads.
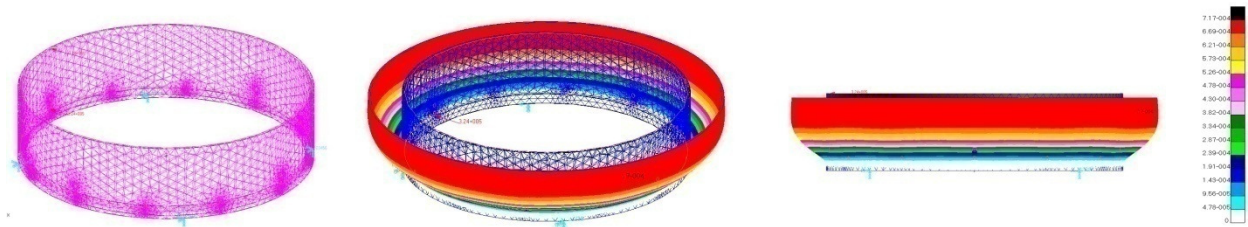
Fig. 44: FE simulation results of the yoke deformation under a pressure load.

In section 2.4.3, however, it is shown that the required rotor yoke thickness needed to ensure desirable flux saturation levels in the steel back yoke (according to the electromagnetic analysis) forces the yoke wall to be increased to 8 mm. This thickness is double the optimum 4 mm thickness from the mechanical strength analysis standpoint. It is implied by the result that mechanical considerations do not determine the optimum yoke wall thickness but rather the electromagnetic conditions. The yoke mass therefore is governed by the electromagnetic optimisation rather than the mechanical.

Chapter 4
Simulated and Measured Results

In this chapter the RFPM wind generator prototype and system are tested and the measured results are discussed. The analytical results of previous chapters are put to the test and verified with these measurements. All tests on the generator were performed at the University of Stellenbosch's Electric Machines Research Laboratory.

4.1   Test station setup

The test bench setup consists of the following:

- An *Allan Bradley* variable speed drive (VSD) controlled, 4-pole 55 kW induction motor. This motor is used to drive the RFPM generator at a desired speed and/or torque so as to simulate the interaction of the wind on the turbine blades.
- Two prop shafts make the connection between the induction motor and the RFPM generator. These shafts are responsible for the torque transfer and have the advantage of not needing precise alignment. Shaft losses are small and negligible.
- A *Lorenz* torque sensor calculating the turbine input power (P_t) by measuring the developed torque (T_d) and the mechanical shaft speed (ω_m). The measurement data is read via a USB 2.0 connection and stored on a laptop computer.
- A 3-phase external inductor (L_e) is coupled to the RFPM generator's terminals.
- A 3-phase 6-bridge diode rectifier is inserted in series with the external inductor (L_e). This rectifies the generator's 3-phase ac-current to single phase dc-current.
- Three series connected 12 V *Deltec* deep cycle lead-acid batteries are connected to the dc-side of the rectifier. These simulate the battery bank load.
- Various other test and measurement equipment: oscilloscopes, circuit-breakers and resistors.
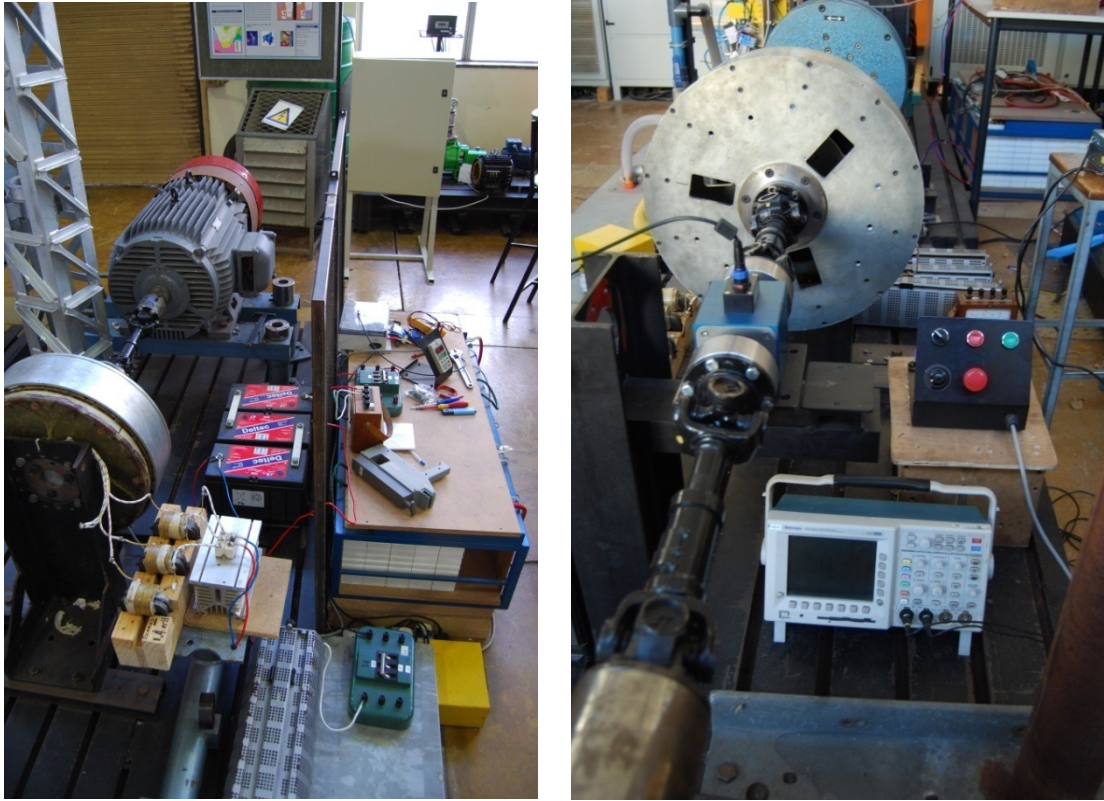
Fig. 45: Test bench setup.

Table 3: Data of prototype air-cored generator.

$p = 32$; $Q = 24$	$a = 8$	$R_i = 52.5$ Ω	$h = 10$ mm
$\kappa = 0.37$	$N_p = 10$	$d = 464$ mm	$h_m = 8.2$ mm
$N_t = 96$	$d_c = 0.315$ mm	$l_a = 76$ mm	$h_y = 8$ mm

Generator prototype

A prototype of an air-cored stator RFPM wind generator has been built and tested. Some of the dimensions and machine factors of the prototype are not precisely the same as the optimum dimensions given in Table 2 (page 33). Fig. 45 shows the test bench setup with the RFPM generator prototype connected to the induction motor. Some of the data of the generator are given in Table 3; the other data are the same as in Table 1.

4.2 Generated power and efficiency

To measure the various performance parameters of the RFPM generator a chosen rated speed of 320 r/min was used. This rated speed is slightly higher than the initial chosen speed of 300 r/min. The reason for this is that the optimum power point of the turbine blades (according to Fig. 30) at a wind speed of 12 m/s is closer to 320 r/min. All generator optimisations, as explained in the previous

section, and all analytical calculations, thus, were redone at this speed to compare calculated with measured results.

4.2.1 Measuring the equivalent circuit parameters

In this section the equivalent circuit parameters of the air-cored generator are measured. Fig. 14 shows the simplified generator circuit. From this it can be seen that three parameters need to be determined. These are the internal per-phase resistance, R_i, the internal per-phase inductance, L_i, and the eddy current loss resistance.

Internal resistance, R_i

The per-phase resistance is measured using two tests. Firstly, a dc-voltage is applied over the terminals of a phase. The resultant dc-current in the stator windings is measured. From this Ohm's Law is used to calculate the resistance. The second test is done to verify the first; a milli-Ohm meter is connected successively across each of the phase's output and the neutral star point and the resistance of each phase is measured. The tests were performed at an ambient room temperature of 20 °C. The resistivity of copper at room temperature is $\zeta_{cu\text{-}20} = 17 \times 10^{-9}$ Ωm. The measured internal per-phase resistance is 48 mΩ. This closely correlates with the analytical calculation of (20).

Internal inductance, L_i

It is very difficult to measure the internal inductance of an air-cored generator accurately. This is primarily due to the very low inductance values of the coils [24]. There are, however, a couple of tests that can be performed. One of these tests is to do a open circuit (OC) test and a short circuit (SC) test. Both of these tests are performed at the same rotor rotation speed. The speed is determined by the safe level of operation of the SC test; the current generated by the SC test has to be within the specifications of what the copper windings can maintain without causing damage. Fig. 46 represents the equivalent circuits of the OC and SC tests.

The SC test is performed first at operating speeds of 20, 30 and 40 rpm. All three phase terminals are short circuited and the short circuit current, I_{sc}, is measured. The OC test is performed at the same rotation speeds to measure the generator's back-EMF voltage at that particular speed. In this case E_{oc} is equal to E_g since there is no current flowing and therefore no voltage drop across the generator's internal impedance. With the open- and short-circuit tests the per-phase internal impedance, Z_i, can be determined by

$$Z_i = \frac{E_{oc}}{\sqrt{3}I_{sc}}.$$

(91)

With Z_i known, the internal inductive reactance, X_{Li}, can be determined by

$$X_{Li} = \sqrt{Z_i^2 - R_i^2} \tag{92}$$

and this gives an internal inductance value, L_i, of

$$L_i = \frac{X_{Li}}{2\pi f}, \tag{93}$$

where the electrical frequency of the generator at the particular speeds is given by

$$f = \frac{n\,p}{120}. \tag{94}$$

Other tests which can be performed to calculate the internal inductance are standstill frequency tests, decay tests and load tests as described in, amongst others, [24]. The measured internal per-phase inductance is measured as 90 μH.

The rated back-EMF voltage, E_{gr}, can also be acquired by performing the OC test at rated speed. The OC terminal voltage waveform is very much sinusoidal and is shown in Fig. 47. It has a RMS value of 56 V at a rated speed of 320 r/min.
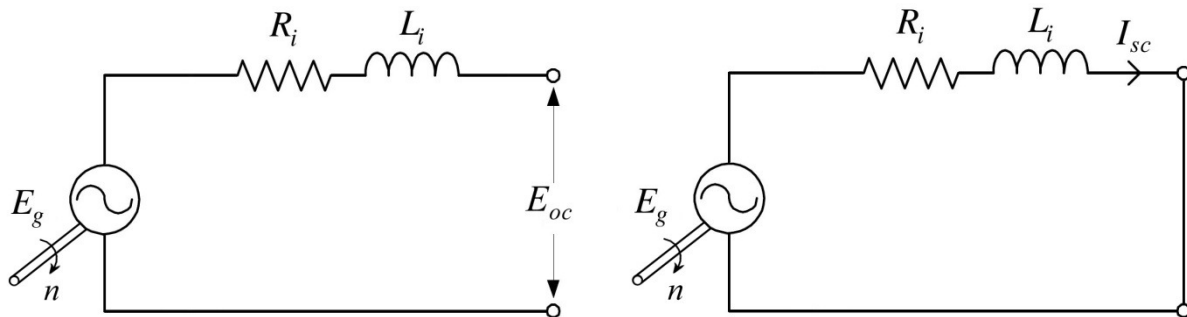
Fig. 46: Open circuit (left) and short circuit (right) tests.
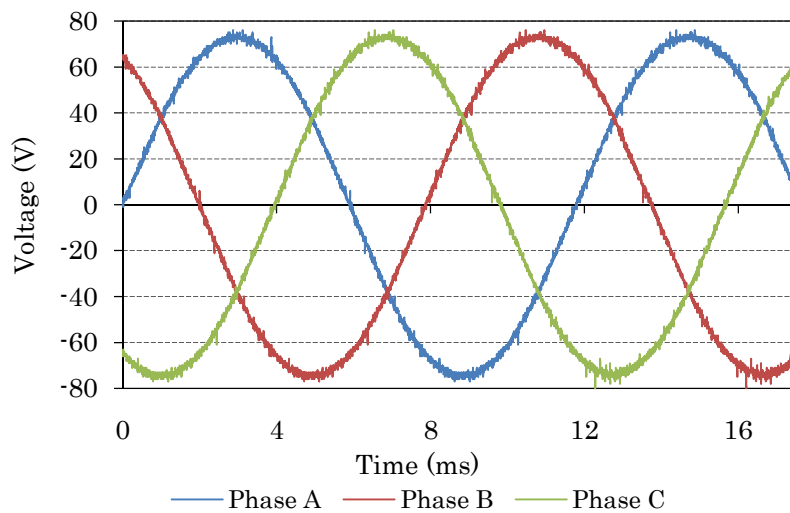
Fig. 47: The OC terminal voltage waveform at 320 r/min.

Eddy current resistor, R_{eddy}

The eddy current losses can be modelled as a resistor, R_{eddy}, which sits in parallel with the generator back-EMF. As seen in (28), the eddy losses are proportional to the square of the operating speed. This entails that the simulated eddy resistance remains constant with a change in operating speed. The eddy-resistance can thus be approximated by

$$R_{eddy} = \frac{3E_g^2}{P_{eddy}},$$
(95)

where E_g is the RMS value of the generated back-EMF voltage. Methods for measuring eddy losses are discussed in Appendix B. Calculated and measured results of the generated RMS open circuit terminal voltage and the eddy-current loss are given in Fig. 48.

4.2.2 Rectifier – resistor tests

In this section the generator was connected via an external inductance and diode rectifier to a resistive load in the form of a water-cooled resistor bank. Each of the bank's 12 ohm resistor elements are rated for 3 kW of load shedding. A combination of parallel connections ensures a workable load with a rated per-phase current of similar size as in the battery load test. In essence the load is matched to the generator.
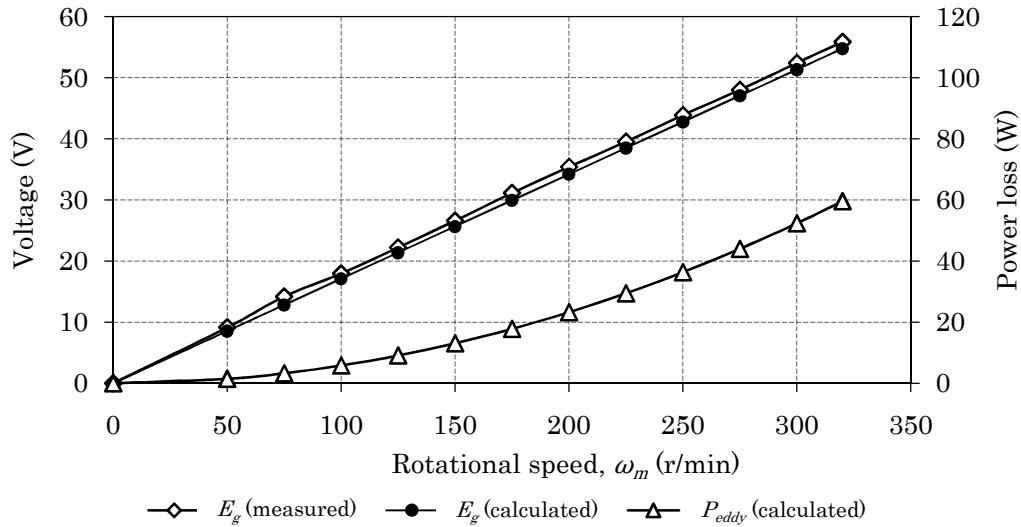
Fig. 48: Generated OC terminal voltage and eddy-current loss versus speed.

The per-phase terminal voltage measured on the ac-side of the diode rectifier, V_r, and the line current, I_r, are measured at the rated mechanical operating speed of 320 r/min and the results are shown in Fig. 49. In the figure it can be seen that the voltage is forced into a quasi-square wave

pattern with the well known six-pulse dc-ripple curves present on the plateau. This ripple is caused by the six-pulse diode rectifier present in the circuit [47]. Because of the presence of the external inductance, a close to sinusoidal line current is induced in the generator.

4.2.3 Rectifier – battery tests

Variable speed load tests are also conducted with the generator connected in a 36 V battery charging system similar to the one in Fig. 6a. The battery load is connected directly to the dc-side of the diode rectifier. The rated current and voltage waveforms at the diode bridge are shown in Fig. 50. It can be seen that the terminal voltage is again a square wave but with a flat topped plateau. The flat top is due to the presence of the battery bank which clamps the voltage. It can be seen that the generator current is fairly sinusoidal, which results in quiet generator operation. As in the rectifier-resistor test, the sinusoidal current can be attributed to the external inductance, L_e, inserted into the system.

4.2.4 Power generation and power point matching

The power delivery of the wind generator can be attained by measuring the power at various points in and at various speeds of the wind generator system. From this test it can be seen how well the RFPM air-cored generator matches the optimum power points of the turbine. The input power or turbine power, P_t, is measured by multiplying the torque sensor measurement on the drive shaft in front of the generator by the shaft speed. The output power or battery power, P_b, is measured at the battery terminals. The generator output power, P_g, is also measured between these two measurement points. The power measurement points of the wind generator system are shown in Fig. 51.

The power measurements are performed at different speeds to simulate each wind speed on the turbine blade power curves. The results of the input (P_t) and output (P_b) power tests are plotted on the turbine power curves and are shown in Fig. 52. From the plot it can be seen how the wind turbine follows both the designed base cut-in speed at 100 r/min and the rated power point at 320 r/min (12m/s wind speed).
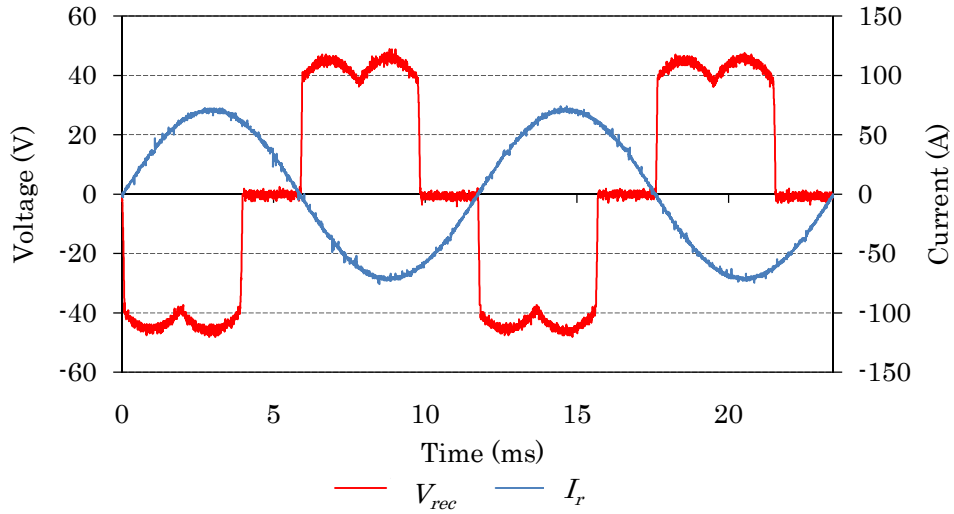
Fig. 49: Current and voltage waveforms of the diode rectifier with the generator connected to L_e and a resistance load at 320 r/min.
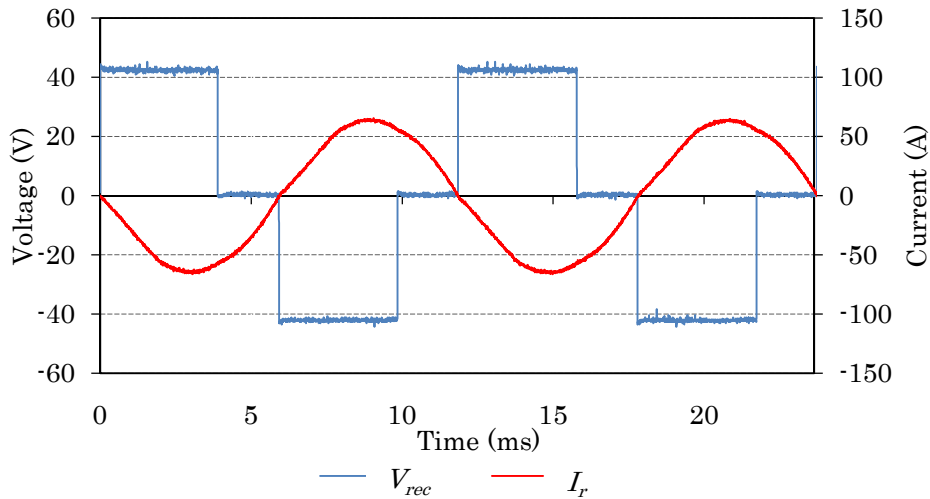
Fig. 50: Current and voltage waveforms of the diode rectifier with the generator connected to L_e and a battery charging load at 320 rpm.
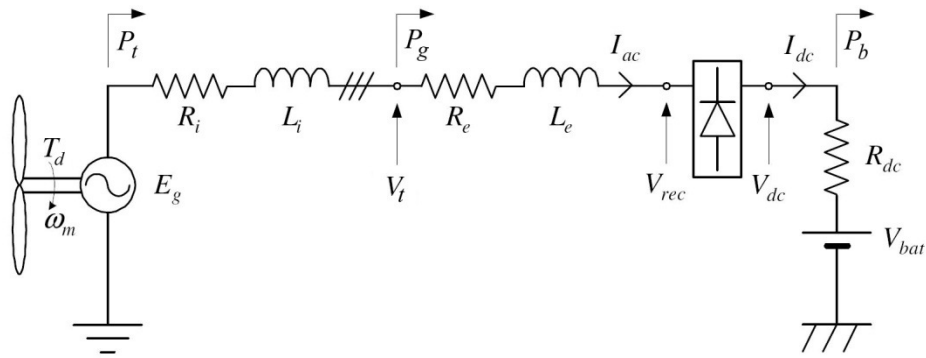
Fig. 51: Per-phase equivalent circuit of the wind generator system showing the power measuring points.
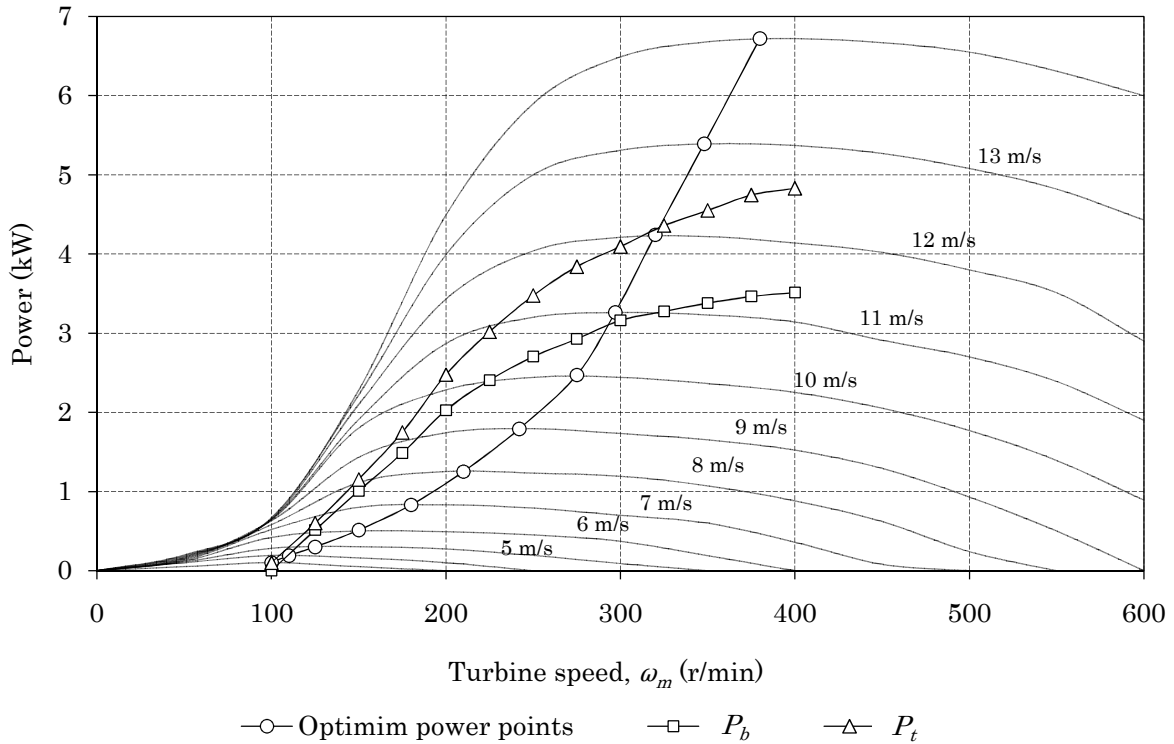
Fig. 52: Power measurement results at the turbine, P_t, and battery load, P_b versus the turbine speed.
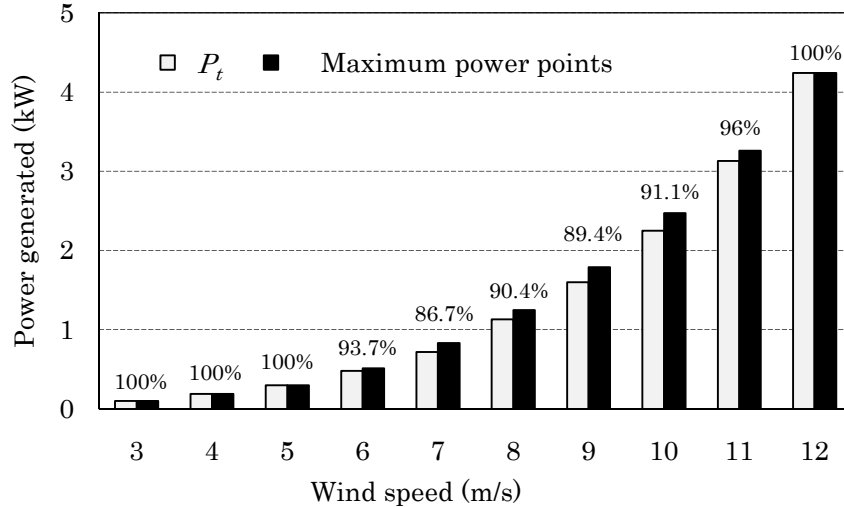
Fig. 53: Measured power point matching results compared to the turbine's optimum power points.

Power point matching

A major disadvantage of iron core machines is their non-optimal power matching. This is due to the fixed value of their system inductance, L_s. The fixed value of L_s is as a result of the iron-cored stator creating the high value of the internal inductance, L_i. Since the internal inductance is unchangeable once the generator is constructed the high value of L_i leaves little room for finer

adjustment of the value of L_s in order to obtain closer to optimal power point matching (PPM). In an air-cored generator however, the value of L_i is much lower making L_s very low as well. This means that the value of L_s can be accurately varied by the use of an external inductance, L_e. Because of this, PPM becomes partially controllable and is no longer fixed as in the case of the iron cored machine. By adjusting the value of L_e one can do good tracking at virtually any wind site.

From the plot in Fig. 52 a new comparison can be made to see how closely the air-cored turbine generator follows the turbine blade's optimum power points. Fig. 53 shows the comparison between the captured turbine power and the optimum power points on the turbine blade curves at different wind speeds. It can be seen that between the 3 and 12 m/s wind speeds the captured power is close to the optimum points. The worst power matching occurs at 7 m/s wind speed which gives 86.7 % of the optimum rating. Overall, thus, the power capturing is very good.

4.2.5 Generator and system efficiency

The RFPM wind generator efficiency, η_g, is defined as the ratio of input power, P_i, to the output power, P_o, of the generator. As seen in Fig. 51, in this case the generator efficiency becomes $P_i = P_t$ and $P_o = P_g$ to give

$$\eta_g = \frac{P_g}{P_t}. \tag{96}$$

The system efficiency is defined as

$$\eta_s = \frac{P_b}{P_t}. \tag{97}$$

Fig. 54 shows the measured system efficiency at various turbine speeds.

Fig. 54: Efficiency of the wind generator battery power system versus the turbine speed

Table 4 gives a summary of the measured and calculated values of both the battery load and resistive load systems. In general the calculated and measured results correlate well. Note specifically the increase in power and efficiency of the generator at small current angles; this implies that the air-cored RFPM generator must be rated as 4.2 kW with a battery charging load, but as 6.6 kW with an active controlled rectifier load.
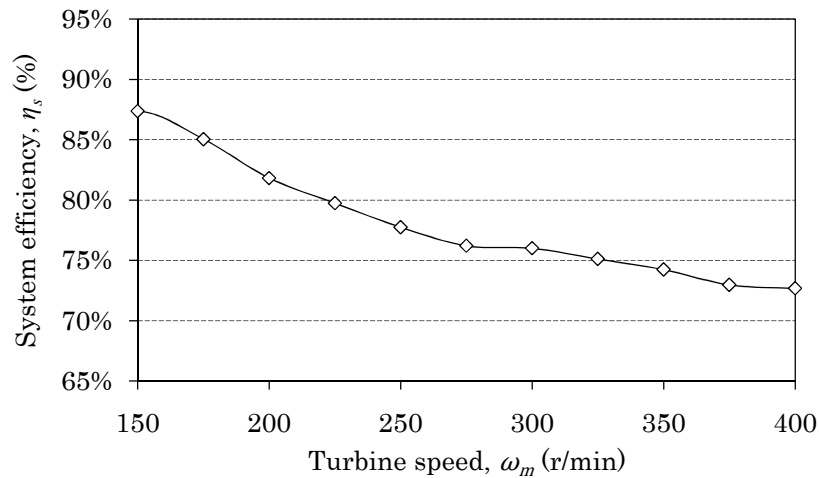
Table 4: Measured and calculated load results.

ω_r = 320 r/min ; f = 85.3 Hz ; I = 43.8 A ; J = 5.4 A/mm^2 ; $P_{wf} \approx 0$ W				
L_i = 90 µH	Battery charging load		3-phase resistive load	
R_i = 48 mΩ	L_e = 1.5 mH; V_{dc} = 39.6 V		L_e = 0 mH	
Parameter ↓	Measured	Calculated	Measured	Calculated
P_{gen} (kW)	4.25	4.2	6.68	6.6
η_g (%)	90.4	91	93.6	94
T_d (Nm)	127	127.5	200	209
θ (deg.)	-	52.5	-	2.6
V (V)	49.9	50.3	49.9	50.3

4.2.6 Current and voltage harmonics

Depending on the external inductance value inserted in the wind generator system, the rectifier-battery load can create non-sinusoidal currents on the ac-side of the rectifier. Current harmonics are created because of the non-linear relationship between the voltage and current in circuits containing a diode rectifier [47]. Harmonics like these produce an acoustic noise which is emitted by the generator. This noise can be annoying or even disturbing. Research has been done on air-cored generators of the axial flux kind that show the current harmonic effects [24]. These current harmonics are a function of the system inductance and the difference between the generated voltage of the wind generator and the ac-equivalent voltage of the battery bank. The order of these harmonics is shown by [24] to be

$$h_h = 6k \pm 1, \tag{98}$$

where h_h is the order of the harmonics and k is any integer. The 5th harmonic is the most dominant while the 7th, 11th and 13th are smaller [24]. This is shown in the following section.

Total harmonic distortion of the rated generated voltage and rated current

An advantage of the concentrated coil air-cored generator is that the generated back-EMF voltage is very close to being pure sinusoidal as shown in Fig. 47. The measured per-phase open circuit back-EMF voltage (at 300 r/min) is shown in the time domain plot of Fig. 55 (left). Also shown (right), is a frequency domain plot of the voltage waveform. A Fast Fourier Transform (FFT) was done on the

measured data points to obtain the amplitudes of each of the harmonics present in the signal. The dominant frequency is of course at 80 Hz with many smaller frequencies superimposed on top of it.

The amount of distortion in the voltage or current waveform is quantified by means of an index called the total harmonic distortion (THD). Total harmonic distortion is defined as the ratio of the sum of the powers of all harmonic components to the power of the fundamental frequency [47]. Harmonic distortion of the voltage waveforms in an electric circuit only occur in circuits with inductive or capacitive components and are absent in pure resistive circuits. Electronic switching devices like diode bridges also cause distortion. A smaller THD gives a more sinusoidal shaped waveform and the THD of a pure sinus wave is 0 %. The THD of the voltage or current can be calculated from [47] as

$$ THD_V\,(\%) = \frac{\sqrt{\sum\limits_{n=2}^{\infty} V_n^2}}{V_1} \quad \text{or} \quad THD_I\,(\%) = \frac{\sqrt{\sum\limits_{n=2}^{\infty} I_n^2}}{I_1}\,, \tag{99} $$

where V_n (or I_n) is the voltage (or current) amplitude of the nth order harmonic frequency and V_1 (or I_1) is the voltage (or current) amplitude of the fundamental frequency. For this particular design the THD is 1.5 %, which is considered as very good.

The time domain plot of the rated per-phase operating current waveform, I_r, with an external inductance of L_e inserted into the battery loaded system is shown in Fig. 56 (left). The corresponding frequency domain plot of the current waveform is shown on the right. The amplitude axis is plotted on a $\log_{10}$ scale. Note specifically the 5th ($f = 426.5$ Hz) and 7th ($f = 597.1$ Hz) current harmonics that are higher. According to (98) the small 2nd, 3rd, 4th and 6th harmonics should not be present. Their presence in this case however can be attributed to measurement noise. The THD of the rated current waveform is calculated by (99) as 2.4%.
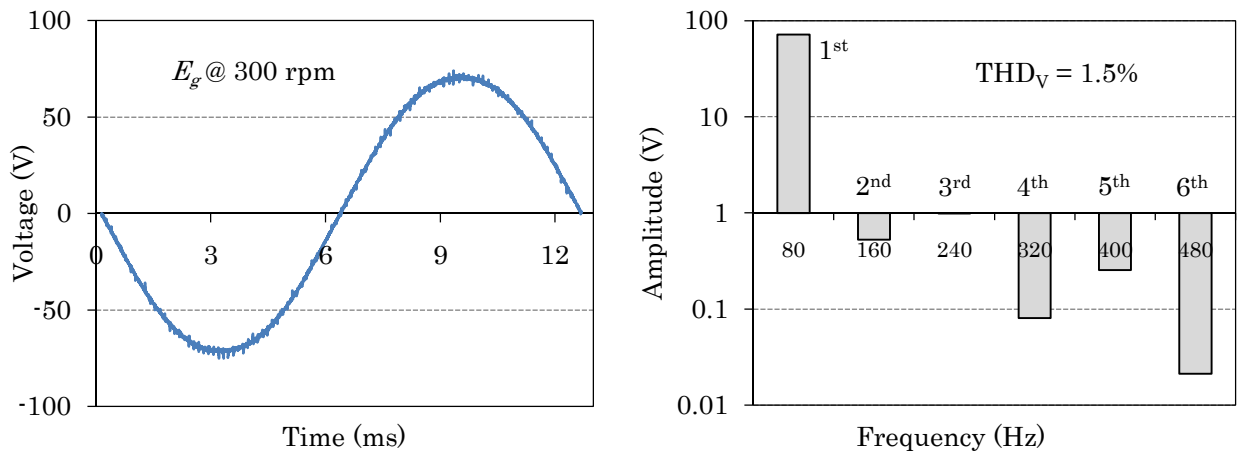

Fig. 55: Back-EMF voltage at 300 r/min in the time domain (left) and FFT analysis in the frequency domain (right).
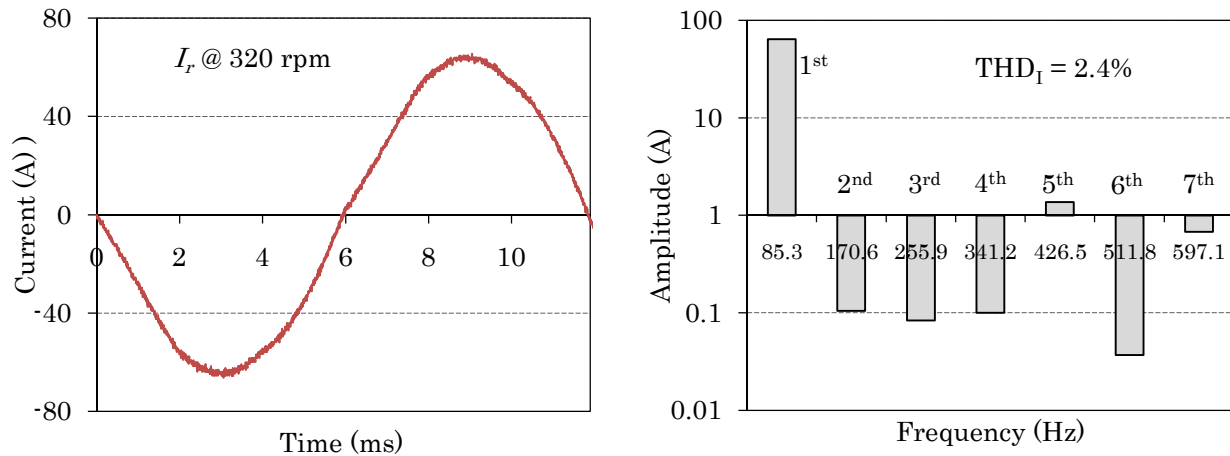
Fig. 56: Rated per-phase line current at 320 r/min in the time domain (left) and FFT analysis in the frequency domain (right).

4.3   Mass and cost of the prototype

It is very important to record and investigate the mass distribution of the RFPM air-cored generator. This is in part due to the fact that the mass of such a generator is closely related to its production cost. Even more important, however, is the fact that the generator has to be mounted on top of a tower and an increase in the tower top mass entails an increase in tower size and cost. Therefore to minimise the cost of the generator and the tower, one has to minimise the generator mass.

The mass distribution in this case is divided into major component categories. A pie chart of the mass distribution of the generator is shown in Fig. 57. From this chart one can see how the two iron rotor yokes are the dominating mass. This was expected because of the large diameter and thick walled steel ring needed for the yoke construction. The thickness of the rotor yoke is dictated by electromagnetic considerations as described in previous sections. Also evident is the rather high percentage of permanent magnet material present in the generator. These rotor magnets also contribute to a large portion of the generator mass. For this reason these two categories received the most attention in terms of minimising the mass. The mass was simulated using *Autodesk Inventor 9* and verified with laboratory measurements.

Also of great importance is the cost estimation of the prototype generator. Cost per energy is one of the main driving factors behind generator development. The cost can be divided into two categories, namely material cost and labour cost. Development cost is omitted as this will become only a small percentage when the generator is mass produced. Both of these, but especially labour costs, will also decrease in mass production. This may significantly change the cost distribution that was obtained in this prototype. For the purpose of the study both the material and labour costs of individual parts were summed together and the result is shown in Fig. 58. Again the rotor yokes

dominate the graph at 34 % with the magnets coming in a close second. In the case of the magnets 50 % of the cost can be ascribed to shipping. A local magnet manufacturer is thus desirable. It should be noted that the cost of the prototype is very high and that mass production will decrease these costs considerably.
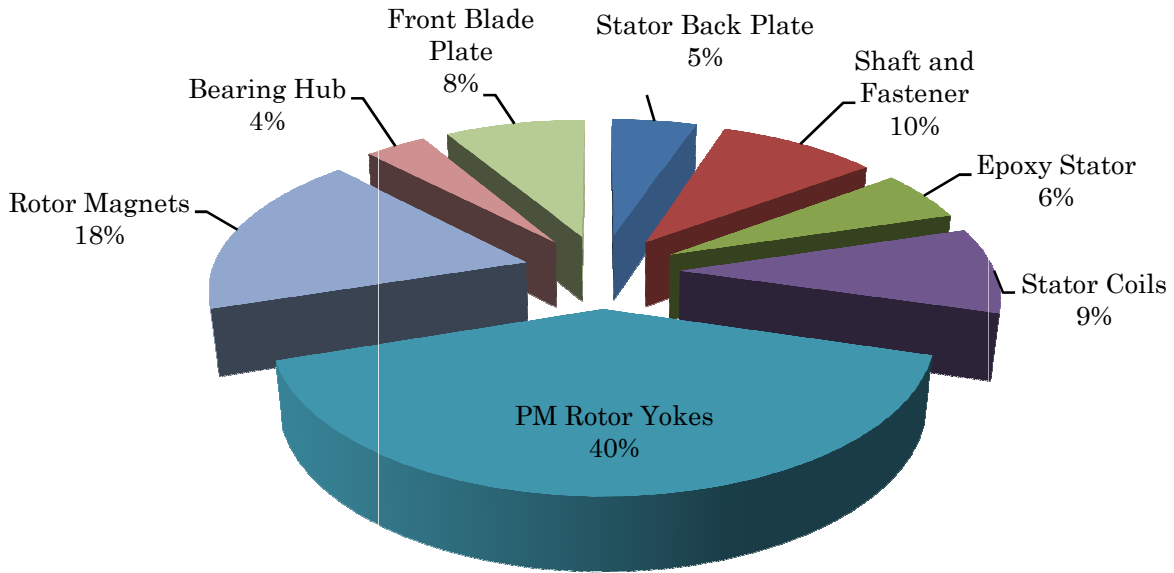
Fig. 57: Mass distribution of the prototype generator.
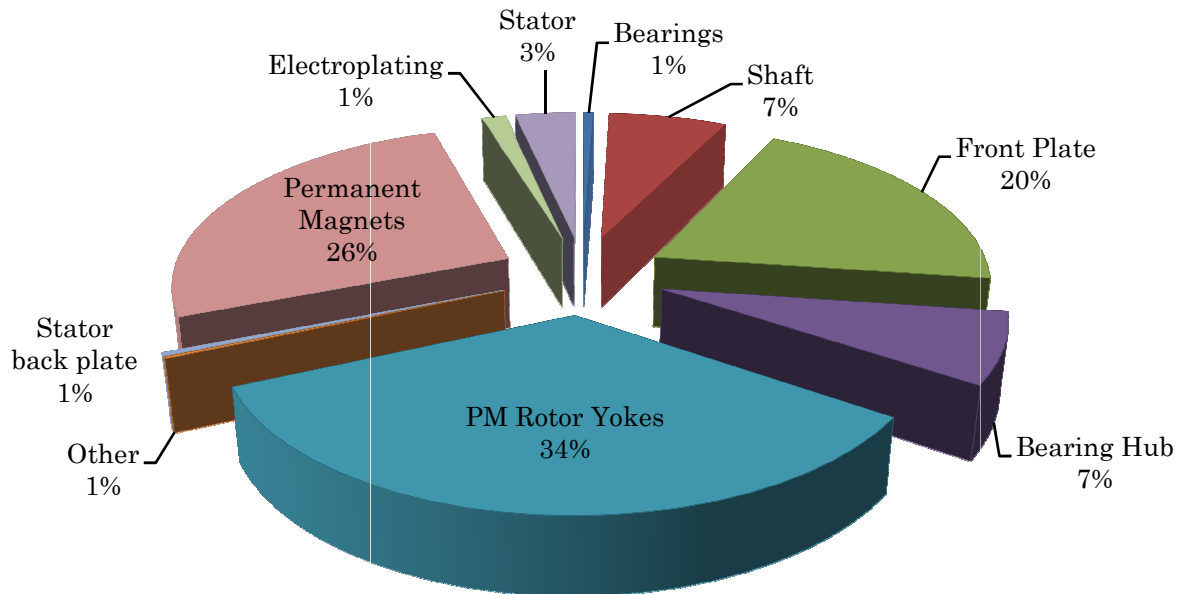
Fig. 58: Cost distribution of prototype generator.

Chapter 5
Comparison of three different generation systems

There are numerous stand-alone battery charging wind turbine system designs, each with its own advantages and disadvantages. In this chapter three system designs are discussed. Two of the designs are well established technologies both of which are widely used. The third design is a new proposal. The content of this chapter was presented as a research paper at the 2010 South-African Universities Power Engineering Conference (SAUPEC) in Johannesburg.

Introduction

In this study three different battery charging wind turbine systems are investigated and compared in terms of efficiency and energy-production per cost. The method whereby the total annual energy capture for each of the systems is calculated is explained in this chapter. The chapter also illustrates how the system components affect the total energy supply to the electrical load. An explanation of the estimated costs and the energy production per cost of each of the three systems, is given.

Wind turbine power capture

Electricity production obtained from a wind source at a given wind speed and with a particular wind turbine, varies a lot depending on the site's wind speed distribution. For example, a wind turbine will produce much more power at a site where the wind speed is 12 m/s for 50 % of the time and 0 m/s for the other 50% of the time than on a site where the wind speed is 6 m/s for 100 % of the time. This is due to the fact that the power available in the wind is proportional to the cube of the wind speed as seen in (2). Even though the annual average wind at two different sites may be equal, the site with the higher wind speeds will still have higher average kinetic energy available in the wind.
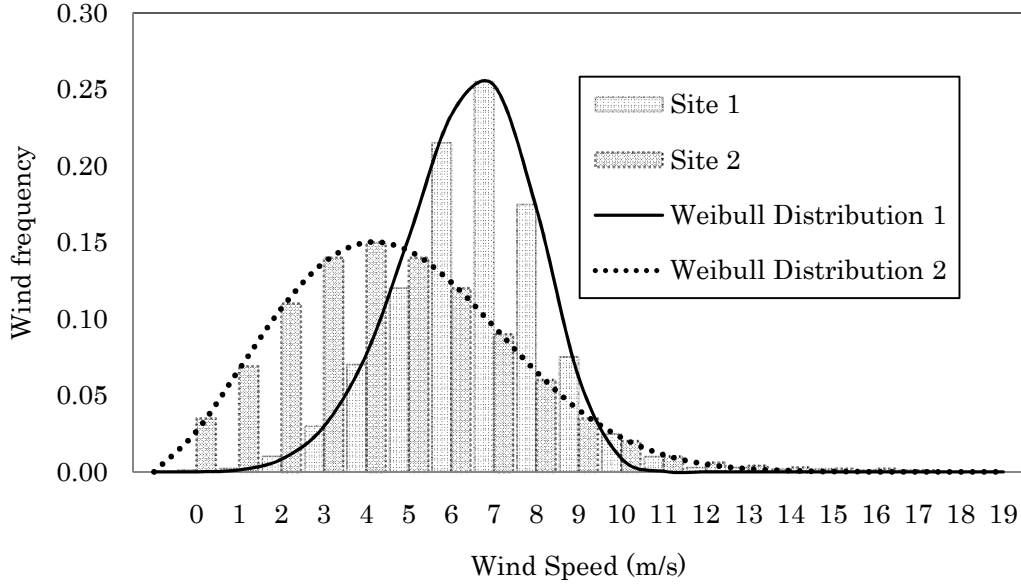
Fig. 59: Weibull wind speed distribution at different wind sites; Frequency of occurrence versus wind speed.

For most areas the wind speed distribution can be approximated by a Weibull plot as shown in Fig. 59. The Weibull curve can be calculated by

$$p(v) = \frac{k_s}{c}\left(\frac{v_W}{c}\right)^{k_s - 1} e^{-\left(\frac{v_w}{c}\right)^{k_s}}, \tag{100}$$

where *p(v)* is the probability density function of the wind speed v_w, k_s is the shape parameter and *c* is the scale parameter. By changing the scale and shape variables, the wind plot can be altered to represent almost any site. In Fig. 59, site 1 (Weibull distribution 1) has a better annual power production capability than site 2. Depending on the wind speed, v_w, at a particular site, the turbine power production can be calculated by considering the turbine blade power curves. In this study 1.9 m turbine blades were used. This equates to a swept area, A_s, of 11.3 m². The blade's power curves are represented in Fig. 7. The power curves are obtained by calculating the mechanical power of the turbine rotor by (3). C_p is usually given as a function of the tip speed ratio in (4). Hence, rewriting (3) and substituting into (4) results in

$$P_m = \frac{1}{2}\rho_a A_s C_p \left(\frac{r_b}{\lambda_s}\right)^3 \omega_m^3. \tag{101}$$

Thus, for a given wind speed and blade radius the available rotor power can be plotted versus the turbine speed. The peak power at each wind speed can be realized if the turbine's optimal tip speed ratio, λ_{opt}, is maintained. This implies a maximum power coefficient, C_{pm}, as shown in Fig. 1. This results in [38]

$$P_m = \frac{1}{2} \rho_a A_s C_{pm} \left(\frac{r_b}{\lambda_{opt}} \right) \omega_m^3 \ .$$ (102)

The optimum tip-speed-ratio can be guaranteed by using an electronic active rectifier to control the generator at the optimum turbine-load speed [39].

5.1 Three alternative generation systems

In this section the three wind generator systems, shown in Fig. 60 – 61, are described. Each of the systems utilizes the same type of generator, namely the air-cored permanent magnet (PM) direct drive generator discussed in this thesis. Research presented in this thesis shows that this type of generator is a good alternative to iron cored generators, particularly in small rural wind energy systems. The air-cored PM generator has numerous advantages such as no core losses, zero cogging torque and no magnetic attraction forces between the rotor and stator.

Each of the systems also employs the same turbine blades and, thus, has the same energy capture potential. Further aspects to be noted, similar to all three systems, is the presence of a battery charge controller. The charge controller ensures safe operating conditions for the batteries by dumping surplus power in resistors when the batteries are near a state of full charge [15]. This component is inactive most of the time and for the purpose of this study is omitted.

5.1.1 Passive controlled system

The first system to be addressed is known as a passive controlled system. This system is also the one discussed in this thesis. A simplified illustration of the passive controlled system is depicted in Fig. 60. It is currently the most widely used system because of its simplicity. Such a system is used by [15] and [45] to provide power to a 230 V grid connection. A 32 – 46 V battery bank coupled to the grid or stand-alone load via an inverter and transformer is common practice. The system in Fig. 60 comprises of an air-cored PM generator with a generated back-EMF voltage E_g, a cable with an impedance Z_c, an external inductance with a reactance X_e, and a diode rectifier that is directly connected to a battery bank. From the battery bank the inverter and transformer converts the power to a fixed frequency, fixed voltage, three-phase stand-alone power supply, to be connected to the loads.

In this system maximum power point tracking cannot be realized due to the passive diode rectifier control. The external inductance is used to ensure sinusoidal phase currents, to reduce generator noise and to obtain better power matching with the turbine at all wind speeds. The external inductance, however, causes the generator to be oversized in its design, which increases the cost of the generator in this system.
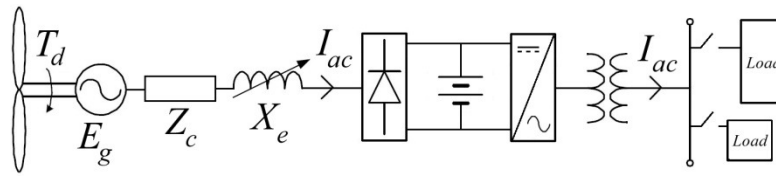
Fig. 60: Passive controlled system.
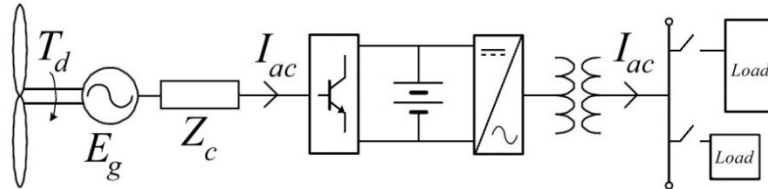
Fig. 61: Active controlled system.
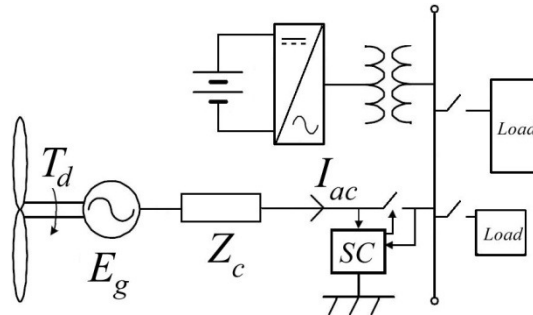
Fig. 62: Fixed speed system

5.1.2 Active controlled system

A simplified illustration of the active controlled wind generator system using an active synchronous rectifier is depicted in Fig. 61. This system comprises of the same components as the passive controlled system, with the exception of the external inductance and the diode rectifier. The external inductance is no longer needed and the diode rectifier is replaced with a current controlled active rectifier.

In contrast with the passive system, the active controlled system utilizes turbine speed control by adjusting the load on the wind turbine and generator [14]. The load on the generator is adjusted by controlling the current of the generator by means of the active rectifier. By loading the generator in an optimum way, maximum power transfer from the turbine to the battery bank is obtained. This system is considerably more expensive due to the active rectifier. However, this system produces maximum power at each wind speed, a feat that makes it an attractive option. The generator also does not have to be oversized in its design as in the case of the passive system; the reason is that the generator is controlled at maximum power conversion efficiency by means of the active rectifier.

5.1.3 Fixed speed system

A simplified illustration of the fixed speed wind generator system is depicted in Fig. 62. As is shown the generator in this case is connected directly to the fixed voltage and fixed frequency battery powered stand-alone grid inverter supply. The turbine and generator, thus, operate at a fixed speed at all wind speeds. The synchronization controller (SC) in Fig. 62 synchronizes the generator with the stand-alone grid inverter-fed supply and keeps the generator synchronized with the supply. In the cases of gusty winds or no wind conditions the SC will disconnect the generator from the mini-grid supply. The possibility and stability of the direct connection of the air-cored generator to the mini grid, are aspects that still have to be investigated. This is, however, beyond the scope of this thesis and, in this study, the connection is assumed to be not only possible but stable as well.

Unlike the previous two wind generator systems, the generator in this case is a high voltage generator. It is, therefore, connected to the mini-grid inverter-fed supply by means of a much thinner high voltage cable; this results in considerably lower I^2R cable losses. A further advantage of the high voltage transmission cable is that it allows for a much longer distance between the wind turbine and the mini-grid supply. The inverter in the fixed speed system is used to charge the batteries in the case of a surplus amount of power supplied from the turbine to the mini-grid. When the wind generator stops producing power, the battery bank will produce power to the stand-alone grid via the inverter and transformer. The inverter-transformer combination will ensure a steady grid voltage and frequency. It should be noted however, that this system's inverter needs to be rated according to two different conditions. Firstly, it has to be rated according to the maximum electric load condition of the fully utilized grid. Secondly, it has to be able to handle the highest amount of generated power from the wind turbine when a strong wind is blowing and all the loads are switched off. This latter condition can be overcome if a simple controller switches on a load, e.g. a water heating geyser, to dump the additional power when a surplus is generated. The optimum speed of the fixed speed wind generator system is determined by obtaining the speed at which the turbine produces the highest annual energy. The method of calculating the annual energy produced by the turbine is described in the following section. The fixed operating speed at which the highest overall energy is produced for site 1 in Fig. 59 and the turbine power curves of Fig. 7 is found to be at 310 r/min.

5.2   Comparing system performance and cost

5.2.1 Annual energy production

The annual energy production can be calculated from the site's annual wind speed distribution and the turbine's performance at these wind speeds. In Fig. 63, the turbine power of each of the three wind generator systems are plotted at each wind speed, for wind speeds of 3 – 14 m/s. The optimum power points of the actively controlled system are calculated by (102), while the fixed speed

system's power points are calculated by (101) with a fixed speed of 310 r/min. The power points of the passive controlled system are calculated from the known system parameters of Fig. 60 and by measurements in section 4.2.4.
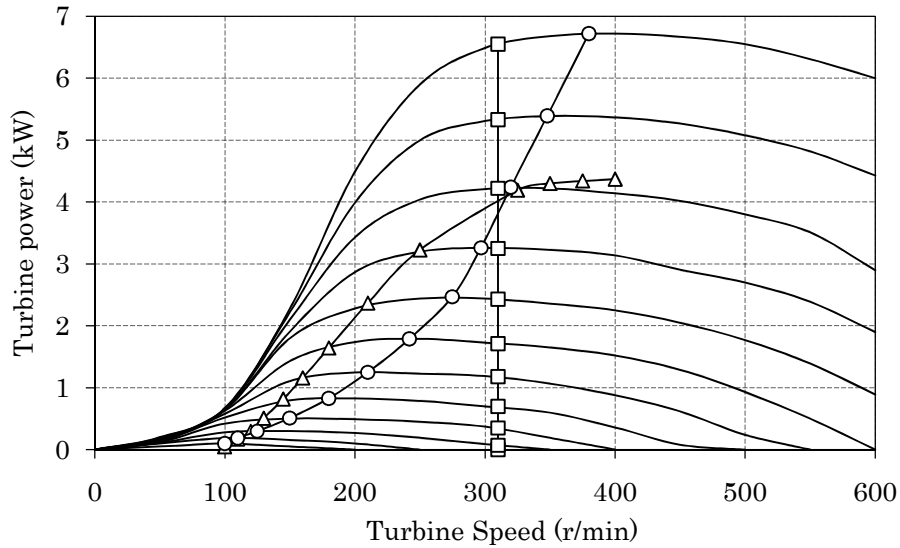
Fig. 63: Generated wind power curves for three systems.
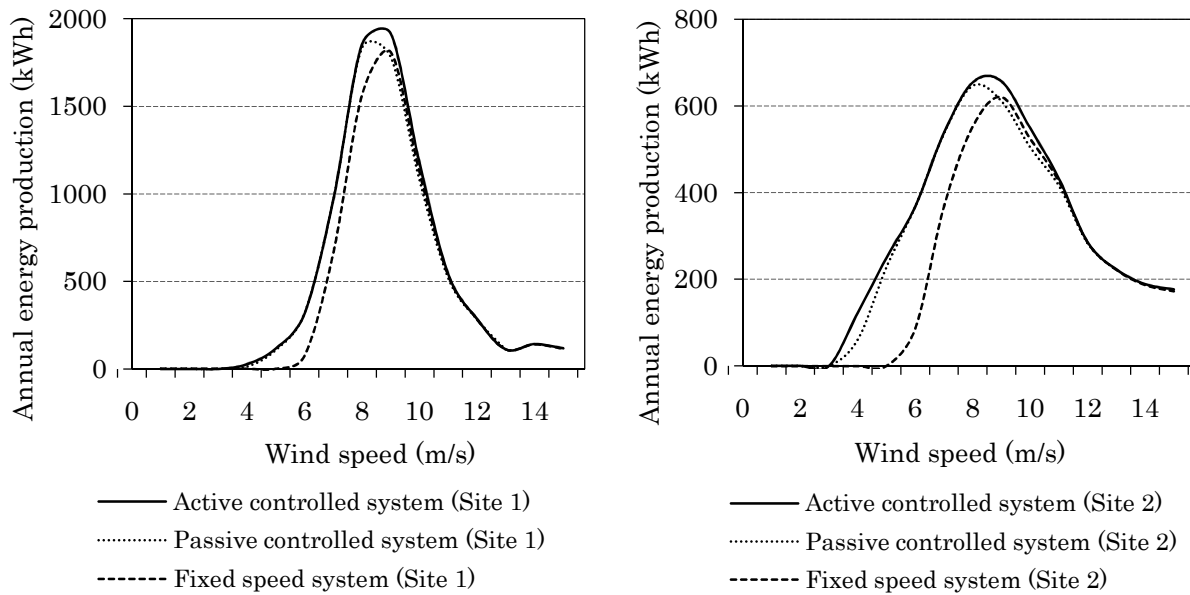
Fig. 64: Annual system energy versus wind speed at site 1 and 2.
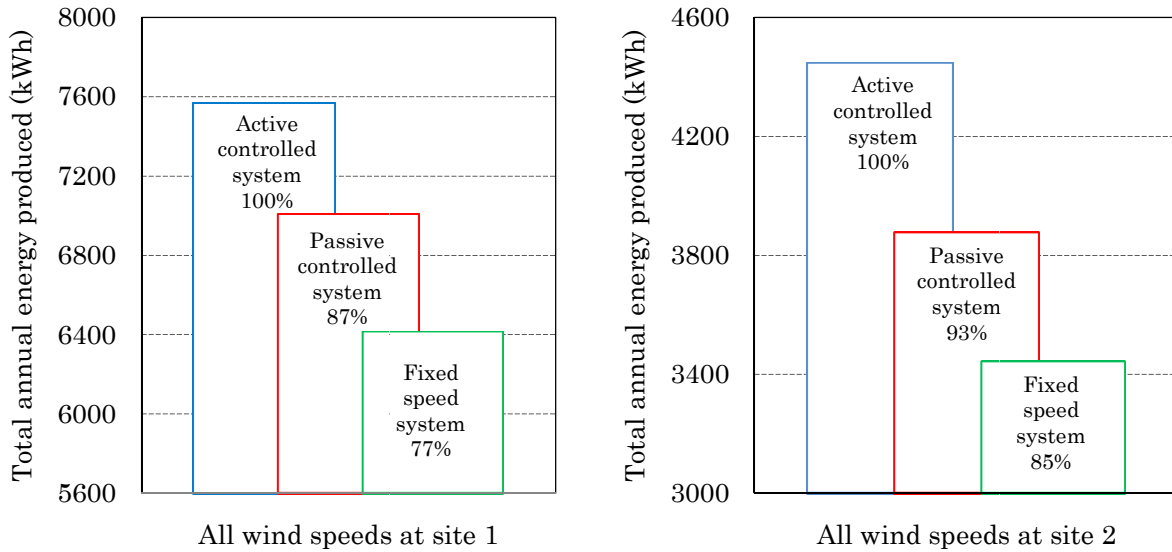
Fig. 65: Total annual system energy captured at site 1 and 2.

To obtain the annual system energy produced versus wind speed, the three power plots in Fig. 63 are multiplied by the annual wind speed distributions of Fig. 59. The results for site 1 and site 2 are shown in Fig. 64, right and left respectively. These two figures show how site 1 produces more energy than site 2 because of its higher wind speeds. It is clear that the fixed speed system performs considerably better at higher wind speeds. All three systems are shown to have similar energy plots for wind speeds of 9 m/s and above.

The total annual energy per site is calculated by integrating the curves of Fig. 64. The total annual energy, in kWh, produced at site 1 is shown in Fig. 65 (left). As expected, the actively controlled turbine performs the best of the three systems as it converts maximum power at each wind speed. The passive controlled system performs second best at 93 % of the active controlled system. Lastly, the fixed speed system produces 85 % of the maximum possible energy. Fig. 65 (right) shows the total annual energy produced by each of the three systems at site 2. In this case the fixed speed system produces only 77 % of the maximum possible energy.

A good way to quantify the delivered energy per annum is known as the capacity factor. It is defined as the ratio of actual average power to the rated power of the wind generator system, measured over a year period [3]. The capacity factor, thus, is given by,

$$C_f = \frac{P_{aa}}{P_{gr}} , \tag{103}$$

where P_{aa} is the annual average turbine power (calculated from Fig. 65) and P_{gr} is the rated generator power of 4.2 kW from Fig. 63. Table 5 lists the capacity factor of the three systems at the two wind sites.

Table 5: System capacity factors.

Site	Turbine capacity factor		
	Passive	**Active**	**Fixed**
Site 1	19%	20.6%	17.4%
Site 2	10.5%	12.1%	9.4%

5.2.2 System efficiency

The conversion efficiency of a system, from the kinetic energy in the wind to the useful electrical power delivered to the load, is the product of all the individual component efficiencies present in the system [1]. Various power losses occurring throughout the system decrease its power conversion efficiency. Fig. 66 shows a power flow diagram of a wind generator system together with its losses. P_w is the power available in the wind. P_m is the extracted power from the turbine that is supplied to the sub-system. P_o is the useful power delivered to the stand-alone mini-grid.

The efficiencies of the components of the sub-system used in the calculations are estimated averaged values of common, of-the-shelf available components. Table 6 gives the estimated efficiencies of each of the components as well as the overall efficiency of the systems for the two wind sites considered. Note that the efficiencies should ideally be taken at the annual average power level, P_a, of (103).

Table 6 shows some interesting differences between the passive, active and fixed speed wind generator systems. Firstly, the transmission cable needed for a high voltage system is much more effective than a low voltage high current cable. Secondly, since the components of the passive and active wind generator systems are connected in series, all the efficiencies are multiplied to give the overall system efficiency.
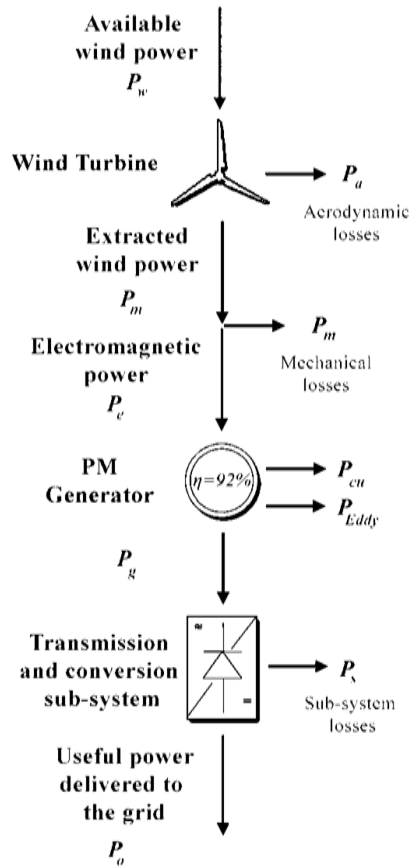
Fig. 66: Total system losses.
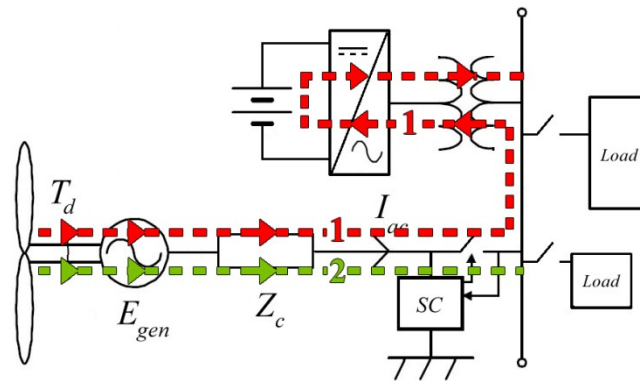
Fig. 67: Power paths in the fixed speed system.

The fixed speed system, on the other hand, has two parallel power flow paths, as shown in Fig. 67. This implies that two scenarios must be considered. The first scenario (path 1 in Fig. 67) is where the turbine produces power to the batteries with all the loads switched off, followed then by a time-period when the batteries supply power to the load with no power from the wind turbine. This scenario is the worst in terms of efficiency as it takes seven conversions (including the battery) before the power reaches the load. The second scenario (path 2 in Fig. 67) is where the turbine

produces all its power to the stand-alone grid load. In this case the generated wind power is directly supplied to the load, consequently at a high efficiency as only two conversions take place. To simplify the efficiency calculation of the fixed speed system, the average efficiency of the two power flow paths is taken as the overall efficiency of this system, as given in Table 6. From the overall efficiency results in Table 6 it is clear that the efficiency of the fixed speed wind generator system is the same or higher than that of the passive controlled system. If the sub-system efficiency is taken into account in the calculation of the capacity factor of (103) called the sub-system capacity factor, C_{fs}, then this factor can be used as a method of comparing wind generator systems. The C_{fs}-percentages of the three wind generator systems are compared in Table 7. From this it can be seen that when the sub-system efficiency is also taken into account, the active controlled system's capacity factor drops to just above the other two systems.

Table 6: Efficiency of system components at rated speed.

Components	Component efficiencies		
	Passive	Active	Fixed
Wind turbine energy capture (site 1, Fig. 65)	93%	100%	85%
Wind turbine energy capture (site 2, Fig. 65)	87%	100%	77%
RFPM Generator efficiency	92%	92%	92%
Transmission cable	96%	96%	99%
External Inductor	95%	-	-
Diode rectifier	98%	-	-
Synchronous MOSFET rectifier	-	96%	-
Inverter and transformer	93%	93%	93%
Total component efficiency (site 1)	71%	79%	70%
System efficiency between turbine and grid (site 1)	71%	79%	77%
Average system efficiency (site 1)	-	-	74%
Total component efficiency (site 2)	67%	79%	61%
System efficiency between turbine and grid (site 2)	67%	79%	70%
Average system efficiency (site 2)	-	-	66%

Table 7: Sub-system capacity factor, C_{fs}.

Site	Sub-system capacity factor		
	Passive	Active	Fixed
Site 1	14.5%	16.2%	15.2%
Site 2	8.1%	9.5%	8.1%

5.2.3 System component cost

The cost of each system component should also be investigated to determine the energy production per cost of each wind generator system. Generic costs are formulated for the components based on industry averages. Table 8 shows the per unit cost of each component of the systems based on the PM generator cost of the passively controlled wind generator system.

From Table 8 one can see that the most economical system in terms of component cost is the fixed speed system. The passive controlled system is also cheaper than the active controlled system. This system is easy to install and to maintain, these being the primary reasons for its wide use. The active controlled system has a very expensive active rectifier. Current rule of thumb estimates a cost of R 2500/kW for power electronic converters in renewable energy applications. The per unit annual energy production per cost of the systems can be determined by dividing the overall system efficiency of Table 6 with the per unit system cost of Table 8. These results are given in Table 9. It is clear that the fixed speed system completely outperforms the other systems in this regard.

Table 8: Per unit system component cost.

Components	Sub-system component costs		
	Passive	Active	Fixed
RFPM Generator	1	0.9	0.9
Transmission cable	0.22	0.22	0.1
External Inductor	0.05	-	-
Diode rectifier	0.05	-	-
MOSFET rectifier	-	0.9	-
Inverter and transformer	1	1	1
Synchronizing controller	-	-	0.2
Total cost	2.32	3.02	2.2

Table 9: Sub-system energy production per cost.

Components	Sub-system energy production per cost		
	Passive	Active	Fixed
Site 1	0.31	0.26	0.34*
Site 2	0.29	0.26	0.3*

*Depends on the matching of the load and the delivered wind power

5.3   Choosing the best system

To choose the best system for a particular application one has to look at the wind conditions at the specific site and also the load characteristics in which the generator system will be implemented. Further considerations may include the cost and complexity of the system. Even though it was found in this chapter that one system performed better than the others, this does not necessarily mean that this will always be the case. As shown, the system performance and ultimately efficiency is highly site dependent.

From the results of the comparative study of the three considered 4 kW air-cored PM wind generator systems for battery charging stand-alone inverter supplies, the following conclusions are drawn:

- For good and moderate wind sites it is found that the fixed speed wind generator system captures 15 – 23 % less annual wind turbine energy than the variable speed maximum power point wind generator system.

- If the subsystem efficiency, however, is taken into account in the calculations, then the annual energy produced to the load by the fixed speed wind generator system is only 6 – 16 % less than that produced by the variable speed maximum power point wind generator system.

- It is shown that the capacity factors of the wind generator systems and wind sites can only be used as a method of comparison if the subsystem efficiency is included in the calculation.

- The cost of the fixed speed wind generator system is found to be substantially lower than that of the other two wind generator systems considered. Hence, with the annual energy delivered to the load less, but the cost of the system also less, the energy production per cost of the fixed speed wind generator system is shown to be much better than that of the other two systems.

Chapter 6
Conclusions and Recommendations

6.1   Conclusions

An analytical calculation method is developed whereby the electromagnetic and mechanical design of the double rotor air-cored stator RFPM machine can be optimised subject to performance constraints. The design method includes the effect of magnetic saturation. The analytical method is proved to be very accurate, thus, electromagnetic and mechanical FE analyses are not necessary per se in the design of this machine. Specific conclusions from this study are summarized as follows:

- Mathematical derivations show that there is a specific function relationship between the axial length and average diameter of the machine that always satisfies the required power and efficiency of the generator. This simplifies very much the analytical design optimisation of the generator.

- If copper losses and current density are constants in the design optimisation, it is shown that the mass of copper is also a constant independent of the dimensions of the machine. In this regard it is not necessary to consider the copper mass in the active mass objective function.

- The strongest magnet grade must be used in the design of the air-cored RFPM machine as this substantially decreases the machine mass with only a marginal increase in cost.

- Equal priority must be given to the different active masses of the generator in the minimisation of the mass objective function, rather than to give a higher priority to the magnet mass minimisation.

- The electromagnetic design and not the mechanical design determines the rotor yoke heights and, thus, the mass and cost of the cylinder yokes. This finding is believed to be valid for most design cases as the finding is based on a machine with already a high number of poles (p = 32) and a high rated frequency (85.3 Hz). It is interesting to note that the opposite has been found for air-cored stator AFPM machines [15].

- The total mass of the constructed RFPM wind generator is 59 kg, which is about 36 % less than the 92 kg mass of an equivalent air-cored stator AFPM wind generator. This is a

significant improvement and shows that the relatively thin cylindrical rotors of the RFPM machine are strong enough to withstand the magnetic attraction forces.

- It is found for the prototype air-cored stator RFPM wind generator that the construction mass amounts to only 27 % of the total mass of the generator.

- It is shown that the defined rated power of the air-cored stator RFPM wind generator depends on the electrical load system it is connected to. For the prototype wind generator this is found to vary from 4.2 kW to 6.6 kW for generator efficiencies not less than 90 %.

- It is found from a theoretical study that the fixed speed battery charging system, proposed in this thesis, is respectable when comparing the systems' efficiency and cost with those of the passive and active controlled systems.

6.2   Recommended further study

The thesis presented is not without shortcomings. These could be addressed in further studies. Some suggestions to further the research are given below.

Electrical aspects:

The copper wire that was used to build this prototype generator is round annealed polyamide coated copper wire. In this application the wire had to be stranded and transposed by hand. This has a detrimental effect on the filling factor. A proposed solution could be to use Litz wire instead. Windings constructed of this wire would have a better filling factor and better insulation properties. In Appendix B the use of Litz wire to minimise eddy-losses is also discussed.

Mechanical aspects:

Further mechanical optimisation could be done on the construction mass of the generator. The construction mass of the generator accounts for almost a third of the generator mass, which leaves room for improvement. For example, a hollow shaft could be used instead of a solid shaft.

In this study only static loads were considered in the mechanical strength calculations. The investigation of dynamic and cyclic loads on the generator components should also be done to protect against fatigue failure. The erratic nature of wind makes this a necessity for the tower and blade designs, but also for the generator design. This is especially true for parts constructed of Aluminium since this metal has no fatigue limit.

Accurate placement of stator coils in the mould should also be investigated. When stator coils are connected in parallel their positions relative to each other should be exact to eliminate electrical imbalances. In this type of generator, one mechanical degree shift is equal to a p/2 = 16 electrical degree shift. This condition is equally true for the placement of the permanent magnets.

Miscellaneous aspects:

Further study needs to be done to compare the classic PM iron-cored generator to a PM air-cored generator of the same size and rating. Provided that the two generators are of the same rating (in terms of power, torque, etc.) these generators could be compared in terms of voltage quality, current harmonics, torque quality (torque ripple and cogging torque), generator efficiency, grid connection options, cost, mass and generated noise levels. The two generators should be tested side-by-side in the same system and on the same load. This would give a good indication of the advantages, and possible disadvantages of the air-cored generator over its iron-cored counterpart.

Further study also needs to be done on the fixed speed system of Fig. 62. As shown in the previous chapter, this could be a good alternative to the passive controlled diode rectifier system used in this thesis.

Appendices

Appendix A
External Inductor Design

One of the disadvantages of air-cores machines is the low internal inductance that these generators possess. This causes the generator to not operate at its maximum power points, greatly lowering the overall system efficiency, and also making the generator exhibit above desired acoustic noise. Fortunately, this can be corrected by placing an extra external inductor, L_e, in series with each of the phases of the machine.

The extra external inductance needed in an air-cored machine to increase its low internal inductance, as discussed in this thesis, is designed and built. A three phase inductor is needed; one with a separate core for each of the machine phases. In this design each of the cores consists of two stacked C-cores, shown in Fig. 70. An alternative three phase solution can be realized with two E-cores stacked on top of each other. Fig. 68 represents the ac-equivalent per-phase circuit of the RFPM generator connected to a battery charging load.

Inductors are fairly simple to design and easy to build. Other advantages include the low cost of the materials and accurate inductance values attainable.

There are however some disadvantages associated with an inductor with a permeable core. The oscillating electric current through the coils induces an oscillating magnetic field in the core and because the core is typically iron, eddy currents are induced which dissipate energy strongly as heat.
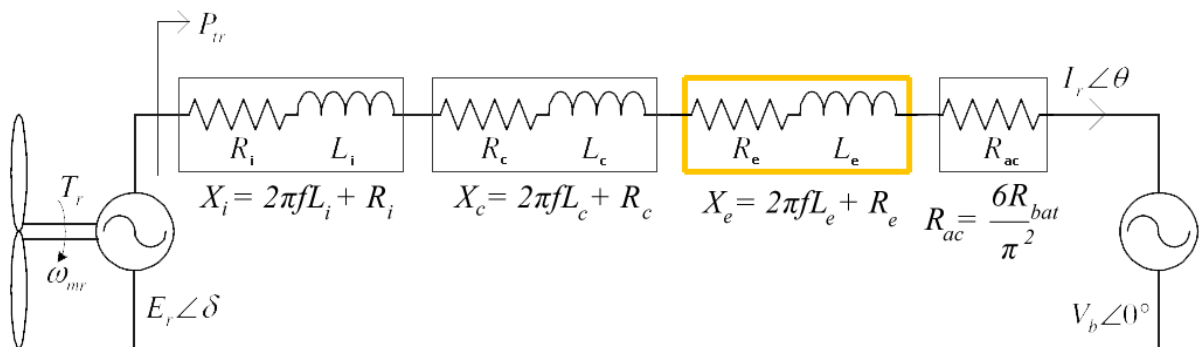

Fig. 68: Per phase ac-equivalent circuit of the RFPM generator connected to a battery charging load.
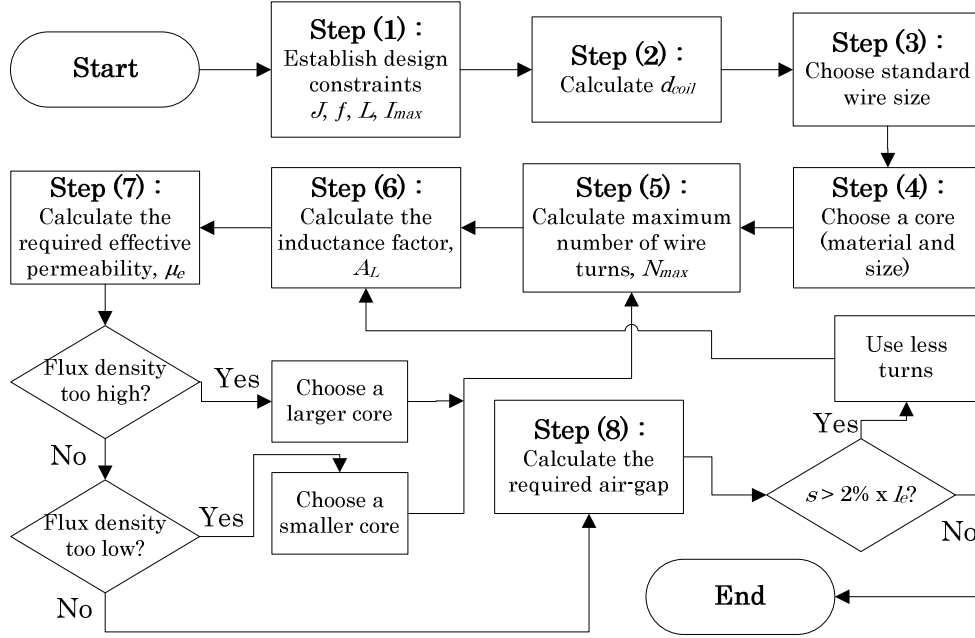
Fig. 69: Flow diagram for designing an inductor.

A method for reducing this effect is to construct the iron core of the inductor out of laminated layers, which has the effect of blocking the conduction of the eddy-currents and so minimizing these losses considerably.

The objective in this Appendix is to design an inductor having a given external inductance L_e, which carries a worst-case current I_{max} without saturating, and which has a given winding resistance R_e, or, equivalently, exhibits a worst-case copper loss of $P_{Cu} = I_{max}^2 R_e$. The task of designing a high current, low voltage inductor is a rather iterative process. The design approach will be discussed by means of a flow diagram shown in Fig. 69.

In step (1) the design constraints are established. These are the current density (J), operating frequency (f), desired inductance (L) and the maximum worst-case current (I_{max}) in the coils. The maximum worst-case current can be calculated from

$$I_{max} = I_{dc} + \frac{\Delta I}{2}, \tag{104}$$

where I_{dc} is the direct current component of the current through the inductor and ΔI is the deviation from the dc-value (i.e. an ac-ripple on top of a dc-current). I_{dc} can also be seen as the RMS value of the per-phase ac-current of the RFPM air-cored generator. Once these constraints are fixed, the copper coil thickness (d_{coil}) used in the inductor (step (2)) can be calculated by

$$d_{coil} = 2\sqrt{\frac{I_{max}}{\pi J}}, \tag{105}$$

where d_{coil} is the minimum coil diameter to ensure a safe operating temperature, I_{max} is the maximum worst-case current reached by the wire and J is the chosen current density. As a safe rule of thumb, current density for an inductor operating in an open environment area is between 4 and 6 A/mm².

In step (3) the wire is chosen from a manufacturer's available standard wire sizes so that the coil diameter is as close as possible to the calculated value, but not less. The inductor windings are standard enamel coated copper wire which is wound around a nylon bobbin rather than directly on the core. The bobbin protects the wire coating and can then easily be slid over the core to form the complete inductor.

Next, a core is chosen (step (4)). From the core manufacturer's catalogues we can obtain the magnetic path length, l_g, the core cross sectional area, A_c, the relative permeability, μ_r, and the window area, A_w. For ease of construction two core pieces are usually put together to form a "closed magnetic path". Unfortunately the surface roughness on the connecting interface introduces a small parasitic air-gap so that the permeability of the combined core construction becomes ±25′% lower than the initial permeability, μ_i, of the core's magnetic material. This new permeability is called the effective permeability, μ_e. As the surface roughness of the core material (i.e. the small parasitic air gap) varies, the value of the inductance factor will also vary, usually in the region of +30/-20 %. This implies that the value of the inductance will also have the same tolerance [48].

By introducing a small air-gap, $s \ll l_e$, the tolerance band of the calculated inductance (and inductance factor) is significantly reduced. The introduction of an air-gap also increases the reluctance value of the core resulting in a lower flux value and thus a lower flux density, B.

Fig. 70 shows a cross section of a laminated C-core with a pre-cut air-gap, l_c, on the right leg.
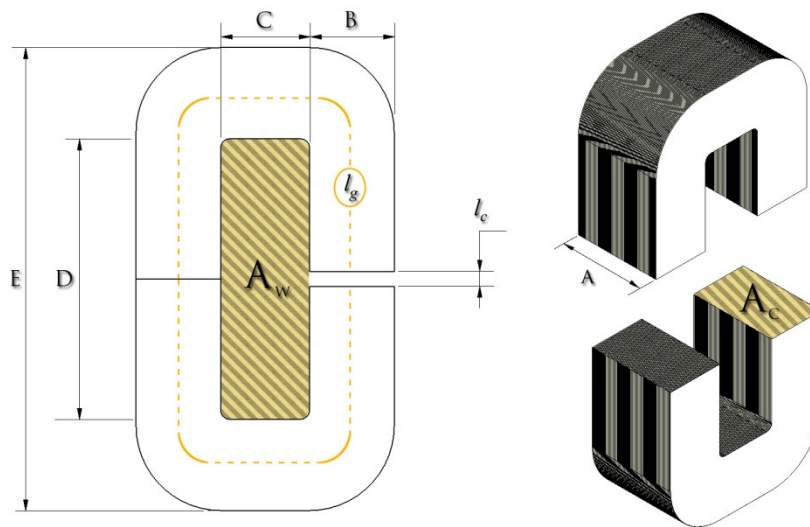

Fig. 70: Inductor core dimensions.

In step (5), the maximum number of coil turns which can fit into the chosen core's window area, is calculated. This is done with an acceptable copper fill factor. A fill factor (in some literature referred as a window utilisation factor [48]) represents the percentage of area occupied by the copper in relation to the total area available in the core's window area. The reason for this factor is that the round shape of the wire has to fit inside a square area. Again, a rule of thumb for choosing a fill factor is 0.55 for round wire. This means that for round wire only 55 % of the core window area will be filled by copper. If however rectangular wire is used this filling factor can be increased. Rectangular copper wire was used in this application. The fill factor for this type of wire is much better because of the snug manner in which the squares fit next to each other. This type of wire allows for a fill factor of approximately 0.8. The calculation is as follows:

$$N_{\max} = \frac{2 k_f A_w}{\pi d_{coil}}, \tag{106}$$

where A_w is the core's window area and k_f is the copper fill factor. When these parameters are known, the inductance factor, A_L, needed to realize the inductor with N_{max} turns is calculated in step (6). The inductance factor is given by

$$A_L = \frac{L}{N_{\max}^2}. \tag{107}$$

The inductance factor is the inverse of the reluctance and given by [48] as

$$A_L = \frac{1}{\Re_T}, \tag{108}$$

where $\Re_T$ is the total reluctance. The reluctance of a core is analogous to the resistance in an electric circuit. Fig. 71 illustrates a magnetic core in comparison to an electric circuit. It compares reluctance to resistance, magnetic flux to current and ampere-turns to a voltage source.
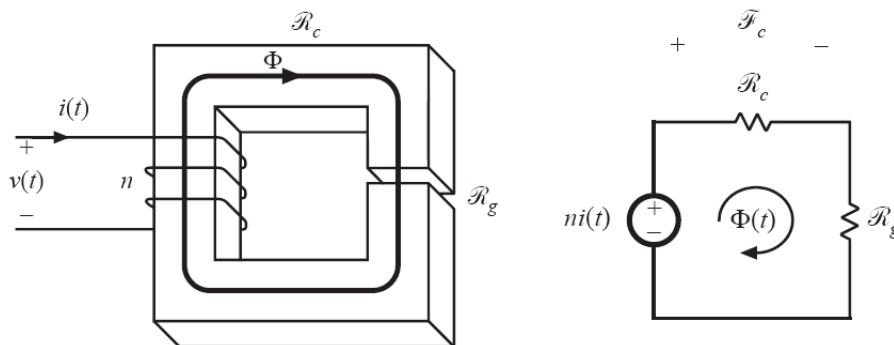

Fig. 71: A magnetic core compared to an electrical circuit.

The inductor, in this case, has an air-gap on the right leg which causes the circuit to have two separate reluctances; one for the core and one for the gap. The total reluctance consists of both these individual reluctances and is summed by [48] as follows,

$$\Re_T = \Re_c + \Re_g$$

$$= \frac{l_c}{\mu_i \mu_0 A_c} + \frac{l_g}{\mu_0 A_g}$$

$$= \frac{l_c + l_g \mu_i}{\mu_i \mu_0 A_c}$$

$$= \frac{l_c + l_g \mu_i}{\mu_i \left(l_c + l_g\right)} \left(\frac{l_c + l_g}{\mu_0 A_c}\right) \qquad \text{(with } A_c \approx A_g \;\; \& \;\; l_g \ll l_c) \qquad (109)$$

$$= \frac{l_c + l_g \mu_i}{\mu_i l_c} \left(\frac{l_c}{\mu_0 A_c}\right)$$

$$= \frac{l_c}{\mu_e \mu_0 A_c}$$

where,

$$\mu_e = \frac{\mu_i l_c}{l_c + l_g \mu_i}$$

$$= \frac{\mu_i l_c}{1 + \dfrac{l_g}{l_c} \mu_i} \qquad , \qquad (110)$$

where μ_e is the effective permeability, μ_i is the core material's initial permeability, l_c is the magnetic path length inside the core and l_g is the magnetic path length in the air-gap. In (109) $\Re_c$ and $\Re_g$ are the core and air-gap reluctances respectively, and A_c and A_g are the cross sections of both the core and air-gap. With A_L known the effective permeability, μ_e, can be calculated in step (7).

Since the reluctance of a medium is directly proportional to the inverse of the permeability of that medium, this makes the reluctance of the air-gap much higher even though its length is so much shorter. This reluctance usually dominates the total value. The assumption that A_c and A_g are approximately equal is a valid one provided the air-gap length is short enough. If the air-gap is too long, fringing flux will start to play a bigger role in the air gap. Fringing flux is illustrated in Fig. 72. Here one can see that the flux path is longer than expected, which effectively increases the air-gap cross section area, A_g.
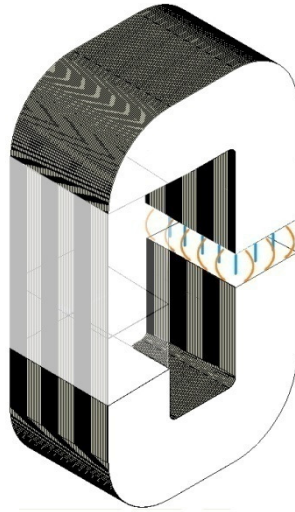
Fig. 72: An inductor core showing leakage flux.

To ensure that the inductance value is accurate, the core material should not saturate magnetically. The maximum flux density for Ferrite cores is much lower than for metal alloys. For example in N27 material, the saturated flux density, B_s = 500 mT @ 25°C and B_s = 440 mT @ 100°C. The flux density in the core can be calculated by

$$
\begin{aligned}
B &= \frac{\Phi}{A} \\
&= \frac{NI}{\Re A} \\
&= \frac{\mu NI}{l} \quad, \\
&= \mu H \\
&= \mu_0 \mu_e H
\end{aligned}
\tag{111}
$$

where H is the magnetic field strength in the core. After step (7) the non-saturation condition should be met by

$$
\begin{aligned}
B_{max} &\geq B_s \qquad \text{(Choose larger core)} \\
B_{max} &< \frac{3}{4} B_s \qquad \text{(Choose smaller core)}
\end{aligned}
\tag{112}
$$

In (112) one can see that if the core does saturate, a bigger core needs to be selected. On the other hand, if the flux density in the core is lower than 75 % of that particular core's saturation flux density, a smaller core can be chosen. Once the final core size is established, the necessary air gap, s, can be calculated in step (8). After the air-gap is calculated another condition has to be met. This condition is necessary so that the fringing flux, which causes inductance inaccuracies, is minimised and is given by

$$s > 2\% \text{ of } l_e \quad \text{(Use less turns)}, \tag{113}$$

where s is the air-gap length. If the air-gap length is greater than the effective length the process has to be redone from step (4), but with less turns. If however the condition is satisfied, the inductor design is complete.

The inductor designed in this thesis has the parameters as seen in Table 10 and the finished product is shown in Fig. 73. It was designed for a RFPM air-cored generator operating at a rated frequency of 80 Hz with a maximum per-phase RMS current of I_{max} = 48 A. L_e is calculated from (66).

Table 10: Parameters of the inductor.

J = 6 A/mm^2	f = 80 Hz	L_e = 1.5 mH	I_{max} = 48 A
d_{coil} = 3.2 mm*	N_{max} = 88	l_e = 230 mm	s = 3.5 mm
B_s = 1.5 T @ 100°C	B_{max} = 1.409 T	k_f = 0.8**	R_{Le} = 0.41 Ω

*This is the diameter of round copper wire that would be equivalent to the cross sectional area of the rectangular wire used to build the prototype.

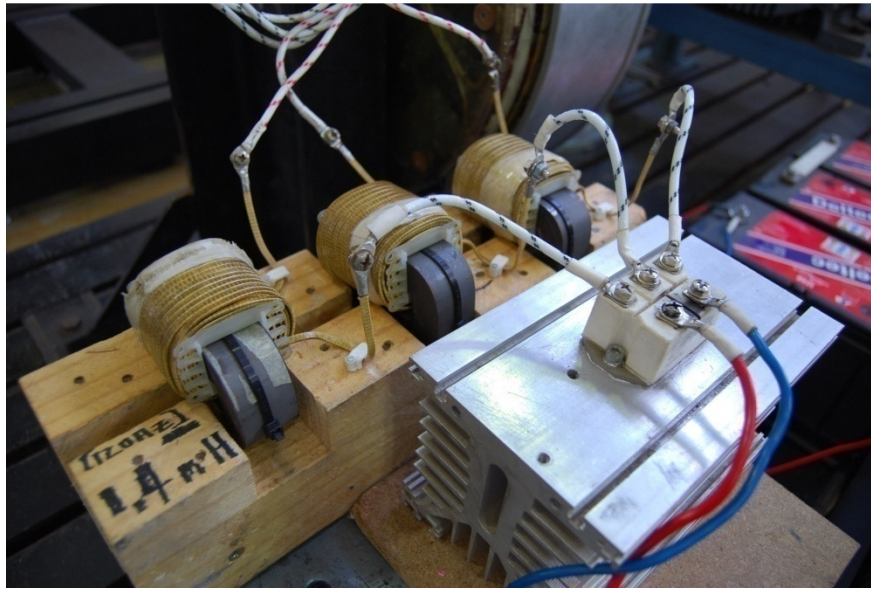**This is the copper filling factor for the rectangular copper wire used.

Fig. 73: 3-Phase inductor connected to the 6-pulse diode rectifier.

Appendix B
Eddy Currents

Eddy losses occur when undesirable eddy-currents are induced in a conducing material due to alternating magnetic field pulsations through it. The induced currents oppose the change in flux that generated them. In this section the nature, measurement and prevention of these losses will be discussed.

B.1 Eddy-losses in an air-cored generator

As previously mentioned, in iron-cored generators eddy-losses are present in the iron stator, stator coils, and the rotor yoke. In air-cored generators however, the stator coils are the only part that is susceptible to major eddy-losses. This is because of the fact that the stator is manufactured from a non-magnetic material and the flux in the rotor yokes remains constant.

When it comes to eddy-losses in conductors, there are three effects that hamper the performance of current carrying conductors that are relevant for discussion. Two of the effects are so small that they become negligible. These two effects are called the skin effect and the proximity effect and are discussed shortly. The third and most prevalent source of eddy losses is also discussed.

Skin effect

The tendency of an alternating current flowing through a conductor is to distribute itself so that the current density near the surface of the conductor is greater than that at its core. This is called the skin effect since the electric current tends to flow near the "skin" of the conductor. This phenomenon also occurs at a certain average depth called the skin depth. The skin effect is disadvantageous because it causes the effective conductor resistance to increase with an increase in current frequency. In essence it causes much of the conductor to carry very little current. The area that does carry current has a much higher current density and the resistance of the wire increases. If the wire resistance is increased more losses will occur, which has a detrimental effect on the generator performance.

Skin effect is caused by the alternating magnetic fields induced by the alternating current the conductor is carrying. The magnetic field coincides with concentric circles around the longitudinal

axis of the conductor. This magnetic field induces eddy-currents in the conductor as shown in Fig. 74 (left).
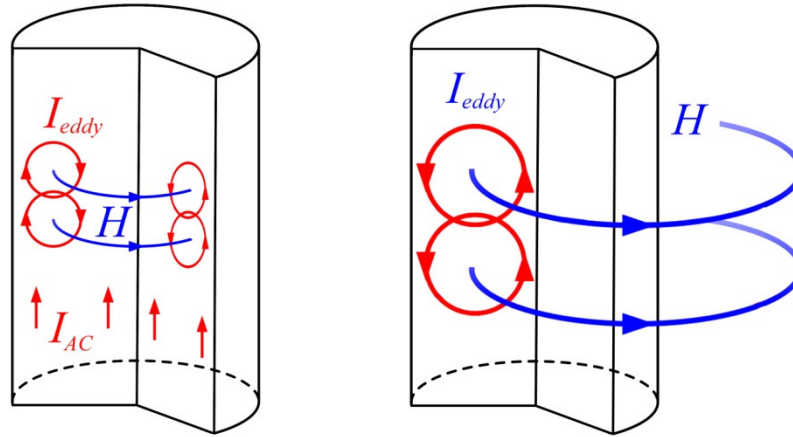

Fig. 74: Skin effect (left) and proximity effect (right).

To calculate whether the conductors of a electric generator or inductor are in danger of being affected by the skin effect, the skin depth can be calculated by evaluating the integral [51]

$$\delta_s = \int_0^\infty e^{-\alpha_c z} dz = \frac{1}{\alpha_c} = \frac{1}{\sqrt{\pi f \mu_{cu} \gamma_{cu}}}, \tag{114}$$

where f is the operating frequency of the ac-current, μ_{cu} is the permeability of copper and γ_{cu} is the conductivity of copper. The skin depth is seen as the depth below the surface of the conductor at which the current density has decayed to $1/\varepsilon$, or roughly 37% of the value of the current density at the surface. If the skin depth is greater than the wire diameter, then the effect becomes negligible. The skin depth of the RFPM air-cored generator prototype built in this study is 5 mm, which is by far larger than the coil diameter of 0.315 mm used. Therefore there exists practically no skin effect in these machines.

Proximity effect

The proximity effect refers to the tendency for eddy-currents to come about due to the presence of magnetic fields generated by conductors in close proximity. The magnetic field created by one conductor cuts through other adjacent conductors and induces eddy currents as shown in Fig. 74 (right). As with the skin effect, the eddy-currents increase the resistance of the conductor, which has a detrimental effect on the generator performance. In general, transformers and inductors are more prone to suffer from proximity effect losses than skin effect losses. There is however also negligible proximity effect present in RFPM air-cored machines.

Eddy losses in RFPM air-cored machines

The third, and by far the most prevalent, source of eddy loss also occurs in the conductors of the RFPM air-cored generator. The permanent magnets located on the rotor yokes generate a radial as well as a tangential magnetic field component in the air gap. The motion of the magnets over the winding produces alternating magnetic fields in the conductors in both the axial and tangential directions, inducing eddy currents [31]. This is shown in Fig. 75. These induced eddy currents may lead to serious additional losses when the generator is operating at relatively high-frequencies. Their presence will increase the temperature of the windings and decrease the efficiency of the machine.
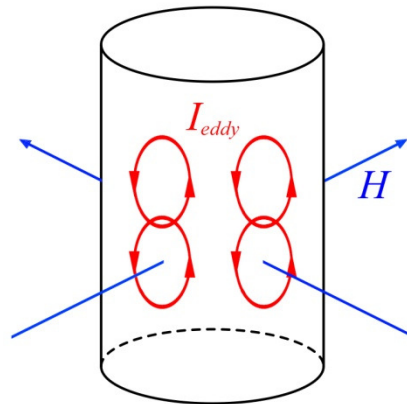
Fig. 75: Induced eddy currents in a single conductor.

B.2 Measuring eddy current losses

To test for the eddy losses at the rated generator speed, two measurements are required. Firstly, the generator phases are disconnected (open circuit configuration). The next step is to spin the rotor at its rated speed of $\omega_r = 320$ r/min. A very small developed torque, T_{d1}, can now be measured on the input side of the generator by means of the torque sensor. The presence of this torque is due to eddy losses, bearing losses and wind and other friction losses on the generator. After this, the stator of the generator is removed so that there is only air between the rotor yokes. The test is repeated without a stator. The second torque reading, T_{d2}, will be smaller than the first because no eddy-losses are present due to the absence of the stator. The difference between these two torque readings multiplied by the speed, gives the eddy loss power, P_{eddy}, in Watt.

The eddy-losses can also be simulated as a resistance, R_{eddy}, situated parallel over the back-EMF of the generator. A representation of R_{eddy} is shown in Fig. 14 and given by

$$R_{eddy} = \frac{3E_{gen}^2}{P_{eddy}}$$

$$= \frac{3E_{gen}^2}{(T_{d1} - T_{d2})\omega_r}$$

(115)

B.3 Minimising the eddy losses

In order to increase generator efficiency it becomes imperative to decrease the machine's eddy-current losses. Litz wire is used to minimise these losses. The word "Litz" is derived from the German word "Litzendraht" meaning woven or stranded wire [50]. This refers to wire consisting of a number of individually insulated copper wires twisted or stranded into a uniform pattern, so that each strand tends to take all possible positions in the cross-section of the entire conductor [50].

Instead of using one large conductor, Litz wire uses a number of small conductors, called strands, positioned parallel to one another to form a bundle. Each strand diameter is less than the skin-depth, which means that an individual strand does not suffer an appreciable skin effect loss. Furthermore, the individual strands are insulated from each other; otherwise all of the wires in the bundle would cause a short circuit, look like a single large wire and still suffer skin effect problems. Lastly, the strands do not occupy the same radial position in the bundle [40]. The bundle is constructed so that the individual strands are positioned periodically on the outside of the bundle and then on the inside of the bundle. This is so that each strand experiences equal measures of the electromagnetic field changes that occur from inner to outer wires.

Further advantages of using Litz wire in construction include: Good temperature resistance (insulation can withstand temperatures of up to 240°C), decreases in labour costs (wires are stranded by machine rather than by hand) and better filling factors (filling factors range from $k_f = 0.6 - 0.8$). Three types of Litz wire are illustrated in Fig. 76.
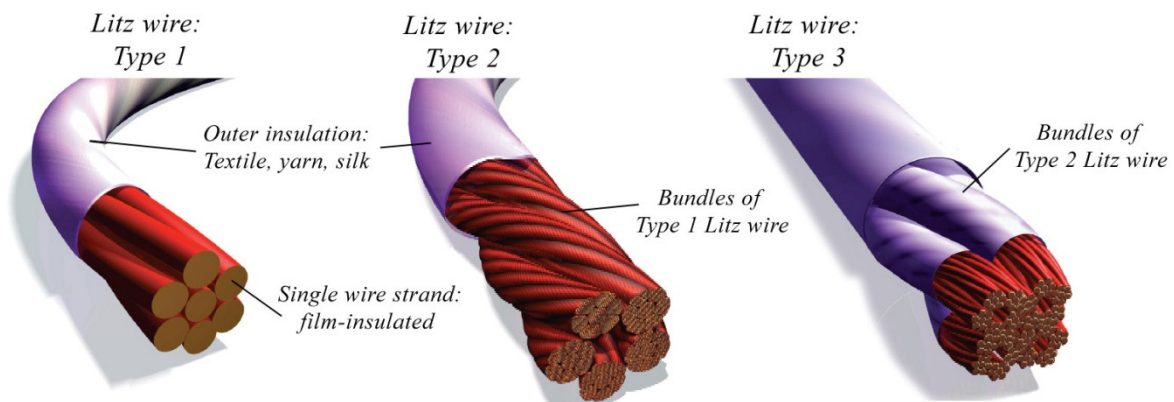
Fig. 76: Litz wire: Type 1,2 and 3.

Appendix C
Fastener design

C.1 Bolted connections

Typical stresses acting on non-permanent screwed or bolted joints include both shear and tensile stresses as shown in Fig. 77 [20]. Once the bolt or bolt-nut connection is tightened, the link is loaded in tension and the clamped parts in compression. If opposite forces act on the different clamped parts of the assembly, as shown in Fig. 77, shear stresses arise in the bolted connection. Another form of shear stress acts on the threads of the bolt throughout their engagement length. It is these shear stresses which cause the stripping of a bolt or screw or the internal thread in the connection or nut. Lastly, bearing stress is characterized by the crushing of the bolt or plate.

Failure in bolted connections can occur in one of the following ways: (a) External or internal threads can strip (shear), (b) the bolt can break due to excessive tensile stresses placed on it, (c) the shear stresses caused by members can cause failure, or (d) bearing stresses in the member or bolt can induce a break in either.

Fig. 77: Non-permanent bolted fastener connection.

Proof strength, a rough equivalent to yield strength, is the maximum tensile stress to which an external fastener can be subjected without permanent deformation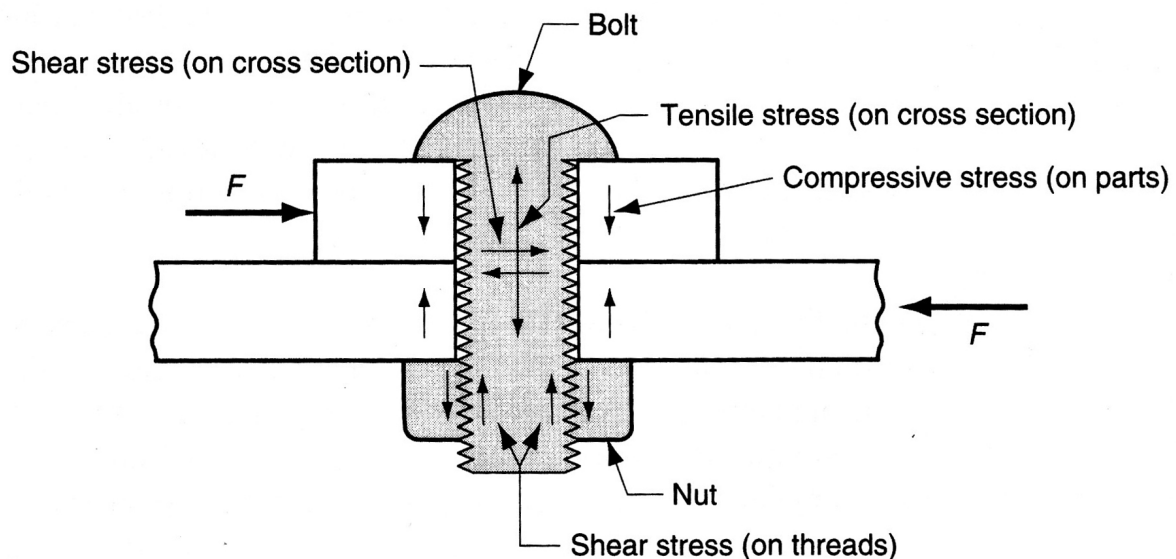 of the material. A fastener's ultimate tensile strength on the other hand is the maximum stress it can withstand in the tensile direction before breaking [23].

The following method is developed to determine the minimum bolt thicknesses needed for each of the non-permanent bolted connections of the machine.

Design of the bolts in fixing the blades onto the aluminium front plate

In this section the calculations done in the design of the bolts responsible for mounting the turbine blades to the front rotor plate, will be discussed. The bolts are subject to 3 forces. These forces consist of a torque moment force, a centrifugal force and gravity. The last two are largely dependent on the mass of the turbine blades. The torque moment is calculated with,

$$F_{T1} = \frac{M_{T1}}{r_{T1}} \, , \tag{116}$$

where F_{T1} is the force generated by the torque moment on the machine at rated speed, M_{T1} is the moment induced by the torque and r_{T1} is the perpendicular distance from the centre of the bolt to the axis of rotation passing through the shaft. Next, the centrifugal force is calculated by [52] as

$$F_{cen} = m_{blade} a_n \, , \tag{117}$$

where F_{cen} is the centrifugal force due to the rotating blade mass, m_{blade}, and the normal acceleration of the load carrying bolt, a_n. The normal acceleration of the bolt is calculated as [52]

$$a_n = \frac{v_t^2}{\rho_B} = \frac{(r_B \omega_m)^2}{\rho_B} = r_B \omega_m^{\,2} \quad (\text{with } \rho_B = r_B) \, , \tag{118}$$

where ω_m is the angular velocity of the bolt and r_B is the perpendicular distance from the axis of rotation to the centre of gravity of the blade. Each turbine blade possesses a mass of 10 kg which creates another force, rendered by gravity, on the two bolts. The gravitational force, F_g, generated on each of the two bolts can be calculated as [52]

$$F_g = \frac{1}{2} m_{blade} a = \frac{1}{2} m_{blade} g \, , \tag{119}$$

where g is the gravitational acceleration. Since there are two bolts used on every turbine blade, the centrifugal force exerted on each can be calculated with trigonometry as

$$F_{c1,2} = \frac{F_{cen}}{\sqrt{2(1 - \cos(\pi - \theta_b))}} \, , \tag{120}$$

where θ_b is the angle between the bolts measured from the centre of gravity. This angle is shown in Fig. 78.
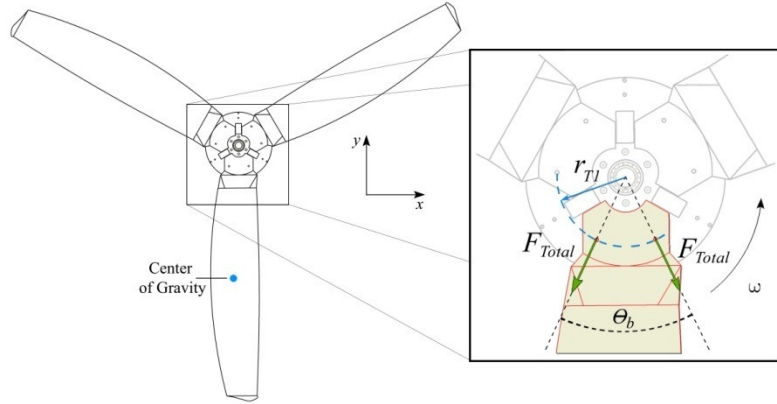

Fig. 78: Wind turbine blades with forces shown.

The combination of the three forces calculated above will cause two resulting forces of equal size to act on each of the two bolts. When the blade is at the bottom of the turbine, the three forces all act in a common direction, downwards. The bolts will thus experience the greatest load when the blades are in this position. When forces are acting in the same direction, they can be summed together. The magnitude of the total resulting force, illustrated in the figure, is calculated with trigonometry by adding the x and y directional components of the forces as

$$F_{total} = \sqrt{\left(F_{c1,y} + F_{T1,y} + F_{g,y}\right)^2 + \left(F_{c1,x} + F_{T1,x}\right)^2} \ . \tag{121}$$

Note that the gravitational force, F_g, does not have a component in the horizontal direction x, and is thus omitted. Once the resulting force on each of these bolts is known, the corresponding bolt thickness needed to withstand this load can be determined analytically. Three strength considerations are of importance here. They are the bearing stress in the bolt (σ_b), the bearing stress in the member (σ_m) and the shear of the bolt (τ_b). To determine an adequate bolt diameter that will withstand the bearing stress on the bolt, the following calculation is used by [23] as

$$d_b = \frac{F_{total} \, n_d}{2t \, S_p} , \tag{122}$$

where d_b is the required minimum bolt thickness able to withstand a force, F_{total}, with a design safety factor, n_d. The thickness of the thinnest member in the bolted connection is represented by t and the proof strength of the bolt material by S_p. Next, an adequate bolt diameter that would allow the members to withstand the bearing stress in the members is calculated by [23] as

$$d_b = \frac{F_{total} n_d}{2t(S_y)_{member}} , \tag{123}$$

where $(S_y)_{member}$ is the yield strength of the weakest bolted member. In this case the yield strength of aluminium is chosen as this is the weaker metal of this particular bolted connection. Lastly, an adequate bolt diameter needs to withstand the shear on the bolt. This diameter is calculated by [23] as

$$d_b = \sqrt{\frac{4\,F_{total}\,n_d}{0.577\,n_b\,\pi\,S_p}}\,,\tag{124}$$

where n_b is the number of active bolts sharing the shear. To determine a bolt size that will handle the load, F_{total}, the largest diameter of (122), (123) and (124) should be chosen.

Design of the bolts in fixing two steel rotor disks to the aluminium front plate.

To fix the two rotor disks to the front aluminium plate, a bolted connection is used. This connection is made in the axial direction through the front plate into the wall of the rotor yoke. A small part of the base of this yoke was machined to accommodate the threaded bolt holes. The same calculations are repeated on these bolts and members as in the previous section.

Appendix D
Deflection of a cantilever beam

In this section the deflection of a cantilever beam with one or more concentrated loads are discussed. In (78) of section 3.1.1 the deflection of a beam with 3 concentrated loads is calculated. This equation will be derived in this section.
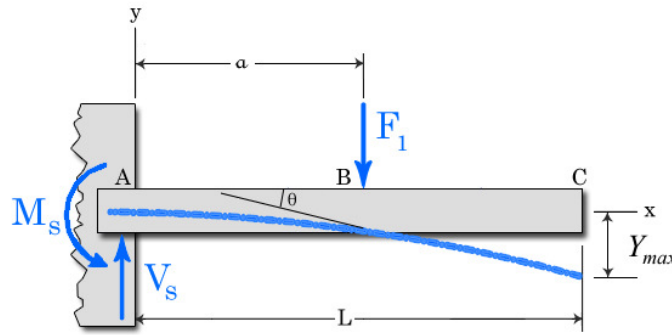
Fig. 79: Cantilever beam deflection.

The bending moment, M, present on the shaft is a function of x and is given by

$$M = -M_s + xV_s, \tag{125}$$

where M_s is the bending moment at the fixed end of the beam (shown in Fig. 79) and given by

$$M_s = a\,F_1, \tag{126}$$

with F_1 is a concentrated force acting downwards at a distance a from the fixed end. The shear force, V_s, can be calculated as,

$$V_s = F_1 \ . \tag{127}$$

The deflection anywhere on the shaft can be determined by using the double integration method of [42] as

$$EI_0 \frac{d^2\Upsilon}{dx^2} = -M = a\,F_1 - x\,F_1. \tag{128}$$

Rearranging and integrating this gives,

$$\Upsilon_x = \int\left(\int \frac{d^2\Upsilon}{dx^2}dx\right)dx = \int\left(\int -\frac{M}{EI_0}dx\right)dx + C_1 x + C_2, \tag{129}$$

where Υ_x is the deflection at distance x on the shaft, E is the Young's modulus of the shaft material, I_0 is the area moment of inertia of the hollow shaft and C_1 and C_2 are integration constants which can be evaluated from the known conditions of slope and deflection at certain points, usually at the supports. Solving equation (129) gives,

$$\Upsilon_x = \frac{a F_1 x^2}{2 E I_0} - \frac{F_1 x^3}{6 E I_0} + C_1 x + C_2, \tag{130}$$

The integration constant, C_1, is solved by looking at the slope boundary condition at the fixed end. The slope at the fixed end (at $x = 0$ m) of the cantilever beam is zero. Substituting $x = 0$ m into the slope equation gives

$$\frac{d\Upsilon}{dx} = 0 = \frac{a F_1 x}{E I_0} - \frac{F_1 x^2}{2 E I_0} + C_1. \tag{131}$$

This causes C_1 to be zero. Next, the integration constant, C_2, is solved by looking at the deflection boundary condition at the fixed end. The deflection at the fixed end (at $x = 0$ m) of the cantilever beam is also zero. Substituting $x = 0$ m into the deflection equation of (130) equation gives

$$\Upsilon_x = 0 = \frac{a F_1 x^2}{2 E I_0} - \frac{F_1 x^3}{6 E I_0} + C_2. \tag{132}$$

From (132) C_2 is also zero. Since both integration constants are zero, (130) becomes simpler and is now expressed as

$$\Upsilon_x = \frac{F_1}{2 E I_0}\left(a x^2 - \frac{x^3}{3} \right). \tag{133}$$

To calculate the deflection at distance a (represented by B in Fig. 79) on the beam simply substitute $x = a$. From this, (133) becomes

$$\Upsilon_B = \frac{a^3 F_1}{3 E I_0}. \tag{134}$$

It should be noted that (134) can only be used from the fixed end up until the concentrated load (point B) in Fig. 79. Beyond point B there exists no force on the beam. It simply remains straight just as before the load was applied. Thus, from point B to the free end at point C the slope remains the same but the deflection will still increase. To calculate the deflection at C the following calculation is done by [42]

$$\Upsilon_C = \Upsilon_B + \left[(\text{slope at B}) \times (L - a) \right]. \tag{135}$$

Therefore, (135) can be written as

$$\Upsilon_C = \frac{a^3 F_1}{3 EI_0} + \frac{a^2 F_1}{2 EI_0}(L - a)$$

$$= \frac{a^2 F_1}{2 EI_0}\left(L - \frac{a}{3}\right) \qquad (136)$$

$$= \frac{a^2 F_1}{6 EI_0}(3L - a)$$

This corresponds to (78) of section 3.1.1.

Appendix E
Derivation of important formulae

In this section various important formulae are derived and/or discussed. These derivations are not given in the main text due to space constraints. Among the formulae given are the flux linkage, stator winding factor and the stator end winding factor.

Flux-linkage, λ

The flux-linkage for the concentrated winding topology, as seen in Fig. 12, at position δ inside the coil is calculated by [25] as

$$\lambda_c = \int_0^l \int_{\alpha+\delta}^{\alpha+\frac{2\pi}{p}-\Delta-\delta} B_{p1} \sin\left(\frac{\theta p}{2}\right) r_n \, d\theta \, dz , \tag{137}$$

with the maximum flux linkage at

$$\alpha = \frac{1}{2}\left[\frac{2\pi}{p} - \left(\frac{2\pi}{Q} - \Delta\right)\right], \tag{138}$$

where Δ is the coil side width. The flux-linkage for an overlapping winding topology at position δ inside the coil is calculated by [25] as

$$\lambda_o = \int_0^l \int_{\alpha+\delta}^{\alpha+\frac{2\pi}{p}-\delta} B_{p1} \sin\left(\frac{\theta p}{2}\right) r_n \, d\theta \, dz . \tag{139}$$

This makes the total flux-linkage for a typical overlapping coil with N_t conductor turns equal to

$$\lambda_N = \frac{4}{p} N_t B_{p1} \cos\left(\alpha \frac{p}{2}\right) r \, l_a k_\lambda . \tag{140}$$

Stator winding factor, k_w

The winding factor of a concentrated winding topology, as shown in Fig. 11, is calculated as

$$k_w = k_p k_d , \tag{141}$$

where k_p is the pitch factor given by [29] as

$$k_p = \frac{\sin\left[\theta_c\left(1-\kappa\right)/2\right]\sin\left(\kappa\theta_c/2\right)}{\kappa\theta_c/2} \tag{142}$$

and k_d is the distribution factor given by [44] as

$$k_d = \frac{\sin\left[u\left(\theta_c-\pi\right)/2\right]}{u\sin\left[\left(\theta_c-\pi\right)/2\right]}, \tag{143}$$

where u is the number of coils in a phase group. If there is only one coil in a phase group, k_d becomes unity. θ_c is defined in Fig. 11 as

$$\theta_c = \frac{\pi p}{Q}. \tag{144}$$

Stator end-winding factor, k_e

The stator end-winding factor is used in the ratio of the total end winding length, l_e, to the axial active winding, l_a, as

$$\delta_c = \frac{l_e}{l_a} = 2k_e\left(\frac{d}{l_a}\right). \tag{145}$$

For practical non-overlapping windings, l_e is given by [29] as

$$l_e = \frac{2d\theta_c}{p}\left(1-0.59\kappa\right). \tag{146}$$

After substituting (146) and (144) into (145) and rearranging, k_e is expressed by

$$k_e = \frac{\pi}{Q}\left(1-0.59\kappa\right). \tag{147}$$

with κ given in (18).

Bibliography

[1]   J.F. Manwell, J.G. McGowan and A.L. Rogers, *Wind energy explained – Theory, design and application*. John Wiley & Sons Ltd, 2003.

[2]   F.M. White, *Fluid mechanics – Fifth edition*. McGraw-Hill, 2003.

[3]   DNV Risø, *Guidelines for design of wind turbines – Second edition*. Det Norske Veritas, Copenhagen and Wind Energy Department, 2002.

[4]   T. Burton, D. Sharpe, N. Jenkins and E. Bossanyi, *Wind energy handbook*. John Wiley & Sons Ltd, 2008.

[5]   Renewable Energy World Magazine, Jul 2010 Issue, pp 33.

[6]   K. Hagemann, "Mesoscale wind altas of South Africa," PhD dissertation, University of Cape Town, 2008.

[7]   T. Hayashi, Y. Li, Y. Hara and K. Suzuki, "Wind Tunnel Tests on a Three-stage Out-phase Savonius Rotor," Tottori University, Japan, 2004.

[8]   J. Krenciszek, S.O. Akindeinde, H. Braun, C. Marcel, E. Okyere and I. Argatov, "Mathematical Modelling of the Pumping Kite Wind Generator: Optimization of the Power Output," Tampere University of Technology, Finland, 2008.

[9]   M.A. Khan, P. Pillay and K.D. Visser, "On Adapting a Small PM Wind Generator for a Multiblade, High Solidity Wind Turbine," *IEEE Transactions on energy conversion*, vol. 20, no. 3, pp. 685-692, 2005.

[10]   H. Polinder, F.F.A. van der Pijl, G.-J. de Vilder and P. Tavner, "Comparison of Direct-Drive and Geared Generator Concepts for Wind Turbines," *IEEE Transactions on Energy Conversion*, vol. 21, no.3, pp. 725-733, 2006.

[11]   M.A. Mueller and A. S. McDonald, "A lightweight low speed permanent magnet electrical generator for direct-drive wind turbines," in *European wind energy conference (EWEC) Brussels,* 2008.

[12]   R. Harrison, E. Hau and H Snel, Large wind turbines – Design and economics. John Wiley & Sons, 2000.

[13] J.A. Stegmann, M.J. Kamper, "Design Aspects of Double Rotor Radial Flux Air-cored Permanent Magnet Wind Generator", *IEEE Energy Conversion and Conference and Expo (ECCE)*, San Jose, USA, pp. 3634 – 3640, Sept. 2009.

[14] A.M. de Broe, S. Drouilhet and V. Gevorgain, "A Peak Power Tracker for Small Wind Turbines in Battery Charging Applications", *IEEE Transactions on Energy Conversion*, vol. 14, no. 4, pp. 1630-1635, 1999.

[15] S. Drouilhet, E. Muljadi, R. Holz and V. Gevorgian, "Optimizing Small Wind Turbine Performance in Battery Charging Applications", *25th Annual Conference and Exhibition on Wind Power*, Washington, DC, 27-30 Mar. 1995.

[16] E. Muljadi, S Drouilhet, R. Holz and V. Gevorgain "Analysis of Wind Power for Battery Charging", *Proceedings of the 15th American Mechanical Engineering Wind Energy Symposium,* Houston, TX, 1996.

[17] P. Sivachandran and P. Venkatesh, "Design and analysis of dual-rotor radial flux permanent magnet generator for direct coupled stand-alone wind energy systems," *International Journal of Innovations in Energy Systems and Power (IJESP)*, vol. 2, no. 1, pp. 24-29, 2007.

[18] G. Tomassi, M. Topor, F. Marignetti, and I. Boldea, "Characterization of an axial-flux machine with non-overlapping windings as a generator," *Electromotion*, vol. 13, no. 1, pp. 73-79, 2006.

[19] B.J. Chalmers, W. Wu and E. Spooner, "An axial-flux permanent-magnet generator for a gearless wind energy system," *IEEE Transactions on Energy Conversion*, vol. 14, no. 2, pp. 251-257, 1999.

[20] M.P. Groover, *Fundamentals of modern manufacturing – Second edition*. John Wiley & Sons, 2004.

[21] J.S. Rohatgi and V. Nelson, *Wind characteristics: An analysis for the generation of wind power*. Alternative energy institute, Canyon, TX, 1994.

[22] Encyclopædia Britannica Online - http://www.britannica.com/EBchecked/topic/78706/breeze. Viewed on 27 Oct. 2009.

[23] J.E. Shigley, C.R. Mischke and R.G. Budynas, *Mechanical engineering design – Seventh edition*. McGraw-Hill, New York, 2004.

[24] F.G. Rossouw, "Analysis and design of axial flux permanent magnet wind generator system for direct battery charging applications," MSc.Eng dissertation, University of Stellenbosch, 2008.

[25] P.J. Randewijk, M.J. Kamper and R-J. Wang, "Analysis and performance evaluation of radial flux air-cored permanent magnet machines with concentrated coils," *7th Int. Conference on Power Electronics and Drive Systems (PEDS),* Bangkok (Thailand), pp. 189-195, Nov. 2007.

[26] R.-J. Wang, M.J. Kamper, K. Van der Westhuizen, and J. Gieras, "Optimal design of a coreless stator axial flux permanent-magnet generator," *IEEE Transactions* on *Magnetics*, vol. 41, no 1, pp. 55-64, 2005.

[27] M.J. Kamper, F.G. Rossouw and R-J. Wang, "Analysis and performance evaluation of axial flux air-cored stator permanent magnet machine with concentrated coils," in *IEEE International Electric Machines and Drives Conference (IEMDC)*, Turkey, pp. 13-20, May 2007.

[28] M.J. Kamper, R-J Wang, F.R. Rossouw, "Analysis and Performance of Axial Flux Permanent-Magnet Machine with Air-Cored Non-overlapping Concentrated Stator Windings", *IEEE Transactions on Industry Applications,* vol. 44, no. 5, pp. 1495-1504, Sep/Oct 2008.

[29] M.J. Kamper, "Comparison of linear permanent magnet machine with overlapping and non-overlapping air-cored stator windings", *The 4th Int. Conference on Power Electronics, Machines and Drives* (PEMD), York (UK), pp.767-771, April 2008.

[30] J.A. Stegmann and M.J. Kamper, "Design Aspects of Double-Sided Rotor Radial Flux Air-cored Permanent Magnet Wind Generator," *IAS Journal Paper*, currently under review.

[31] R-J. Wang and M.J. Kamper, "Calculation of eddy-current loss in axial field permanent magnet with coreless stator," *IEEE Transactions on Energy Conversion*, vol. 19, no. 3, pp. 532-538, 2004.

[32] F.G. Rossouw and M.J. Kamper, "Use of air-cored axial flux permanent magnet generator in direct battery charging wind energy systems," *Power Electronics and Drive Systems (PEDS)*, Bangkok, 2007.

[33] T. Wildi, *Electrical machines drives, and power systems – Fifth edition*. Pearson Education, New Jersy, 2002.

[34] N.A. Karim, J. Azzouzi, and G. Barakat, "Influence of skewing on the performances of an axial flux PM wind generator coupled to a diode rectifer," *IEEE International Electric Machines & Drives Conference* (IEMDC), vol. 2, pp. 1037-1042, 2007.

[35] J.E. Gieras, R-J. Wang and M.J. Kamper, *Axial flux permanent magnet brushless machines*. Kluwer, 2004.

[36] J. F. Gieras, R.-J. Wang and M. J. Kamper, *Axial flux permanent magnet brushless machines – 2nd Edition*. Springer science, 2008.

[37] Z. Q. Zhu, Y. Chen, D. Howe and J.H. Gliemann "Rotor eddy current loss in single-phase permanent magnet brushless dc motor" *in Proceedings of IEEE IAS Annual Meeting*, New Orleans, LA, USA, pp. 537 – 543, Sept. 2007.

[38] F.M. Rodrigo, L.C. Herrero de Lucas, S. de Pablo Gómez and J.M. González de la Fuente, "Analysis of the efficiency improvement in small wind turbines when speed is controlled", *IEEE International Symposium on Industrial Electronics (ISIE)*, pp. 437-442, 2007.

[39] A. Koyanagi, H. Nakamura, M. Kobayashi, Y. Suzuki and R. Shimada, "Study on maximum power point tracking of wind generators using a flywheel", *IEEE Power Conversion Conference (PCC)*, Osaka, Japan, pp. 322-327, 2002.

[40]   R-J. Wang, "Design aspects and optimisation of an axial field permanent magnet machine with ironless stator," Ph.D. dissertation, Department of Electrical Engineering, University of Stellenbosch, Matieland, South Africa, 2003.

[41]   R.R. Craig Jr., *Mechanics of materials – Second edition*. John Wiley & Sons Ltd, 2000.

[42]   P.P. Benham, R.J. Crawford and C.G. Armstrong, *Mechanics of engineering materials – Second edition.* Pearson Education Ltd, 1996.

[43]   H. Kierstead, R.-J. Wang and M.J. Kamper, "Design optimization of a single-sided axial flux permanent magnet in-wheel motor with double-layer non-overlap concentrated winding", *Southern African Universities Power Engineering Conference (SAUPEC)*, Stellenbosch, pp. 36-40, 2009.

[44]   M.J. Kamper, A.J. Rix, D.A. Wills and R-J Wang, "Formulation, finite element modelling and winding factors of non-overlap winding permanent magnet machines", *Proceedings of International Conference on Electrical Machines (ICEM)*, Vilamoura (Portugal), Sept. 2008.

[45]   J.R. Bumby, N Stannard, J. Dominy and N. McLeod, "A Permanent Magnet Generator for Small Scale Wind and Water Turbines", *18th International Conference on Electrical Machines (ICEM)*, Sydney, Australia, 2008.

[46]   J.R. Bumby, N Stannard and R. Martin, "A Permanent Magnet Generator for Small Scale Wind Turbines", *International Conference on Electrical Machines (ICEM)*, Greece, 2006.

[47]   N. Mohan, T.M. Undeland and W.P. Robbins, *Power Electronics – Converters, Applications, and design.* John Wiley & Sons Ltd, 2003.

[48]   Colonel W.T. McLyman*, Transformer and inductor design handbook.* Pearson, 2003.

[49]   J.R. Bumby and R. Martin, "Axial-flux permanent-magnet air-cored generator for small-scale wind turbines," *Proc. IEE - Electrical Power Applications*, vol. 152, no. 5, pp. 1065-1075, 2005.

[50]   http://www.litz-wire.com/applications.html, viewed on 2 June 2010.

[51]   D. Rodger, P.J. Leonard, H.C. Lai and P.C. Coles, "Finite element modelling of thin skin depth problems using magnetic vector potential", *IEEE Transactions on magnetics*, vol. 33, no. 2, pp. 1299 - 1301, 1997.

[52]   J.L. Meriam and L.G. Kraige, *Engineering Mechanics: Dynamics – Fifth Edition*. John Wiley & Sons Ltd, 2003.